GRAVITATIONAL MICROLENSING AND DYNAMICS IN THE MILKY WAY

A thesis submitted to the University of Manchester
for the degree of Doctor of Philosophy
in the Faculty of Engineering and Physical Sciences

2006

By
Alexander Anthony Wood
School of Physics and Astronomy

(EPKDE)

Contents

List of Tables

List of Figures

Abstract

This thesis is concerned with gravitational microlensing; specifically, microlensing towards the central bulge of the Milky Way. Calculations are presented for a new Galactic model, which is empirically normalised by *Hubble Space Telescope* (*HST*) star counts. Maps and distributions of the expected microlensing optical depth, τ, and average event timescale are generated. Good agreement is found with data recently published by the OGLE, MACHO and EROS collaborations. Various event rate distributions are also predicted. The fractional contributions to the total expected event rate, as a function of timescale, are found for different types of lenses. Asymptotic behaviour is clearly seen at both long and short timescales: the fractional contribution from a lens of mass M is found to be weighted by $M^2\,n(M)\,\mathrm{d}M$ and $M^{-1}\,n(M)\,\mathrm{d}M$, respectively. This is independent of the density and kinematics of the lens population, and hence provides valuable information concerning the lens mass function. These weightings are also derived directly from the event rate equation, and similar asymptotic behaviour is seen as a function of Einstein radius. It is estimated that a few per cent of stellar lenses should be detected with event follow-up observations by the *HST* and the *James Webb Space Telescope* after 10–20 yrs.

Reported measurements of the optical depth based on the lensing of red clump giants (RCGs) are significantly below those using lensing of all stars. It is found that this discrepancy cannot be explained by a dependence of the lensing surveys on their different flux limits. τ is predicted as a function of source apparent magnitude: the trend is generally flat, but with a significant oscillation caused by RCG sources. A comparison with the latest observations from EROS is inconclusive, finding an apparent oscillation in the data, but at a low significance, as the data are still insufficient. The predicted amplitude of the τ oscillation varies with the inclination angle of the Galactic bar, as does the expected total τ. Combining this latter dependance with the latest measurements, upper limits are placed on

the bar angle, ruling out large values supported by recent observations.

The stellar proper motions and velocity dispersions in the Galactic bulge are examined. A relatively simple kinematic model is built upon, in order to reproduce newly discovered trends of proper motion and dispersion with latitude, longitude and distance. The effect of each modification to the model is analysed, and in only a few steps, a good overall fit to the observations is obtained. This demonstrates what can be achieved with kinematic models that are simpler and less computationally expensive than those constructed with other, more sophisticated techniques.

Finally, the first direct detection of a microlens towards the bulge is presented, for which data analysis is ongoing at the time of writing. A preliminary maximum likelihood analysis is performed. This shows that when all the available observable parameters are securely determined, precise estimates of the lens mass and distance will be possible. This would be only the second precise mass measurement of an isolated star, other than the Sun, to date.

Declaration

Except where stated, the work contained in this thesis is that of author alone.
No portion of the work referred to in this thesis has been submitted in support of an application for another degree or qualification of this or any other university or other institution of learning.

Copyright

The Author

The author graduated from the University of Manchester in 2002 with a M.Phys. (Hons) degree in Physics with Astrophysics. In September that year he began studying for a Ph.D. at Jodrell Bank Observatory, University of Manchester. The results of that work are presented in this thesis.

Refereed publications and conference contributions

Refereed journals

- *Optical depths and time-scale distributions in Galactic microlensing*
  Wood A., Mao S., 2005, MNRAS, 362, 945
- *Optical depth as a function of source magnitude*
  Wood A., 2006, MNRAS, in prep.
- *The first direct detection of a gravitational μ-lens toward the Galactic bulge*
  Kozłowski S., Woźniak P.R., Mao S., Wood A., 2006, ApJ, in prep.

Conference contributions

- *Simulations of gravitational microlensing by extra-solar planets*
  Talk at XXXIII Young European Radio Astronomers Conference (YERAC), 2003, Bonn
- *Gravitational microlensing and the structure of the Galaxy*
  Talk at XXXIV YERAC, 2004, Cork
- *Optical depth maps, timescale distributions and lens detection with Galactic microlensing*
  Talk at ANGLES network Workshop, 2005, Crete

Acknowledgements

I give my thanks to the following: my supervisor Shude Mao, for his instruction, guidance and support; Martin Smith and Nick Rattenbury, for their general help and advice; Szymon Kozłowski, with whom I collaborated on part of this work; and Jim Rich of the EROS collaboration, for providing me with some of their unpublished data.

I am grateful to Andrew Lyne for making available the facilities at Jodrell Bank; to Belinda, Janet, Pat, Sarah, Stella et al. for their general assistance; to Ant, Bev, Bob et al. for being there when the computer gremlins came out to play (and for often kindly bumping up my disk quota); and to PPARC, for the award of a studentship, and for the provision of a students' travel budget that enabled me to travel the world in the name of conferences, which I much enjoyed attending.

I thank all the other great people who I either met at Jodrell or got to know better in my time here, for making it such a great place for me to spend four years, with the good fun and bad jokes (cheers Paul). In no particular order: the Theory Group (Dave A., Neal, Nick, Paddy, Richards B., J., and L., Shude, Tim et al.), for the weekly discussions about interesting papers and other matters theoretical; the Lensing Group (Dave A., Edward, Ian, Lukasz, Ming, Neal, Nick, Richard L., Sanhita, Shude, Szymon, Tom et al.), for the weekly discussions about matters lensing and otherwise, held over pub lunches (with special mention to those generous members who always supplied the students with free drinks); the Jodrell Bank Football Club (Ant, Chin, Chris, Clive, Dave, David, Garth, Iain, Matts G. and S., Richard B., Tim, Zamri et al.), for the brilliant five/six-a-side matches (with special mention to the mysterious powers of The Algo, that usually produced close games); and also in particular Alan, Cesar, Cormac, Danielle, Debbie, Francisco, Helen, Jenny, Jimi, Lisa, Magda, Megan, Simon, Tony, and Stuart who kindly gave this thesis a thorough proofreading. Apologies to anyone

else I should have included.

Finally I thank my family, especially my parents Valerie and Tony, for all their love, support and encouragement, without which none of this would have been possible.

Notations, abbreviations and miscellaneous notes

The conventional abbreviations for SI units and astronomical quantities are used. The following abbreviations are used in this thesis:

- ACS – Advanced Camera for Surveys
- BD – Brown Dwarf
- BH – Black Hole
- BW – Baade's Window
- CGR – Central Galactic Region
- CMD – Colour-Magnitude Diagram
- *COBE* – *Cosmic Background Explorer* satellite
- DIA – Difference Image Analysis
- dof – Degrees Of Freedom
- EROS – Expérience pour la Recherche d'Objets Sombres (EROS collaboration)
- GLIMPSE – Galactic Legacy Infrared Mid-Plane Survey Extraordinaire
- HG03 – Han & Gould (2003)
- *HST* – *Hubble Space Telescope*
- *JWST* – *James Webb Space Telescope*
- K06 – Kozłowski et al. (2006)
- KS – Kolmogorov–Smirnov (KS test)
- LF – Luminosity Function
- LMC – Large Magellanic Cloud
- LOS – Line Of Sight
- MACHO – Massive Astrophysical Compact Halo Objects / MACHO collaboration
- MOA – Microlensing Observations in Astrophysics (MOA collaboration)
- MS – Main-Sequence / Main-Sequence star
- NGP – North Galactic Pole
- NS – Neutron Star

- OGLE – Optical Gravitational Lensing Experiment (OGLE collaboration)
- PSF – Point Spread Function
- RCG – Red Clump Giant
- *RF* – Reddening-Free magnitude
- rms – Root-Mean-Square
- SMC – Small Magellanic Cloud
- S/N – Signal-to-Noise ratio
- *SST* – *Spitzer Space Telescope*
- TVT – Tensor Virial Theorem
- WFPC2 – Wide Field Planetary Camera 2
- WD – White Dwarf

The following are some of the most commonly used symbols in this thesis:

- $D_{\rm d}$ – The deflector (lens) distance
- $D_{\rm s}$ – The source distance
- $M_{\rm d}$ – The lens mass
- $r_{\rm E}$ – The Einstein radius projected onto the lens plane
- τ – The microlensing optical depth
- $t_{\rm E}$ – The Einstein radius crossing time
- $\theta_{\rm bar}$ – The inclination angle of the Galactic bar
- $\theta_{\rm E}$ – The angular Einstein radius

In general, this thesis follows the conventions of the journal *Monthly Notices of the Royal Astronomical Society.* For example, in the lists of references, all authors of a paper are given only when there are eight or fewer.

There are a few minor differences in this thesis to the corresponding published work, due to corrections that have no significant effect on the results.

"Have you noticed that the astronomers and mathematicians are much the most cheerful people of the lot? I suppose that perpetually contemplating things on so vast a scale makes them feel either that it doesn't matter a hoot anyway, or that anything so large and elaborate must have some sense in it somewhere."

– Dorothy L. Sayers
The Documents in the Case

Chapter 1

Introduction and literature review

1.1 Introduction

Gravitational lensing, first discussed centuries ago, was long considered a mere theoretical curiosity. The last two decades have seen its rapid growth into a major astrophysical tool. A brief history of gravitational lensing is given in §1.2. This chapter then focuses on one aspect of the field: microlensing, which itself has numerous interesting and important applications, and is the concern of this thesis. The basic theory is presented in §1.3. A review of the literature, current endeavours and future prospects follows in §1.4 – §1.6, with greater emphasis on those areas relevant to the work in this thesis. That work is outlined in §1.7.

1.2 Brief history

Newton first proposed that light is bent by gravitational fields in his 1704 *Opticks*, but no calculation was published until Soldner (1804) claimed that light should be deflected at the solar limb by 0.875 arcsec. Einstein (1911) independently reproduced Soldner's formula, then in 1915, using his general theory of relativity, found the correct value to be twice his previous result. This was soon confirmed when Dyson, Eddington & Davidson (1920) famously measured the apparent

angular shift of stars close to the Sun during the solar eclipse of 1919[1]. *Gravitational lensing* refers to this deflection of light by massive bodies and the resulting phenomena.

Eddington (1920) realised there may be multiple light paths from a source to observer, giving multiple images of a single source. Chwolson (1924) went further, showing that lensing of stars by other stars could create images of fictitious double stars, and that if two stars were exactly aligned, the background source would appear as a ring-shaped image centred on the foreground lens – these are now called Einstein rings.

Einstein (1936, see also Renn, Sauer & Stachel 1997) also considered star-star lensing and concluded the lensed images would be unresolvable with the telescopes then available. However, Zwicky (1937a) showed that resolvable images *would* be produced by galaxy-galaxy lensing. He correctly predicted that as well as providing an additional test of general relativity, this effect would magnify distant, otherwise undetectable galaxies, and enable accurate determinations of galaxy masses. He also correctly estimated the probability of galaxy lensing to be $\sim$1% (1937b).

Gravitational lensing was then not reconsidered in the literature until papers by Klimov (1963), Liebes (1964) and Zel'dovich (1964), and by Refsdal (1964) who derived most of the essential lensing formulae used today. Meanwhile the rise of radio astronomy led to the discovery of quasars (Schmidt 1963), which are ideal sources for lensing: their large distances mean a high probability of being lensed by an intervening galaxy, yet they are bright enough to still be ordinarily detectable, and their small emission regions enable high magnifications. The first observation of gravitational lensing, of the quasar QSO 0957+561, was made by Walsh, Carswell & Weymann (1979).

Although the double images from 'point mass' lensing are still unresolvable, Chang & Refsdal (1979) and Gott (1981) noted that a star crossing the line of sight (LOS) to a source could produce a measurable temporary amplification. Paczyński (1986a,b) called this *microlensing* and showed it could be used to detect dark matter objects in the Galactic halo, from their lensing of stars in the Large Magellanic Cloud (LMC), since the halo stars alone would measurably magnify one in a million LMC stars. Such dark matter objects responsible for

[1]Measurements by the *Hipparcos* satellite have since verified Einstein's formula to within 0.3% (Froeschle, Mignard & Arenou 1997), imposing strong constraints on deviations from general relativity.

microlensing are commonly known as MACHOs (Massive Astrophysical Compact Halo Objects, Griest 1991). It was then realised that microlensing could also be observed towards the Galactic bulge, whose stars would be lensed by MACHOs and stars in the disc (*bulge-disc* lensing, Paczyński 1991; Griest 1991; Griest et al. 1991), and by other bulge stars (*bulge-bulge* lensing, also called *bulge self-lensing*, Kiraga & Paczyński 1994).

Monitoring millions of stars – with frequent sampling, and distinguishing any light curves from those due to variable stars – seemed unfeasible, but the technology advanced such that three separate collaborations were soon conducting systematic surveys: OGLE (Udalski et al. 1992), MACHO (Alcock et al. 1993) and EROS (Aubourg et al. 1993). These have been followed by other groups that are discussed later in this chapter.

There are many reviews of gravitational lensing and its various applications. Three books providing comprehensive coverage are by Schneider, Ehlers & Falco (1992), Mollerach & Roulet (2002) and Meylan et al. (2006). Articles include Refsdal & Surdej (1994), Paczyński (1996), Wu (1996), Roulet & Mollerach (1997), Narayan (1998), Wambsganss (1998), Narayan & Bartelmann (1999), Gould (2001a,b), Milsztajn (2002), Jackson, Browne & Wilkinson (2002) and Evans (2004). IAU Symposium 173 (Kochanek & Hewitt 1996) covers all aspects of lensing, and Brainerd & Kochanek (2001) present recent progess and future goals, including two reviews of microlensing by Mao (2001) and Sackett (2001).

Gravitational lensing is now split into three fields: strong lensing, involving galaxy lensing and multiple images; weak lensing, also on cosmological scales but concerning distortion of single images; and microlensing, generally within the Milky Way (see Fig. 1.1).

1.3 Basic theory of microlensing

1.3.1 Single lenses

Fig. 1.2 shows lensing by a point mass M. A light ray from a source S, passing at a distance b, the impact parameter, is deflected by an angle

$$\alpha = \frac{4GM}{bc^2}, \tag{1.1}$$

Figure 1.1: All-sky panorama of the Milky Way. The plane of the Galaxy runs horizontally through the middle, with the Galactic north at the top. The Large and Small Magellanic Clouds are seen as two fuzzy patches in the lower right quadrant. (Image courtesy of and ©Axel Mellinger).

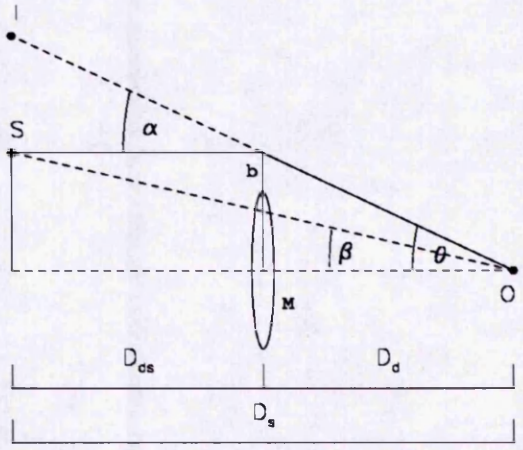

Figure 1.2: Lensing by a point mass M, which causes light rays from a source S, passing at a distance b, to be deflected by an angle α. An observer O hence sees an image I. The other symbols are defined in the text. (Adapted from Narayan & Bartelmann 1999, fig. 5).

as calculated by Einstein (1915). Hence an observer O sees an image I. The deflector (lens) and source are at distances $D_{\rm d}$ and $D_{\rm s}$, respectively, from O and are separated by $D_{\rm ds}$.

From Fig. 1.2 it is simple to derive the *lens equation*:

$$\theta - \beta = \alpha D_{\rm ds}/D_{\rm s}, \tag{1.2}$$

which is in general nonlinear, meaning that multiple light paths – and hence multiple images – may exist for one source. For a point mass lens and source, there will be only two images, on opposite sides of the source. $D_{\rm d}$, $D_{\rm s}$ and $D_{\rm ds}$ are *angular size distances*, defined by the expression

$$\text{linear separation} = \text{angular separation} \times \text{distance}. \tag{1.3}$$

Note that this is only valid in the small angle approximation, which may be used on microlensing scales. Note also that in general $D_{\rm ds} \neq D_{\rm s} - D_{\rm d}$, as this is a Euclidean relation and not obviously true in curved spacetimes, which must be considered when observing on cosmological scales. (Angular size distances are different from *luminosity distances*, which relate absolute and apparent magnitudes, by a factor $(1+z)^2$, where z is the redshift. See e.g. Peacock (1999) for more details). However, as space is locally Euclidean, we may assume here that $D_{\rm ds} = D_{\rm s} - D_{\rm d}$.

If $\beta = 0$ there will be only one image: an Einstein ring with angular radius $\theta_{\rm E}$. Substituting equation (1.1) into (1.2), with $b = \theta D_{\rm d}$, gives

$$\theta_{\rm E} = \left(\frac{4GM}{c^2} \frac{D_{\rm s} - D_{\rm d}}{D_{\rm d} D_{\rm s}} \right)^{1/2}. \tag{1.4}$$

This is the *Einstein radius*, a convenient scale in lensing geometry as shown below. Expressing equation (1.2) in terms of $\theta_{\rm E}$ we have

$$\theta - \beta = \frac{\theta_{\rm E}^2}{\theta}, \tag{1.5}$$

which has two solutions,

$$\theta_{\pm} = \frac{1}{2} \left(\beta \pm \sqrt{\beta^2 + 4\theta_{\rm E}^2} \right), \tag{1.6}$$

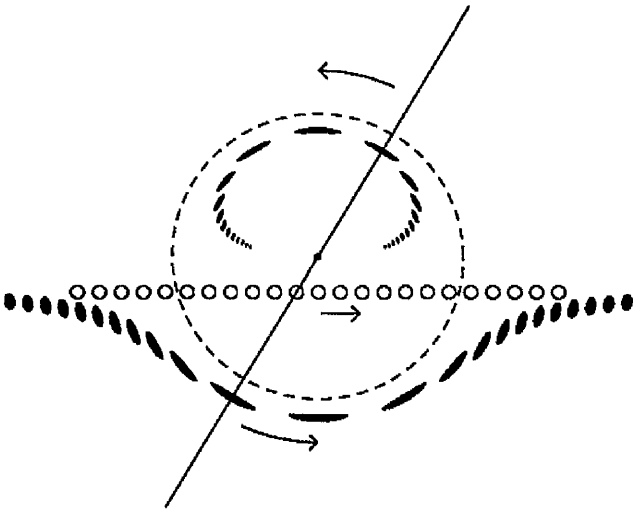

Figure 1.3: A standard microlensing event (Paczyński 1996, fig. 3). The series of open circles indicates a source passing across the Einstein ring (dashed line) of a lens (small dot). The series of dark ellipses shows the two images, which at any instant are in line with the lens and source, as indicated by the straight line.

corresponding to the two images, with one inside the Einstein ring and the other outside. Fig. 1.3 shows this geometry, with a source passing behind the lens. As the source moves away, one image approaches the lens and disappears, while the other approaches the source and tends to a magnification of unity.

This geometry cannot yet be resolved for any microlensing event, as stellar mass lenses in the Milky Way have Einstein radii of $\sim$1 mas (compared with a few μas at cosmological distances), but this should be possible with long-baseline sensitive optical interferometers (Delplancke, Górski & Richichi 2001).

Microlensing events can, however, be easily detected. Lensing conserves surface brightness (because of Liouville's theorem), but changes the apparent solid angle of a source. Hence the image amplification μ is equal to the ratio of solid angles,

$$\mu = \frac{\text{image area}}{\text{source area}}. \tag{1.7}$$

For a point mass lens, μ is given by

$$\mu_{\pm} = \left| 1 - \left(\frac{\theta_{\rm E}}{\theta_{\pm}} \right)^4 \right|^{-1} = \frac{u^2+2}{2u\sqrt{u^2+4}} \pm \frac{1}{2}, \tag{1.8}$$

where $u = \beta/\theta_{\rm E}$, the dimensionless impact parameter (in units of the Einstein radius). The difference in amplification of the two images is therefore constant,

$$\mu_+ - \mu_- = 1, \tag{1.9}$$

and the total amplification is simply the sum of the individual amplifications:

$$\mu = \mu_+ + \mu_- = \frac{u^2+2}{u\sqrt{u^2+4}}. \tag{1.10}$$

Note that for a true point mass lens the amplification is infinite ($\mu \rightarrow \infty$ as $u \rightarrow 0$). When the source lies at the Einstein radius, $\beta = \theta_{\rm E}$, $u = 1$, and

$$\mu \approx 1.17 + 0.17 \approx 1.34. \tag{1.11}$$

This is a brightening of 0.32 magnitudes (as $\Delta{\rm mag} = 2.5\log\mu$), so lenses passing within $\theta_{\rm E}$ of a source should be easily detectable. The characteristic timescale of a microlensing event, $t_{\rm E}$, is defined as the time for the lens to move relative to the source by one Einstein radius[2]:

$$t_{\rm E} = \frac{r_{\rm E}}{v} = 0.214 \text{ yrs} \left(\frac{M}{\rm M_\odot} \right)^{1/2} \left(\frac{D_{\rm d}}{10 \text{ kpc}} \right)^{1/2} \left(\frac{D_{\rm s} - D_{\rm d}}{D_{\rm s}} \right)^{1/2} \left(\frac{200 \text{ kms}^{-1}}{v} \right), \tag{1.12}$$

where v is the relative transverse velocity of the lens and source, and $r_{\rm E} = D_{\rm d}\theta_{\rm E}$ is the projection of the angular Einstein radius onto the lens plane. The $t_{\rm E}$ probability distribtion is very broad, with power-law tails (Mao & Paczyński 1996): lenses very close to either the source or observer will produce very short events, and lenses moving almost along the LOS will produce very long events. The a priori mass range for MACHOs is approximately 10^{-7}–10^4 $\rm M_\odot$, which corresponds to timescales from $\sim$1 hour to a few decades (Milsztajn 2002). Lighter primordial H/He objects would have evaporated since the Galaxy formed (De Rujula, Jetzer

[2]The MACHO collaboration includes a factor 2, defining $t_{\rm E}$ as the Einstein diameter crossing time.

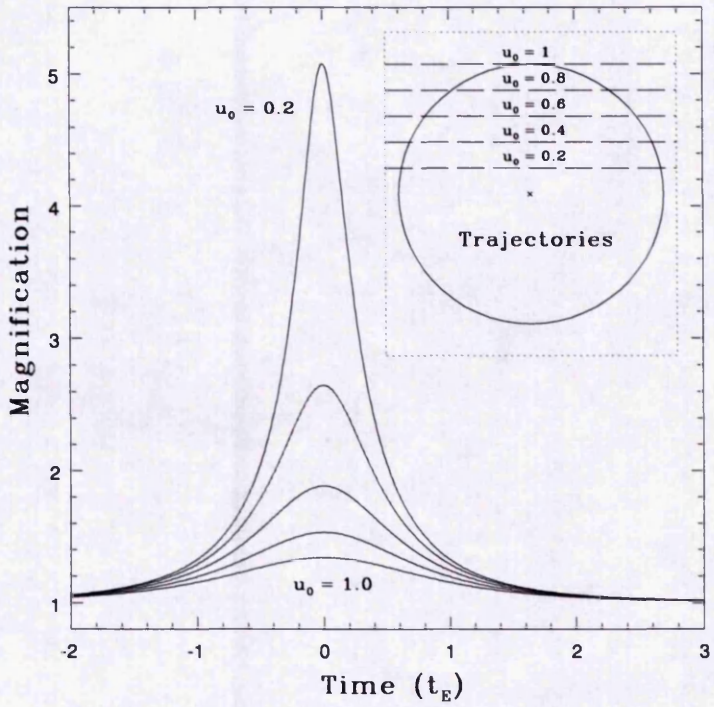

Figure 1.4: Light curves due to lensing by a point mass (Smith 2003, fig. 1.3). The curves correspond to the trajectories that are shown relative to the lens's Einstein radius (inset), with mimimum impact parameter u_0.

& Masso 1992), while a halo full of more massive bodies would have no globular clusters by now (Arras & Wasserman 1999). For most events t_E is the only measurable parameter that gives any information about the lens. Determining the t_E distribution can also reveal the lens mass function (De Rujula, Jetzer & Masso 1991; Mao & Paczyński 1996). However, a measurement of t_E will not give M, but only a combination of M, D_d, D_s and v. Ways to break this *lens mass degeneracy* are discussed in §1.4.3. Breaking the degeneracy is of great importance. It is the only known way to make direct mass measurements of isolated stars other than the Sun, as all other techniques exploit companions such as binary partners.

There is a direct correspondence between the peak magnification and u_0, the minimum impact parameter. Fig. 1.4 shows typical light curves for different values of u_0. The peak widths are $\sim t_E$.

The cross section for microlensing is defined as the area enclosed by the Einstein ring, the *Einstein circle*. Hence the probability of seeing an event, the *optical depth*, is equal to the fraction of total sky solid angle covered by the Einstein circles of all the lenses in the sky:

$$\tau = \frac{1}{\delta\omega} \int \mathrm{d}V n(D_\mathrm{d}) \pi \theta_\mathrm{E}^2, \tag{1.13}$$

where $\mathrm{d}V = \delta\omega D_\mathrm{d}^2 \mathrm{d}D_\mathrm{d}$ is the volume of an infinitesimal spherical shell of radius D_d which covers a solid angle $\delta\omega$, and $n(D_\mathrm{d})$ is the number density of lenses at D_d. Inserting equation (1.4) for θ_E, we see that the optical depth towards a given source at D_s is

$$\tau = \int_0^{D_\mathrm{s}} \frac{4\pi G\rho}{c^2} \frac{D_\mathrm{d}(D_\mathrm{s} - D_\mathrm{d})}{D_\mathrm{s}} \mathrm{d}D_\mathrm{d}, \tag{1.14}$$

where ρ is the mass density of lenses. Note that τ depends on this mass density of lenses, but not on their individual masses. Hence a measurement of τ along a particular LOS probes the total mass (including of course dark matter) in that direction, with no prior knowledge of the mass function.

Paczyński (1991) calculated the average time interval between events as

$$\langle \Delta t \rangle = \frac{\pi t_\mathrm{E}}{2\tau}. \tag{1.15}$$

The frequency of events, the *event rate*, is defined as

$$\Gamma = \langle \Delta t \rangle^{-1} = \frac{2\tau}{\pi t_\mathrm{E}} = \frac{2v\tau}{\pi} \left[\frac{4GM}{c^2} \frac{(D_\mathrm{s} - D_\mathrm{d})D_\mathrm{d}}{D_\mathrm{s}} \right]^{-1/2}. \tag{1.16}$$

1.3.2 Multiple lenses

Most disc stars are in binary pairs (e.g. Abt 1983). The fraction of binary MACHOs is unknown, but Mao & Paczyński (1991) estimated binary lenses would cause ~10% of microlensing events in the Galactic plane, consistent with OGLE observations reported by Udalski et al. (2000). Such events have more complicated light curves than those produced by single lenses, with sharp features due to *caustic* crossings. Caustics are curves in the plane of the source. When a source crosses a caustic, two images either appear or disappear (depending on the direction of crossing) somewhere on the *critical curve*, defined as the locus of points in the lens plane that are mapped by the lensing onto the caustic curve.

A point source exactly on a caustic would be infinitely magnified; for a single lens, the caustic is the single point behind the lens, and the critical curve is the Einstein ring. Sources with a finite size have a large but finite magnification. Whereas a single lens typically produces a single-peaked, symmetric light curve, double lenses may cause features such as spikes and double peaks. Fig. 1.5 shows examples of this for a binary lens composed of two equal point masses.

A detailed analysis of double star microlensing is given by Schneider & Weiss (1986). Several attempts were made to compute binary lens light curves before Mao & Di Stefano (1995) produced the first code able to fit observed data. It was applied to the first reported binary event, seen by OGLE (Udalski et al. 1994b), which is shown in Fig 1.6.

1.4 Observations

1.4.1 Microlensing surveys

The first microlensing searches were conducted by the OGLE (Optical Gravitational Lensing Experiment, Udalski et al. 1992), MACHO (Alcock et al. 1993) and EROS (Expérience pour la Recherche d'Objets Sombres, Aubourg et al. 1993) collaborations, and later DUO (Disk Unseen Objects, Alard et al. 1995). The MACHO project has been succeeded by SuperMACHO, while the OGLE survey is ongoing, along with observations by MOA (Microlensing Observations in Astrophysics, e.g. Bond et al. 2001).

These groups have collectively surveyed the Galactic bulge and the Large and Small Magellanic Clouds (SMC), the primary aim being to accurately measure the optical depth. The bulge optical depth provides a probe of the bulge's shape and structure, which are still not well understood, and measurements of τ are compared with predictions from a variety of Galactic models. Determining τ towards the LMC and SMC provides a similar probe of the halo. Another key observable is the timescale distribution, which also depends on the mass function and kinematics along the LOS.

The first microlensing detections were reported almost simultaneously by EROS (Aubourg et al. 1993), MACHO (Alcock et al. 1993, see Fig. 1.7) and OGLE (Udalski et al. 1993). Since then well over 2000 events have been recorded, with rates now at $\sim$500 per yr (e.g., Woźniak et al. 2001; Sumi et al. 2003; Afonso

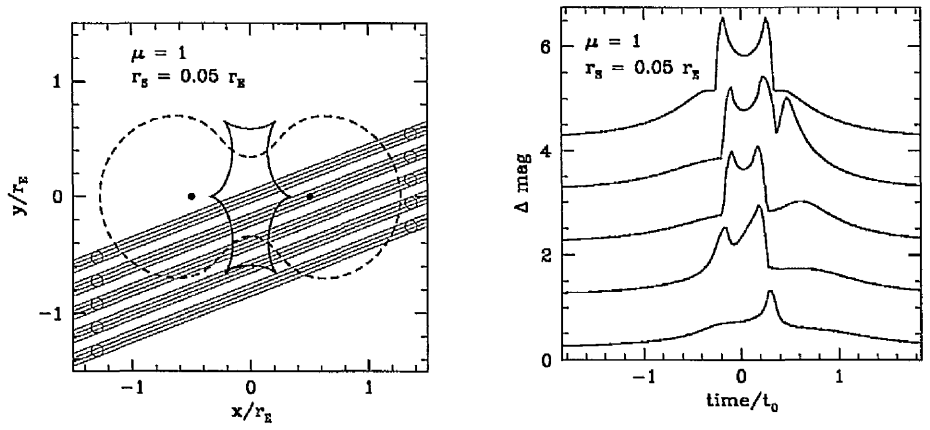

Figure 1.5: Left panel: A binary lens composed of two equal point masses, separated by one Einstein radius $r_{\rm E}$ (Paczyński 1996, fig. 7). The thick solid line with six cusps is the caustic, and the dashed line shows the corresponding critical curve. Five identical sources (open circles) of radius $r_{\rm s}$ move along the straight trajectories indicated. Right panel: The corresponding light curves for each source, (Paczyński 1996, fig. 6), with sharp spikes and double peaks due to caustic crossings. (The curves are shifted along the vertical scale for clarity).

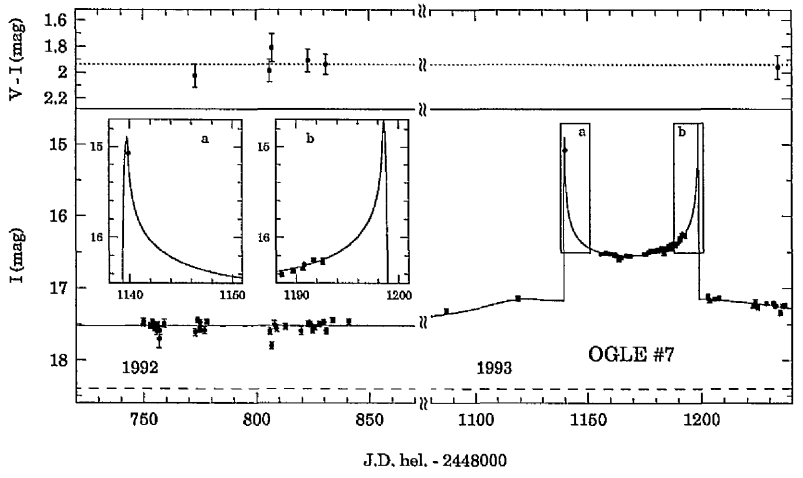

Figure 1.6: The first observed binary microlensing event, OGLE #7 (Udalski et al. 1994b, fig. 2). The boxes (a) and (b) highlight the two caustic crossings.

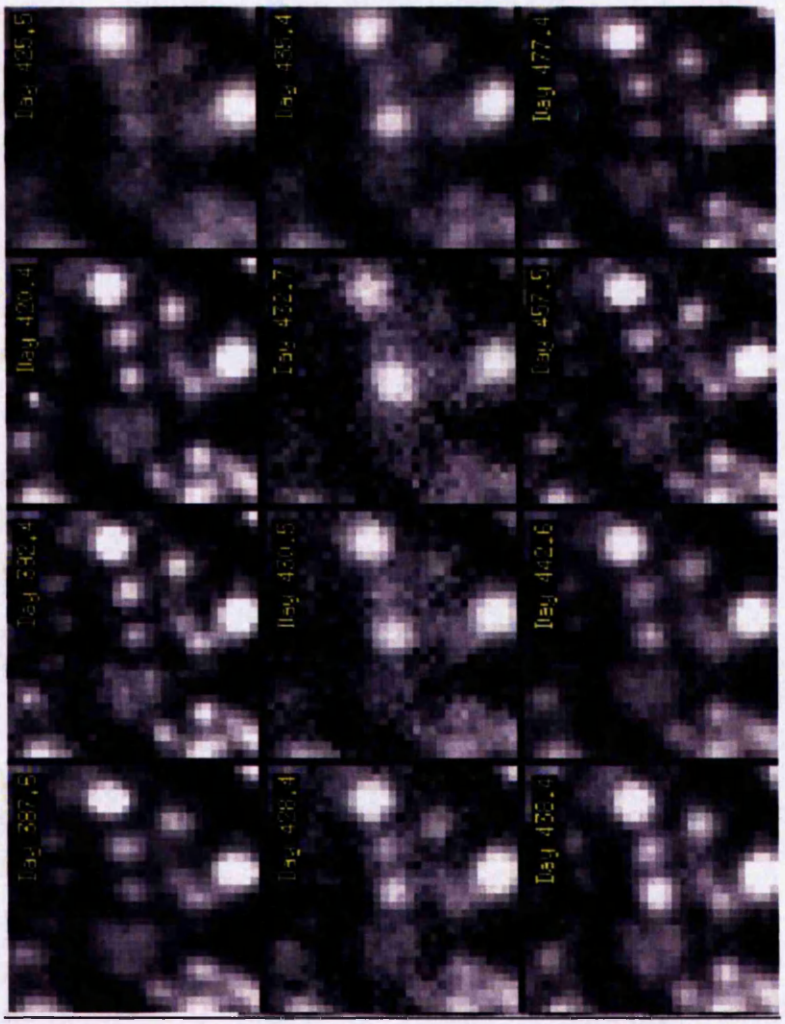

Figure 1.7: Portions of selected images of the first microlensing event to be reported by MACHO (Alcock et al. 1993, fig. 3). Each frame is centred on the lensed star.

et al. 2003b; Thomas et al. 2005). With many stellar fields being monitored, each one may be sampled only once or twice per night. Hence the survey teams post online real-time alerts of stellar brightenings consistent with microlensing. These are followed up by one or more of a second type of collaboration, who make more frequent and detailed observations. Past and present follow-up networks include GMAN (Global Microlensing Alert Network, Pratt et al. 1996), PLANET (Probing Lensing Anomalies NETwork, Albrow et al. 1996), MPS (Microlensing Planet Search, e.g Rhie et al. 1998), EXPORT (EXtra-Solar Planet Observational Research Team, Eiroa et al. 2001), and MicroFUN (Microlensing Follow-Up Network[3]).

1.4.2 Complications

Observers must distinguish microlensing events from intrinsically variable stars. In most cases the difference is clear. Lensing light curves are normally symmetric in time, achromatic (as light deflection does not depend on wavelength), and the magnification will not be repeated: the optical depth is only $\sim 10^{-6}$ towards the Galactic bulge (see §1.5.1), so the chance of a particular star being lensed more than once in a few years is negligible. In contrast, variable stars typically have asymmetric, chromatic light curves, which are repeated periodically.

However, there are several possible complications. Due to the low optical depth, microlensing surveys cover crowded fields (see Fig. 1.8). This concentration of stars increases the chances of detecting events, as an intervening lens is more likely to pass in front of a potential source. However, whilst the Einstein radii of solar mass lenses are $\sim$1 mas, a typical seeing disc is $\sim$1 arcsec. Hence an image of an apparently single star may in fact be a blend of two or more, with only one being lensed. The measured flux will then consist of both the magnified and unmagnified fluxes. This blending is a major concern in any microlensing analysis. One problem is that blended stars of different colours can cause an apparently chromatic event, as one colour temporarily dominates the blend. This was first seen by Udalski et al. (1994b). If stars in the same seeing disc are separately lensed at different times, they may be dismissed as a repeating variable star (Griest & Hu 1992). Another problem is the underestimation of the event timescale. For example, a bright star may be blended with a very faint star that

[3]www.astronomy.ohio-state.edu/~microfun/

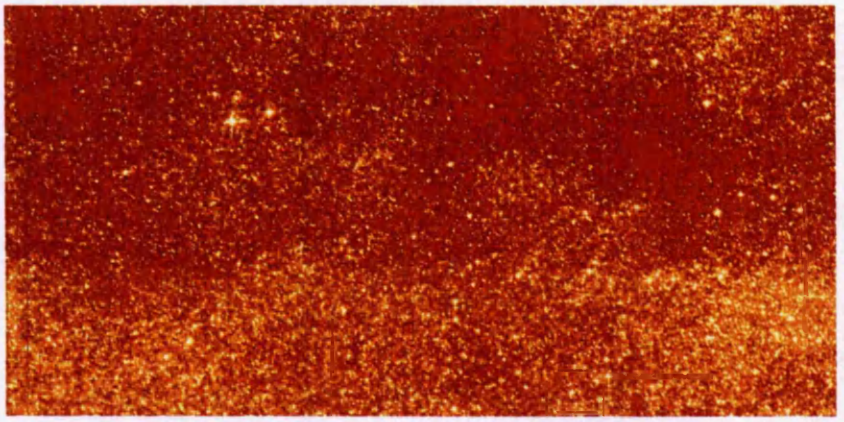

Figure 1.8: A section of one of the MOA bulge fields. The image is in false colour, and is approximately 1/12th the total field of view of the MOA telescope. (Image courtesy of the MOA collaboration).

is lensed. Only at its peak amplification does the faint star's flux become a significant fraction of the blend, and the light curve is detected. However, only the tip of the curve has been seen, and the measured timescale, wrongly attributed to the bright star, is too short.

Of course, sources will also be blended with their stellar lenses, but this is not a significant problem: most lens stars are expected to be low mass, and hence very faint or undetectable (e.g., Kamionkowski 1995; Buchalter, Kamionkowski & Rich 1996). In fact, only one direct detection of a microlens has so far been published, towards the LMC (Alcock et al. 2001). This event, *MACHO-LMC-5*, is discussed further in §1.4.3. The first direct detection of a microlens towards the bulge is analysed in chapter 5.

Two observational strategies have been deployed to overcome or minimise the effects of blending. One is to concentrate on lensing of bright stars, such as clump giants, which it was assumed are negligibly affected by blending. The more recent measurements of τ have been based on such events, which constitute only a small subset of the complete event databases. These measurements are discussed in detail in §1.5.1. However, Sumi et al. (2006) found $\sim$38% of events from OGLE-II (the second OGLE phase) with apparent red clump giant (RCG) sources were really due to faint stars blended with a bright companion. Fortunately, there is actually little effect on estimates of τ, due to partial cancellation of blending's different effects (Popowski et al. 2005; Sumi et al. 2006; Hamadache

et al. 2006). Timescale distributions, though, will be significantly shifted towards shorter events, and must be appropriately corrected. Note another reason for using only RCG events: observers measuring τ towards the bulge wish to consider lensing of bulge stars only, but stars in that direction may not lie in the bulge itself. RCGs have a well-defined position in the colour-magnitude diagram (CMD), which ensures they are most likely located in the bulge. Hence foreground and background contamination can be virtually eliminated.

The second anti-blending strategy is to use difference image analysis (DIA), also known as pixel lensing, rather than standard photometric fitting (e.g. Alard & Lupton 1998). This technique involves subtracting subsequent images of the same field from each other, revealing only the varying part of the flux. The principle advantages are that it can detect lensing of stars that are too faint to be seen when unlensed, and is less sensitive to the systematics of blending (Sumi et al. 2006). These advantages may be exploited fully in an analysis including all stars along the LOS, rather than just RCGs. However, as mentioned above, when measuring τ towards the bulge, only bulge sources should be considered. Hence in this case, it is assumed the observed star counts are dominated by the bulge and foreground disc, and a correction is made for the fraction $f_{\rm disc}$ of disc sources. This increases τ by $\sim$25% (e.g., Alcock et al. 2000a; Sumi et al. 2003). However the application, and size, of this correction is somewhat controversial.

1.4.3 Useful complications: breaking the lens mass degeneracy

Similar blending effects to those described above may also occur with binary sources, though Griest & Hu (1992) state that most binary source events should be achromatic and similar to single source light curves. A more likely source of complications is binary lenses. The light curves shown in Figs. 1.5 and 1.6 are examples of the 'resonant' case, where two lenses of similar mass are separated by about one Einstein radius. Non-resonant lenses are well separated and act almost independently, possibly causing an event to apparently repeat, but this should occur in only a few per cent of all events (Di Stefano & Mao 1996).

Of course, stars are not really point masses. For sources larger than the impact parameter of a single lens, or the caustic of a binary, their finite size significantly modifies the light curve (e.g., Nemiroff & Wickramasinghe 1994; Witt & Mao

1994). Measurement of this effect may enable study of the light distribution across the source, the limb darkening and spots (e.g., Witt 1995; Albrow et al. 2001; Abe et al. 2003; Rattenbury & Mao 2006, see also Dominik 2004). More importantly, it may yield the relative proper motion of the lens-source system (Gould 1994a). If v is known, the lens mass degeneracy can be partially broken.

Another important effect is parallax: if the relative transverse velocity of the lens, source and observer is not constant during an event, the light curve can become asymmetric. Parallax due to the Sun's acceleration of the Earth was predicted by Gould (1992) and first observed by Alcock et al. (1995). If detected, this extra observable can further help to break the lens mass degeneracy. Alcock et al. (1995) were thus able to estimate the mass of a lens, but with low precision. Parallax may be more easily detected if Earth-based observations are combined with those from telescopes in space (Gould 1994b). With two vantage points separated by $\sim$1 AU, different light curves can be seen for the same event, enabling an accurate parallax measurement. However, Smith, Mao & Paczyński (2003, see also Smith et al. 2005) described three degeneracies associated with parallax. One involves similar light curve distortions arising from both parallax and blending. Another is called *xallarap*: acceleration of the source (by a binary companion) can cause distortions that mimic parallax caused by the Earth's acceleration. Poindexter et al. (2005) carried out a systematic analysis of 22 candidate parallax events and found 23% were strongly affected by xallarap.

It is possible to completely break the degeneracy and accurately measure the lens mass. This was first achieved by An et al. (2002), for an EROS binary lens event towards the bulge that included caustic-crossing and finite source effects. It is possible because space-based telescopes can help again, after an event has occured. With their superior resolution, it may be only a few years before a lens has moved sufficiently far away (in projection) from the source for both to be resolved. This enables a direct, and more accurate, measurement of the relative proper motion. Gould, Bennett & Alves (2004) combined their light curve measurements of the MACHO-LMC-5 event (referred to in §1.4.2) with *Hubble Space Telescope* follow-up observations, to produce the most precise mass measurement of an isolated star other than the Sun. Gould (2004), building on the work of Smith, Mao & Paczyński (2003), showed that there exists another, *jerk-parallax* degeneracy, where jerk refers to the non-uniform acceleration of the Sun. However, only one of the jerk-parallax solutions for the MACHO LMC event

was consistent with photometric estimations.

Lens mass measurements remain rare. Only one other has been published: Jiang et al. (2004) were able to make a crude estimation for an OGLE event towards the bulge, and they discuss the difficulties of finding events that allow lens mass measurements. Han & Chang (2003) predicted that lenses should be resolved for ~22% of bulge-disc events with follow-up observations after 10 yrs using the *Next Generation Space Telescope* (now the *James Webb Space Telescope*).

Astrometric microlensing (e.g. Walker 1995) provides another means of determining the lens mass. As explained in §1.3.1, the two lensed images cannot yet be resolved. However, with sufficient resolution one can measure the shift of the image centroid during an event, or even fully resolve the lensing geometry. This may become feasible with the *Very Large Telescope Interferometer* (Delplancke, Górski & Richichi 2001) and the *Gaia* satellite (Belokurov & Evans 2002). Gould (2003) states that observations with the future *Space Interferometry Mission* satellite will allow hundreds of lens mass measurements, with up to 1% accuracy. This would yield the first determination of the bulge mass function.

1.5 Measuring the optical depth

A microlensing survey will typically monitor a few tens of fields, each $\sim 1\,\mathrm{deg}^2$, a few times per night for several years. τ cannot be calculated from the observational data using equation (1.14). The required formula is given by e.g. Hamadache et al. (2006):

$$\tau = \frac{\pi}{2u_0(\mathrm{max})} \frac{\sum_{i=1}^{N_{\mathrm{ev}}} t_{\mathrm{E},i}/\epsilon(t_{\mathrm{E},i})}{\sum_{j=1}^{N_*} T_j}, \tag{1.17}$$

where each event i has a timescale $t_{\mathrm{E},i}$ and detection efficiency $\epsilon(t_{\mathrm{E},i})$, each monitored star j is observed for a time T_j, the total numbers of events and stars are N_{ev} and N_*, respectively, and $u_0(\mathrm{max})$ is the maximum impact parameter of all the observed events.

The detection efficiency $\epsilon(t_{\mathrm{E},i})$ is the fraction of events with timescale t_{E} that are successfully recovered from the data, after all the necessary cuts have been made. Accurately estimating the efficiency is therefore a crucial part of the analysis. This is essentially done by adding artificial events to the databases, and

seeing how many pass the same cuts. $\epsilon(t_{\mathrm{E},i})$ varies significantly with t_{E}: events too short to be seen by a few observations per night will be missed, as will (less common) events that are longer than the period of the survey. See e.g. Sumi et al. (2006) for a detailed example of computing $\epsilon(t_{\mathrm{E},i})$.

1.5.1 The Galactic bulge

Original theoretical estimates, considering bulge-disc lensing, predicted $\tau < 10^{-6}$ (Paczyński 1991; Griest et al. 1991). Kiraga & Paczyński (1994) realised that bulge self-lensing is dominant, but predictions were still significantly below the first observed values: OGLE estimated $\tau \geq 3.3 \pm 1.2 \times 10^{-6}$ from 9 events towards Baade's window (BW) – at $(l, b) = (1.0°, -3.9°)$ – and nearby bulge fields (Udalski et al. 1994a). MACHO's first result used 13 clump giant events and an efficiency calculation. They found $\tau = 3.9^{+1.8}_{-1.2} \times 10^{-6}$ at $(l, b) = (2.55°, -3.64°)$, and noticed a significant increase in τ with decreasing $|b|$ (Alcock et al. 1997).

Axisymmetric Galactic models predicted $\tau \approx 1\text{–}1.2 \times 10^{-6}$ (e.g., Kiraga & Paczyński 1994; Evans 1994). Paczyński et al. (1994) proposed that the bulge is in fact a bar, inclined in the plane by $\sim$15° to our LOS. They noted that Stanek et al. (1994) had seen a difference of $\sim$0.37 magnitudes in the extinction-corrected apparent magnitudes of RCGs in two OGLE fields at $l = \pm 5°$. Assuming the RCGs' intrinsic luminosity distributions were the same in both locations, this implied a bar structure for the bulge. Including such a bar in Galactic models lengthens the average LOS from lens to source, and so increases τ. Although there had long been evidence for a bar (e.g. De Vaucouleurs 1964), it was only in the 1990s that the combined evidence from the NIR light distribution, source count asymmetries, gas kinematics and large optical depth had convinced most people of its existence (see e.g. Gerhard 2002, and references therein).

Numerous models including bars and other effects were developed (e.g., Zhao, Spergel & Rich 1995; Metcalf 1995; Zhao, Rich & Spergel 1996; Zhao & Mao 1996; Stanek et al. 1997; Bissantz et al. 1997; Gyuk 1999; Nair & Miralda-Escudé 1999; Grenacher et al. 1999; Sevenster & Kalnajs 2001), and used to predict optical depth maps and timescale distributions. However, they could not reasonably increase the predicted τ enough. Binney, Bissantz & Gerhard (2000) showed that the measured optical depths could not be plausibly reconciled with the standard Galactic models.

Alcock et al. (2000a) produced another high measurement – the first to use

DIA – of $\tau = 3.23^{+0.52}_{-0.50} \times 10^{-6}[0.75/(1 - f_{\rm disc})]$ at $(l, b) = (2.68°, -3.35°)$, from 99 MACHO events. Lower values came with measurements based on RCGs. Popowski et al. (2001) conducted a preliminary analysis of 52 clump giant MACHO events, obtaining $\tau = 2.0 \pm 0.4 \times 10^{-6}$ at $(l, b) = (3.9°, -3.8°)$. New bulge optical depth maps were then produced by Evans & Belokurov (2002) and Bissantz & Gerhard (2002). They and Han & Gould (2003) predicted $\tau \approx 1$–2×10^{-6} towards BW.

The latest measurements based on RCGs are consistent with these predictions. Afonso et al. (2003b) reported $\tau = 0.94 \pm 0.30 \times 10^{-6}$ at $(l, b) = (2.5°, -4.0°)$ from 16 EROS events. Popowski et al. (2005) updated their previous preliminary analysis, now using 62 MACHO events, to measure $\tau = 2.17^{+0.47}_{-0.38} \times 10^{-6}$ at $(l, b) = (1.50°, -2.68°)$, (though this value was based on a subsample of 42 events). With 32 events from the OGLE-II survey, Sumi et al. (2006) found $\tau = 2.55^{+0.57}_{-0.46} \times 10^{-6}$ at $(l, b) = (1.16°, -2.75°)$. These measurements are consistent with each other when adjusted for variations in latitude and longitude – as well as giving τ for the average coordinates of the survey fields, optical depth trends with l and b are also now routinely published. The most recent measurement comes from Hamadache et al. (2006). They used 120 EROS-2 events, spread over such a wide area that an average τ has little meaning. Therefore they gave $\tau = (1.62 \pm 0.23) \exp[-a(|b| - 3 \text{ deg})] \times 10^{-6}$, where $a = (0.43 \pm 0.16 \text{ deg}^{-1})$, in the latitude range $1.4° < |b| < 7.0°$. This is also consistent with the other recent RCG measurements.

However, the latest 'all-star' value is still significantly higher: Sumi et al. (2003) reported $\tau = 3.36^{+1.11}_{-0.81} \times 10^{-6}\,[0.77/(1 - f_{\rm disc})]$ based on 28 MOA events, at $(l, b) = (3.0°, -3.8°)$ (coordinates given by Sumi et al. 2006). This is consistent with the previous all-star optical depth from Alcock et al. (2000a). The discrepancy between RCG- and all-star-based measurements has yet to be explained.

1.5.2 The Magellanic Clouds

Lensing of stars in the LMC and SMC provides a valuable probe of the Galactic halo. The clouds are sufficiently near to us that relatively small ground-based telescopes can resolve tens of millions of stars, and far enough away that microlensing surveys will sample a sizeable fraction of the halo. The optical depths (and hence event rates) towards the clouds are lower than towards the bulge, with $\tau \sim 10^{-7}$. The latest measurements towards the LMC, by MACHO (Alcock et al.

2000b) and EROS (Tisserand et al. 2006), place contradictory limits on the halo fraction composed of MACHOs. These conclusions were based on 13–17 events[4] and 1 event, respectively. Of the MACHO group's events, one has been shown to be a variable star, and others due to LMC self-lensing or Galactic disc lensing – see e.g. the discussion by Tisserand et al. (2006), and references therein. The analysis by Tisserand et al. was the first of Magellanic lensing to use only bright stars, as is commonly done with bulge lensing, and they discuss possible problems arising from the inclusion of faint stars in previous calculations. Further analyses of the LMC's stellar halo, dark matter halo, and an apparent bar structure in the LMC are given by Alves (2004), Calchi Novati et al. (2006) and Zhao & Evans (2000), respectively.

Most publications on Magellanic lensing have focused on the LMC. Although the SMC offers fewer stars and events, it provides a useful second LOS through the halo. See e.g. Afonso et al. (2003a), who report 5 candidate events towards the SMC.

1.6 Other interesting results and prospects

1.6.1 Planets

Multiple lenses of particular interest are planetary systems. A planet orbiting a lens star will superimpose perturbations on the light curve caused by the star. These perturbations have timescales of a few hours or days, compared to typical stellar lensing timescales of a few tens of days. Smaller planets produce shorter, but not weaker, perturbations.

Mao & Paczyński (1991) suggested that microlensing searches could lead to the first detection of extra-solar planets, but this was soon achieved by pulsar timing (Wolszczan & Frail 1992). Well over 100 planets have now been found by the radial velocity and transit techniques (e.g. Perryman & Hainaut 2005). However, microlensing is the only method sufficiently sensitive to detect Earth-mass bodies. Observations of the light curve peaks in high magnification events are particularly sensitive to planets (e.g. Bond et al. 2002). Another obvious and unique advantage of microlensing is that it does not require planets to have a host star at all, and is therefore the only way to detect free-floating interstellar

[4]Depending on the selection criteria.

planets. Two reviews of planetary microlensing are given by Wambsganss (2004) and Gould (2005). A few tens of candidate or confirmed planets have also been found from transits of sources in the lensing surveys (e.g. Silva & Cruz 2006).

In recent years four secure planetary microlensing detections have been made, with planet masses $M_{\rm p}$ of $1.5^{+0.1}_{-1.2}$ $\rm M_{Jupiter}$, $0.05 \leq M_{\rm p}/\rm M_{Jupiter} \leq 4$, $5.5^{+5.5}_{-2.7}$ $\rm M_{\oplus}$ and $\sim$13 $\rm M_{\oplus}$ – see e.g. the latest review by Rattenbury (2006). Han & Han (2002) even considered the detection of satellites around lensing planets, but concluded that any signatures in the light curves would be severely smeared out by the finite source effect.

RoboNet is a prototype network of robotic telescopes that aims to detect planetary microlensing[5]. However the best chances of large-scale planetary detections from lensing lie with space-based telescopes, which have several advantages. Whereas ground-based observations of the bulge and Magellanic clouds are nightly, seasonal and subject to bad weather, satellite telescopes can observe events and fields continously, with better photometric accuracy. The *Microlensing Planet Finder* is a proposed satellite mission that will, according to Bennett et al. (2004), complete the first census of extrasolar planets, with sensitivity to planets like those in our own solar system. It would detect bodies of $0.1\rm M_{\oplus}$, and Earth-like planets at all separations from 0.7 AU to infinity.

1.6.2 Other uses

The many years of microlensing surveys have created vast databases of multi-band photometry of millions of stars. Thousands of clump giants, and pulsating, eclipsing and other variables have been catalogued, enabling valuable studies of these stars. Paczyński (1996) describes some of the important earlier results. It is possible to use the magnification from lensing to obtain high quality stellar spectra, which would normally be difficult for faint stars. This has been done by e.g. Minniti et al. (1998). Accurate CMDs and extinction maps have been generated (e.g., Udalski et al. 2002; Sumi 2004). Belokurov, Evans & Du (2003) have developed neural networks to automatically classify variable light curves as microlensing events or other phenomena.

[5]www.astro.livjm.ac.uk/RoboNet/

1.6.3 Rare and extra-galactic lensing

As more events are recorded, rare and very exotic types are seen. For example, Mao et al. (2002) found the longest ever event, with $t_{\rm E} = 640$ days, and suggested the lens could be a stellar black hole. Agol et al. (2002) calculated the probability of this as 76%, and similarly 16% and 4% for the next two longest events recorded (see also Bennett et al. 2002). Smith et al. (2002) found the first multiple peak parallax event, concluding that the multiple peaks were most likely due to parallax effects combined with the lens's slow relative transverse velocity – the slowest yet reported.

Two exceptionally high magnification events were analysed by Abe et al. (2004) and Dong et al. (2006), with amplification factors of 500 and 3000, respectively. In the latter case, observations over the peak of the light curve would have had some sensitivity to Earth-mass planets. Rattenbury et al. (2005) analysed an event where the lens was a close binary whose centre-of-mass passed almost directly in front of the source star. This meant that the source was temporaily closely bounded on all sides by a caustic of the lens, allowing the oblateness of the source star to be constrained.

Wyrzykowski et al. (2006) conducted the first systematic search for microlensing events with variability in their baselines – e.g. lensing of variable stars – finding them to be quite common ($\sim$10% of the total number of constant baseline events). They also found that this new type of exotic event can allow the determination of extra event parameters.

Observations have been carried out towards the spiral arms, e.g. Derue et al. (2001) have presented 7 candidate EROS events. The Andromeda Galaxy, M31, has long been considered as another target for microlensing surveys (e.g. Crotts 1992), and searches are being conducted for lensing in its halo. In total about two dozen candidate events have been reported by the WeCaPP (Wendelstein Calar Alto Pixellensing Project, Riffeser et al. 2003) group, the VATT/Colombia (Vatican Advanced Technology Telescope, Uglesich et al. 2004) survey, the POINT-AGAPE (Pixel Observation on Isaac Newton Telescope – Andromeda Galaxy and Amplified Pixels Experiment, Calchi Novati et al. 2005) group, and the Nainital (Joshi et al. 2005) and MEGA (Microlensing Exploration of the Galaxy and Andromeda, De Jong et al. 2006) collaborations. Paulin-Henriksson et al. (2002) reported the first candidate inter-galactic event: lensing of an M31 source by an object in M32. The Angstrom Project (Andromeda Galaxy Stellar Robotic

Microlensing, Kerins et al. 2006) aims to use stellar microlensing events to trace the structure and composition of the inner regions of Andromeda.

1.7 Thesis outline

Chapter 2 presents microlensing calculations for a new Galactic model. Maps and distributions of optical depth and event timescale are predicted, and compared with the latest observational measurements. Expressions are derived for the asymptotic behaviour of the timescale distribution, in both the long and short tails, in terms of the lens mass. Various event rate distributions are predicted, and new estimates are calculated of the fraction of luminous lenses that should be detected with event follow-up observations, under different selection criteria.

Chapter 3 considers the discrepancies in optical depth measurements obtained from RCGs and from all stars, and investigates the effects of their different flux limits. τ is predicted as a function of source magnitude, and the resulting trends are explained and compared with the latest EROS data. Combining the optical depth predictions with observed values, constraints are placed on the inclination angle of the Galactic bar.

Chapter 4 examines the stellar proper motions and velocity dispersions in the Galactic bulge. Building on a relatively simple kinematic model, we see how each stage of development brings the predicted trends closer to those observed in several MACHO survey fields. The sensitivity of event timescale predictions to the different kinematic assumptions is then considered.

Chapter 5 presents an analysis of the first direct detection of a microlens towards the Galactic bulge. A maximum likelihood method is used to constrain the lens mass, and the distances to the lens and source. The relative influence of each observational constraint is also shown.

Finally, chapter 6 gives an overall summary and conclusions, with a brief look at future prospects connected to this work.

References

Abe F. et al., 2003, A&A, 411, L493

Abe F. et al., 2004, Sci, 305, 1264

Abt H.A., 1983, ARA&A, 21, 343

Afonso C. et al., 2003a, A&A, 400, 951

Afonso C. et al., 2003b, A&A, 404, 145

Agol E., Kamionkowski M., Koopmans L.V.E., Blandford R.D., 2002, ApJ, 576, L131

Alard C., Lupton R.H., 1998, ApJ, 503, 325

Alard C., Guibert J., Bienayme O., Valls-Gabaud D., Robin A.C., Terzan A., Bertin E., 1995, The Messenger, 80, 31

Albrow M. et al., 1996, in Kochanek C.S., Hewitt J.N., eds, IAU Symp. 173, Astrophysical Applications of Gravitational Lensing, Kluwer, Dordrecht, p. 227

Albrow M.D. et al., 2001, ApJ, 549, 759

Alcock C. et al., 1993, Nat, 365, 621

Alcock C. et al., 1995, ApJ, 454, L125

Alcock C. et al., 1997, ApJ, 479, 119

Alcock C. et al., 2000a, ApJ, 541, 734

Alcock C. et al., 2000b, ApJ, 542, 281

Alcock C. et al., 2001, Nat, 414, 617

Alves D.R., 2004, ApJ, 601, L151

An J.H. et al., 2002, ApJ, 572, 521

Arras P., Wasserman I., 1999, MNRAS, 306, 257

Aubourg E. et al., 1993, Nat, 365, 623

Belokurov V.A., Evans N.W., 2002, MNRAS, 331, 649

Belokurov V., Evans N.W., Du Y.L., 2003, MNRAS, 341, 1373

Bennett D.P. et al., 2002, ApJ, 579, 639

Bennett D.P. et al., 2004, BAAS, 36, 1356

Binney J., Bissantz N., Gerhard O., 2000, ApJ, 537, L99

Bissantz N., Gerhard O., 2002, MNRAS, 330, 591

Bissantz N., Englmaier P., Binney J., Gerhard O., 1997, MNRAS, 289, 651

Bond I.A. et al., 2001, MNRAS, 327, 868

Bond I.A. et al., 2002, MNRAS, 331, L19

Brainerd T.G., Kochanek C.S., 2001, eds, ASP Conf. Ser. 237, Gravitational Lensing: Recent Progress and Future Goals, Astron. Soc. Pac., San Francisco

Buchalter A., Kamionkowski M., Rich R.M., 1996, ApJ, 469, 676

Calchi Novati S. et al., 2005, A&A, 443, 911

Calchi Novati S., De Luca F., Jetzer P., Scarpetta G., 2006, A&A, accepted, preprint astro-ph/0607358

Chang K., Refsdal S., 1979, Nat, 282, 561

Chwolson O., 1924, Astron. Nachrichten, 221, 329

Crotts A.P.S., 1992, ApJ, 399, L43

De Jong J.T.A. et al., 2006, A&A, 446, 855

De Rujula A., Jetzer P., Masso E., 1991, MNRAS, 250, 348

De Rujula A., Jetzer P., Masso E., 1992, A&A, 254, 99

De Vaucouleurs G., 1964, IAU Symp. 20, The Galaxy and the Magellanic Clouds, 20, 195

Delplancke F., Górski K.M., Richichi A., 2001, A&A, 375, 701

Derue F. et al., 2001, A&A, 373, 126

Di Stefano R., Mao S., 1996, ApJ, 457, 93

Dominik M., 2004, MNRAS, 352, 1315

Dong S. et al., 2006, ApJ, 642, 842

Dyson F.W., Eddington A.S., Davidson C.R., 1920, Mem. R. Astron. Soc., 287, 733

Eddington A.S., 1920, Cambridge Science Classics, University Press, Cambridge

Einstein A., 1911, Annalen der Physik, 35, 898

Einstein A., 1915, Sitzungsber. König. Preuß. Akad. Wissensch. (Berlin), p. 831

Einstein A., 1936, Sci, 84, 506

Eiroa C., et al., 2001, A&A, 365, 110

Evans N.W., 1994, ApJ, 437, L31

Evans N.W., 2004, in Clemens D., Shah R., Brainerd T., eds, ASP Conf. Ser. 317, Milky Way Surveys: The Structure and Evolution of our Galaxy, Astron. Soc. Pac., San Francisco, p. 165

Evans N.W., Belokurov V., 2002, ApJ, 567, L119

Froeschle M., Mignard F., Arenou F., 1997, ESA SP-402, Hipparcos – Venice '97, 49

Gerhard O., 2002, in Da Costa G.S., Jerjen H., eds, ASP Conf. Ser. 273, The Dynamics, Structure & History of Galaxies: A Workshop in Honour of Professor Ken Freeman, Astron. Soc. Pac., San Francisco, p. 73

Gott III J.R., 1981, ApJ, 243, 140

Gould A., 1992, ApJ, 392, 442

Gould A., 1994a, ApJ, 421, L71

Gould A., 1994b, ApJ, 421, L75

Gould A., 2001a, Publ. Astron. Soc. Pac., 113, 903

Gould A., 2001b, in Menzies J.W., Sackett P.D., eds, SP Conf. Ser. 239, Microlensing 2000: A New Era of Microlensing Astrophysics, Astron. Soc. Pac., San Francisco, p. 3

Gould A., 2003, in Ikeuchi S., Hearnshaw J., Hanawa T., eds, ASP Conf. Ser. 289, Proc. IAU 8th Asian-Pacific Regional Meeting, Volume I, p. 453

Gould A., 2004, ApJ, 606, 319

Gould A., 2005, New Astron. Rev., 49, 424

Gould A., Bennett D.P., Alves D.R., 2004, ApJ, 614, 404

Grenacher L., Jetzer P., Strässle M., De Paolis F., 1999, A&A, 351, 775

Griest K., 1991, ApJ, 366, 412

Griest K., Hu W., 1992, ApJ, 397, 362 (Erratum: 1993, ApJ, 407, 440)

Griest K. et al., 1991, ApJ, 372, L79

Gyuk G., 1999, ApJ, 510, 205

Hamadache C. et al., 2006, A&A, 454, 185

Han C., Chang H.-Y., 2003, MNRAS, 338, 637

Han C., Gould A., 2003, ApJ, 592, 172

Han C., Han W., 2002, ApJ, 580, 490

Jackson N., Browne I., Wilkonson P., 2002, in Stone W.R., ed, Review of Radio Science 1999–2002, IEEE Press, Piscataway, New Jersey, p. 831

Jiang G. et al., 2004, ApJ, 617, 1307

Joshi Y.C., Pandey A.K., Narasimha D., Sagar R., 2005, A&A, 433, 787

Kamionkowski M., 1995, ApJ, 442, L9

Kerins E., Darnley M.J., Duke J.P., Gould A., Han C., Jeon Y.-B., Newsam A., Park B.-G., 2006, MNRAS, 365, 1099

Kiraga M., Paczyński B., 1994, ApJ, 430, L101

Klimov Y.G., 1963, Sov. Phys. Doklady, 8, 119

Kochanek C.S., Hewitt J.N., 1996, eds, IAU Symp. 173, Astrophysical Applications of Gravitational Lensing, Kluwer, Dordrecht

Liebes Jr. S., 1964, Phys. Rev., 133, B835

Mao S., 2001, in Brainerd T.G., Kochanek C.S., eds, ASP Conf. Ser. 237, Gravitational Lensing: Recent Progress and Future Goals, Astron. Soc. Pac., San Francisco, p. 215

Mao S., Di Stefano R., 1995, ApJ, 440, 22

Mao S., Paczyński B., 1991, ApJ, 374, L37

Mao S., Paczyński B., 1996, ApJ, 473, 57

Mao S. et al., 2002, MNRAS, 329, 349

Metcalf R.B., 1995, AJ, 110, 869

Meylan G., Jetzer P., North P., Schneider P., Kochanek C.S., Wambsganss J., 2006, Saas-Fee Advanced Course 33: Gravitational Lensing: Strong, Weak and Micro, Springer, Berlin

Milsztajn A., 2002, Space Science Reviews, 100, 103

Minniti D., Vandehei T., Cook K.H., Griest K., Alcock C., 1998, ApJ, 499, L175

Mollerach S., Roulet E., 2002, Gravitational Lensing and Microlensing, World Scientific Publishing, Singapore

Nair V., Miralda-Escudé J., 1999, ApJ, 515, 206

Narayan R., 1998, New Astron. Rev., 42, 73

Narayan R., Bartelmann M., 1999, in Dekel A., Ostriker O., eds, Proc. 1995 Jerusalem Winter School, Formation of Structure in the Universe, Cambridge University Press, Cambridge, p. 360

Nemiroff R.J., Wickramasinghe W.A.D.T., 1994, ApJ, 424, L21

Paczyński B., 1986a, ApJ, 301, 503

Paczyński B., 1986b, ApJ, 304, 1

Paczyński B., 1991, ApJ, 371, L63

Paczyński B., 1996, ARA&A, 34, 419

Paczyński B., Stanek K.Z., Udalski A., Szymański M., Kałużny J., Kubiak M., Mateo M., Krzemiński W., 1994, ApJ, 435, L113

Paulin-Henriksson S. et al., 2002, ApJ, 576, L121

Peacock J.A., 1999, Cosmological Physics, Cambridge University Press, Cambridge

Perryman M., Hainaut O., 2005, Extra-solar planets, ESA-ESO Working Groups Report No. 1, ESA and ESO, preprint astro-ph/0506163

Poindexter S., Afonso C., Bennett D.P., Glicenstein J.-F., Gould A., Szymański M.K., Udalski A., 2005, ApJ, 633, 914

Popowski P. et al., 2001, in Menzies J.W., Sackett P.D., eds, ASP Conf. Ser. Vol. 239, Microlensing 2000: a New Era in Microlensing Astrophysics, Astron. Soc. Pac., San Francisco, p. 244

Popowski P. et al., 2005, ApJ, 631, 879

Pratt M.R. et al., 1996, in Kochanek C.S., Hewitt J.N., eds, IAU Symp. 173, Astrophysical Applications of Gravitational Lensing, Kluwer, Dordrecht, p. 221

Rattenbury N.J., 2006, Modern Phys. Letters A, 21, 919

Rattenbury N.J., Mao S., 2006, MNRAS, 365, 792

Rattenbury N.J. et al., 2005, A&A, 439, 645

Refsdal S., 1964, MNRAS, 128, 295

Refsdal S., Surdej J., 1994, Rep. Prog. Phys., 57, 117

Renn J., Sauer T., Stachel J., 1997, Sci, 275, 184

Rhie S.H. et al., 1998, BAAS, 30, 1415

Riffeser A., Fliri J., Bender R., Seitz S., Gössl C.A., 2003, ApJ, 599, L17

Roulet E., Mollerach S., 1997, Phys. Rep., 279, 67

Sackett P.D., 2001, in Brainerd T.G., Kochanek C.S., eds, ASP Conf. Ser. 237, Gravitational Lensing: Recent Progress and Future Goals, Astron. Soc. Pac., San Francisco, p. 227

Schmidt M., 1963, Nat, 197, 1040

Schneider P., Weiss A., 1986, A&A, 164, 237

Schneider P., Ehlers J., Falco E.E., 1992, Gravitational Lenses, Springer-Verlag, Berlin

Sevenster M.N., Kalnajs A.J., 2001, AJ, 122, 885

Silva A.V.R., Cruz P.C., 2006, ApJ, 642, 488

Smith M.C., 2003, PhD thesis, Univ. Manchester

Smith M.C. et al., 2002, MNRAS, 336, 670

Smith M.C., Mao S., Paczyński B., 2003, MNRAS, 339, 925

Smith M.C., Belokurov V., Evans N.W., Mao S., An J.H., 2005, MNRAS, 361, 128

Soldner J., 1804, Berliner Astron. Jahrb., p. 161

Stanek K.Z., Mateo M., Udalski A., Szymański M., Kałużny J., Kubiak M., 1994, ApJ, 429, L73

Stanek K.Z., Udalski A., Szymański M., Kałużny J., Kubiak M., Mateo M., Krzemiński W., 1997, ApJ, 477, 163

Sumi T., 2004, MNRAS, 349, 193

Sumi T. et al., 2003, ApJ, 591, 204

Sumi T. et al., 2006, ApJ, 636, 240

Thomas C.L. et al., 2005, ApJ, 631, 906

Tisserand P. et al., 2006, preprint astro-ph/0607207

Udalski A., Szymański M., Kałużny J., Kubiak M., Mateo M., 1992, Acta Astron., 42, 253

Udalski A., Szymański M., Kałużny J., Kubiak M., Krzemiński W., Mateo M., Preston G.W., Paczyński B., 1993, Acta Astron., 43, 289

Udalski A. et al., 1994a, Acta Astron., 44, 165

Udalski A., Szymański M., Mao S., Di Stefano R., Kałużny J., Kubiak M., Mateo M., Krzemiński W., 1994b, ApJ, 436, L103

Udalski A., Żebruń K., Szymański M., Kubiak M., Pietrzyński G., Soszyński I., Woźniak P., 2000, Acta Astron., 50, 1

Udalski A. et al., 2002, Acta Astron., 52, 217

Uglesich R.R., Crotts A.P.S., Baltz E.A., De Jong J., Boyle R.P., Corbally C.J., 2004, ApJ, 612, 877

Walker M.A., 1995, ApJ, 453, 37

Walsh D., Carswell R.F., Weymann R.J., 1979, Nat, 279, 381

Wambsganss J., 1998, Living Rev. in Relativity, 1, 12

Wambsganss J., 2004, in Beaulieu J.-P., Lecavelier des Etangs A., Terquem C., eds, ASP Conf. Ser. 321, Extrasolar Planets: Today and Tomorrow, Astron. Soc. Pac., San Francisco, p. 47

Witt H.J., 1995, ApJ, 449, 42

Witt H.J., Mao S., 1994, ApJ, 430, 505

Wolszczan A., Frail D.A., 1992, Nat, 355, 145

Woźniak P.R., Udalski A., Szymański M., Kubiak M., Pietrzyński G., Soszyński I., Żebruń K., 2001, Acta Astron., 51, 175

Wu X.-P., 1996, Fundamentals of Cosmic Physics, 17, 1

Wyrzykowski Ł., Udalski A., Mao S., Kubiak M., Szymański M.K., Pietrzyński G., Soszyński I., Szewczyk O., 2006, Acta Astron., 56, 145

Zel'dovich, Y.B., 1964, Sov. Astron., 8, 13

Zhao H., Evans N.W., 2000, ApJ, 545, L35

Zhao H., Mao S., 1996, MNRAS, 283, 1197

Zhao H., Spergel D.N., Rich R.M., 1995, ApJ, 440, L13

Zhao H., Rich R.M., Spergel D.N., 1996, MNRAS, 282, 175

Zwicky F., 1937a, Phys. Rev. Lett., 51, 290

Zwicky F., 1937b, Phys. Rev. Lett., 51, 679

Chapter 2

Galactic microlensing and lens detection

In this chapter, microlensing calculations are presented for a new Galactic model. Maps and distributions of optical depth and event timescale are predicted, and compared with the latest observational measurements. Expressions are derived for the asymptotic behaviour of the timescale distribution, in both the long and short tails, in terms of the lens mass. Various event rate distributions are predicted, and new estimates are calculated of the fraction of luminous lenses that should be detected with event follow-up observations, under different selection criteria. Parts of the work in this chapter appear in Wood & Mao (2005).

2.1 Introduction

As discussed in chapter 1, one of the main aims of all microlensing observations is to accurately measure the optical depth, τ – the probability of seeing a microlensing event at any given instant – which can provide much information concerning the structure and mass distribution of the Galaxy and its halo. The composition of this mass, and the Galactic dynamics, can also be probed by measuring the distribution of event timescales.

Since the first estimates of τ by Paczyński (1991) and Griest (1991), predictions based on increasingly refined models have consistently and significantly disagreed with measurements based on increasingly large sets of observational data. However, there are now signs of convergence. Han & Gould (2003, hereafter HG03) used star counts from the *Hubble Space Telescope* (*HST*) to normalise their Galactic model, predicting $\tau = 1.63 \times 10^{-6}$ towards Baade's window (BW), based on lensing of red clump giants (RCGs). They noted reasonable agreement with two recent measurements towards the bulge, also based on RCGs, of $\tau = 2.0\,(2.13) \pm 0.4 \times 10^{-6}$ and $\tau = 0.94\,(1.08) \pm 0.30 \times 10^{-6}$, from the MACHO (Popowski et al. 2001) and EROS (Afonso et al. 2003) collaborations, respectively. The numbers in parentheses are from table 2 of Afonso et al. (2003), who enabled a better comparison between all bulge optical depth measurements to be made by adjusting the values for their offset from BW. Now from 7 yrs of MACHO survey data, Popowski et al. (2005) report $\tau = 2.17^{+0.47}_{-0.38} \times 10^{-6}$ at $(l, b) = (1.50°, -2.68°)$, which is in excellent agreement with recent theoretical predictions, including the Han & Gould result. From the OGLE-II survey Sumi et al. (2006) find $\tau = 2.55^{+0.57}_{-0.46} \times 10^{-6}$ at $(l, b) = (1.16°, -2.75°)$, which is also consistent with the recent MACHO survey value. The latest measurement comes from EROS-2 (Hamadache et al. 2006): they give $\tau = (1.62 \pm 0.23) \exp[-a(|b| - 3 \text{ deg})] \times 10^{-6}$, where $a = (0.43 \pm 0.16 \text{ deg}^{-1})$, in the latitude range $1.4° < |b| < 7.0°$. This agrees well with EROS's previous values, and with the recent MACHO and OGLE-II measurements.

In this chapter, Monte Carlo simulations of the Galaxy are generated based on HG03. §2.2 and §2.3 describe the model and theory, and §2.4 presents the results and discussion. In §2.4.1 the HG03 $\tau_{\rm BW}$ is reproduced, and then predicted optical depths are compared with the recent MACHO, OGLE and EROS measurements in various directions. §2.4.2 presents maps of optical depth and average event timescale. These maps can be compared with observations in any direction. In

§2.4.3 the event rate is predicted as a function of timescale and compared with the distributions observed by OGLE and EROS. In §2.4.4, it is shown how at both long and short times the timescale distribution is directly related to the lens mass function. In light of the observations by Kramer et al. (2006), §2.4.5 examines the potential of a population of slow-moving neutron stars to explain the observed excess of long events. In §2.4.6 estimates are made of the fraction of luminous lenses that could be detected by follow-up observations with space-based telescopes, and in §2.4.7 the expected event rate as a function of Einstein radius is given, showing similar asymptotic behaviour to that with timescale. A summary and conclusions follow in §2.5.

2.2 The model

2.2.1 Bulge and disc mass models

Dwek et al. (1995) compared various hypothetical mass density models of the bulge with the infrared light density profile seen by the *Cosmic Background Explorer* (*COBE*) satellite. Here, the G2 (barred) model from their table 1, with $R_{\max} = 5$ kpc, is used. The bar is inclined by $\theta_{\rm bar} = 13.4°$ to the Galactic Centre line of sight (LOS), and the distance to the Galactic centre is set at 8 kpc. Dwek et al. used 8.5 kpc, so their model parameters are adjusted accordingly. The model is then normalised by the *HST* star counts of Holtzman et al. (1998), as described in §2.2.3. This independent constraint can be used to normalise any bulge model.

For the disc, the local disc density model of Zheng et al. (2001) is used, as extended to the whole disc by HG03. As the disc model is relatively secure (HG03), it will contribute only small uncertainties to predictions of the optical depth, so it is not renormalised as for the bulge model.

2.2.2 Source and lens populations

The optical depth reported by Popowski et al. (2005) is based on lensing of RCGs in the bulge, and HG03 assume only bulge RCG sources in their model. Sumi et al. (2006) observed lensing of red giants and red supergiants as well as RCGs. These different types of stars are assumed to follow the same bar density distribution and are bright enough to be seen throughout the bar, which corresponds to the

case with $\gamma = 0$ in equation (2.7), §2.2.5.

The lens mass function is generated as in HG03. Their unnormalised bulge mass function assumes initial star formation according to

$$\frac{\mathrm{d}N}{\mathrm{d}M} = k \left(\frac{M}{M_{\mathrm{brk}}} \right)^{\alpha}, \tag{2.1}$$

where $M_{\mathrm{brk}} = 0.7$ M$_\odot$, $\alpha = -2.0$ for $M > M_{\mathrm{brk}}$, and $\alpha = -1.3$ for $M \leq M_{\mathrm{brk}}$, consistent with observations by Zoccali et al. (2000). However, HG03 extended this beyond the latter's lower limit of $M \sim 0.15$ M$_\odot$ to a brown dwarf cut-off of $M \sim 0.03$ M$_\odot$. The model assumes objects with masses 0.03–0.08 M$_\odot$ and 0.08–1 M$_\odot$ become brown dwarfs (BD) and main-sequence stars (MS), respectively, 1–8 M$_\odot$ stars evolve into 0.6 M$_\odot$ white dwarfs (WD), 8–40 M$_\odot$ stars become 1.35 M$_\odot$ neutron stars (NS), and anything more massive forms a 5 M$_\odot$ black hole (BH). The resulting mass fractions are

$$\mathrm{BD} : \mathrm{MS} : \mathrm{WD} : \mathrm{NS} : \mathrm{BH} = 7 : 62 : 22 : 6 : 3. \tag{2.2}$$

Note that the mass is dominated by MS stars, which also provide the normalisation constraint on the bulge model (see §2.2.3).

2.2.3 Normalisation method

The bulge is randomly populated according to the mass function described in §2.2.2. MS stars are assigned magnitudes from the mass-M_V relation of Cox (1999), with adjustment for the star's distance. All other lenses are taken to be dark. The same mass function and luminosity relation are also used for the disc. Strictly speaking they should be estimated independently, but any uncertainties are small compared to others involved, as the disc contributes only ∼20% of all the model stars.

Extinction reddening is applied to each star using equation (2.3), as used by HG03 (Han & Gould, private communication). It assumes a total extinction along the LOS to BW (i.e. 8 kpc) of $A_V = 1.28$ (Holtzman et al. 1998), and a dust scale height of 120 pc:

$$A_V(x) = -2.5 \times \log_{10} \left\{ \exp \left[-6.76 \times 10^{-4} \int_0^x \exp \left(-\frac{|z|}{h_z} \right) dx \right] \right\}, \tag{2.3}$$

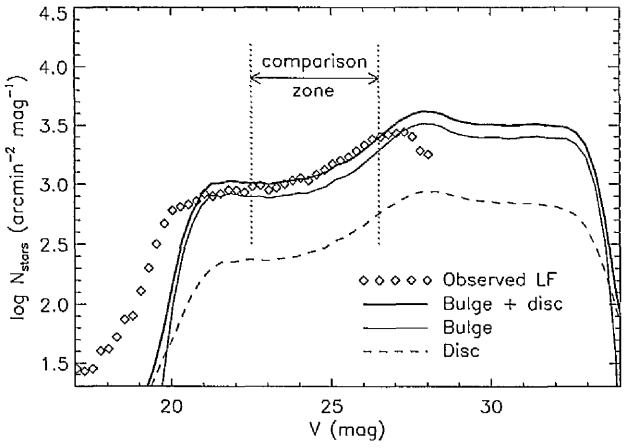

Figure 2.1: Star counts towards BW. The disc model is fixed, while the bulge model is normalised so that the total counts match the observed luminosity function (LF) of Holtzman et al. (1998) in the range $22.5 < V < 26.5$.

where x is the star's distance, $z = x\sin(b)$ is the height above the Galactic plane and h_z is the scale height.

Fig. 2.1 shows how the bulge star counts are then normalised, so that the total counts from the bulge and disc match the Holtzman et al. (1998) *HST* V-band star counts in BW, in the range $22.5 < V < 26.5$. The observational data are incomplete at fainter magnitudes, and at brighter magnitudes the mass-luminosity relation does not account for evolution off the MS, thus slightly overpredicting the counts. (At much greater magnitudes the absence of giants from the model causes a large underprediction). The disc counts are not adjusted as the disc is already well modelled by Zheng et al. (2001).

2.2.4 Kinematic model

To calculate the event rate, the velocities of the lenses, sources and observer must also be specified. The observer velocity $v_{\rm O}$ is assumed to follow the Galactic rotation, adjusted for the Sun's peculiar motion, so the two velocity components in l and b are given by

$$v_{{\rm O},l} = v_{\rm O,rot} = 220 + 5.2 \ {\rm kms}^{-1}, \qquad v_{{\rm O},b} = 0 + 7.2. \tag{2.4}$$

The lens and source velocities in the l and b directions are given by

$$v_l = v_{\rm rot} + v_{{\rm rand},l}, \qquad v_b = v_{{\rm rand},b}, \tag{2.5}$$

where $v_{\rm rot}$, the longitudinal component of the rotation velocity, and $v_{\rm rand}$, the random velocity, are from Han & Gould (1995): for the disc $v_{\rm rot} = 220$ kms^{-1}, and for the bar $v_{\rm rot}$ is given by projecting $v_{\rm max} = 100$ kms^{-1}, the maximum rotational velocity, across the LOS according to

$$\begin{aligned} v_{\rm rot} &= v_{\rm max}\left(\frac{x}{1\ {\rm kpc}}\right) \qquad (R < 1\ {\rm kpc},\ {\rm solid\ body\ rotation}), \\ v_{\rm rot} &= v_{\rm max}\left(\frac{x}{R}\right) \qquad (R \geq 1\ {\rm kpc},\ {\rm flat\ rotation}), \end{aligned} \tag{2.6}$$

where $R = (x^2 + y^2)^{1/2}$, and the coordinates (x, y, z) have their origin at the Galactic centre, with the x and z axes pointing towards the Earth and the north Galactic pole, respectively. The random velocity components $v_{{\rm rand},l}$ and $v_{{\rm rand},b}$ are assumed to have Gaussian distributions, with dispersions taken from Han & Gould (1995): for the disc, $\sigma_{l,b} = (30, 20)$ kms^{-1}; for the bar, they calculated $\sigma_{x,y,z} = (110, 82.5, 66.3)$ kms^{-1} from the tensor virial theorem (see also Kuijken & Rich 2002; Sumi, Eyer & Woźniak 2003). This was done for $\theta_{\rm bar} = 20.0°$, with a normalisation to the observed mean LOS dispersion of $\sim$110 kms^{-1}. Adjusting for $\theta_{\rm bar} = 13.4°$ yields $\sigma_{x,y,z} = (110, 78.4, 65.1)$ kms^{-1}. These values should be altered slightly, as the calculation by Han & Gould (1995) contained a mistake as pointed out by Blum (1995), and did not of course include HG03's normalisation by star counts. This may have a small effect on the results (see chapter 4), but it is reassuring that the results based on such a simple kinematic model appear to agree with the data quite well (see §2.4).

2.2.5 Optical depth and event rate

τ in any given direction is an average over the optical depths of all the source stars in that direction. The optical depth to a particular star is defined as the probability that it is within the Einstein radius of any foreground lenses. Hence more distant stars, although fainter and less likely to be detected, have higher optical depths (e.g. Stanek 1995). HG03 accounted for this with the term γ in

the calculation of expected optical depth:

$$\langle \tau \rangle_\gamma = \frac{4\pi G}{c^2} \frac{\int_0^\infty \mathrm{d}D_\mathrm{s} D_\mathrm{s}^{2-\gamma} \rho(D_\mathrm{s}) \int_0^{D_\mathrm{s}} \mathrm{d}D_\mathrm{d} \rho(D_\mathrm{d}) D_\mathrm{d}(D_\mathrm{s} - D_\mathrm{d})/D_\mathrm{s}}{\int_0^\infty \mathrm{d}D_\mathrm{s} D_\mathrm{s}^{2-\gamma} \rho(D_\mathrm{s})}, \tag{2.7}$$

where D_s and D_d are the distances to the source and deflector (lens), respectively, and $\rho(D_\mathrm{s})$ and $\rho(D_\mathrm{d})$ are the source number density and lens mass density. RCGs and other bright stars in the bulge can be identified independently of their distance, so $\gamma = 0$. Equation (2.7) was originally presented (in a slightly different form) by Kiraga & Paczyński (1994), who also derived an expression for the lensing event rate Γ, for a population of lenses with identical masses. That expression is given here in terms of γ, with variable lens masses accounted for by bringing the term $M^{-1/2}$ inside the integral:

$$\begin{aligned} \Gamma &= \frac{4G^{1/2}}{c} \int_0^\infty \mathrm{d}D_\mathrm{s} D_\mathrm{s}^{2-\gamma} \rho(D_\mathrm{s}) \\ &\quad \times \frac{\int_0^{D_\mathrm{s}} \mathrm{d}D_\mathrm{d} \rho(D_\mathrm{d}) v [D_\mathrm{d}(D_\mathrm{s} - D_\mathrm{d})/M D_\mathrm{s}]^{1/2}}{\int_0^\infty \mathrm{d}D_\mathrm{s} D_\mathrm{s}^{2-\gamma} \rho(D_\mathrm{s})}, \end{aligned} \tag{2.8}$$

where v is the lens-source relative transverse velocity,

$$v = ({v_l}^2 + {v_b}^2)^{1/2}, \tag{2.9}$$

and its components in the Galactic l and b coordinates, v_l and v_b, are related to the observer, lens and source velocities by

$$v_{l,b} = \left[(v_\mathrm{D} - v_\mathrm{O}) + (v_\mathrm{O} - v_\mathrm{S}) \frac{D_\mathrm{d}}{D_\mathrm{s}} \right]_{l,b}, \tag{2.10}$$

where v_D and v_S are the deflector (lens) and source transverse velocities; their components in the l and b directions are given by equation (2.5).

The timescale of an event t_E is defined as the time taken for a source to cross the Einstein radius of the lens (Paczyński 1996):

$$t_\mathrm{E} = \frac{r_\mathrm{E}}{v} \qquad r_\mathrm{E} = \left[\frac{4GM}{c^2} \frac{D_\mathrm{d}(D_\mathrm{s} - D_\mathrm{d})}{D_\mathrm{s}} \right]^{1/2}. \tag{2.11}$$

2.3 Lens detection

2.3.1 Threshold magnitude and proper motion

62% of all the model lenses are luminous (see §2.2.2). However, during a microlensing event stellar lenses generally cannot be resolved from their source, and may only be independently observed some time afterwards. Detecting these lenses would enable accurate measurement of the lens-source relative proper motion, which has important applications as discussed in §1.4.3. (Such an event is analysed in chapter 5).

The fraction of detectable model lenses is calculated via the method of Han & Chang (2003). They defined the condition for a lens and source to be separately resolved as $\mu\Delta t \geq \theta_{\rm th}(\Delta m)$, where a lens with relative proper motion μ will, at a time Δt after lensing, be separated from the source by an angle $\geq$ a threshold angle $\theta_{\rm th}$. Hence in a follow-up observation of the event at this time, the lens would be resolved.

Since $\theta_{\rm th}$ depends on the lens-source apparent flux ratio, it is calculated as a function of the difference in apparent magnitude, $\Delta m = m_L - m_S$. For this calculation, the point spread function (PSF) of each stellar image is modelled as a Gaussian, with standard deviation σ – the resolving power of the observing instrument is $\theta_{\rm PSF} = 2\sigma$. Two real cameras are considered: the High Resolution Channel of the Advanced Camera for Surveys on the *HST*, with $\theta_{\rm PSF} \sim 0.064$ arcsec; and the Near Infrared Camera of the *James Webb Space Telescope* (*JWST*), capable of $\theta_{\rm PSF} \sim 0.05$ arcsec.

The two Gaussians are normalised such that the area under each is proportional to the flux of each star, thus forming the combined image. If the derivative of this combined image changes sign more than once between the centres of the individual images, the stars are deemed to be resolved – see Fig. 2.2. $\theta_{\rm th}$ is then simply the minimum separation at which this occurs.

Fig. 2.3 shows $\theta_{\rm th}$ as a function of Δm, for the two PSFs considered. From this distribution, the fraction of resolvable lenses can be calculated as a function of elapsed time after lensing. Of course a resolvable lens must be sufficiently bright to actually be detected. A threshold magnitude for the lenses is set at $V = 26.4$ (as for the *HST*[1]).

[1]This is the approximate magnitude limit for the observations reported by Kozłowski et al. (2006, Kozłowski, private communication), which are considered in chapters 4 and 5.

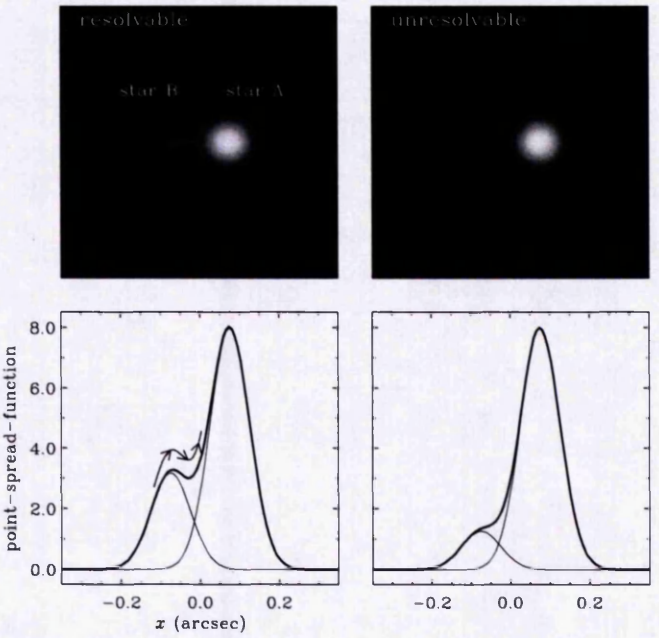

Figure 2.2: Condition for resolving two stars (Han & Chang 2003, fig. 2). Top panels: Two examples of the combined image of the lens and source. Bottom panels: The PSFs of the lens and source (thin lines) are modelled as two Gaussians, with areas proportional to the fluxes of the two stars, and standard deviation σ, where the resolution of the observing instrument is $\theta_{\rm PSF} = 2\sigma$. In both cases, $\sigma = 0.05$ arcsec, and the stars are separated by 0.15 arcsec, but the magnitude differences are different: $\Delta m = 1.0$ (left) and 2.0 (right). The stars are deemed to be resolved if the derivative of the combined image (bold line) changes sign more than once between the two peaks. Hence the two stars on the left are resolved, but those on the right are not.

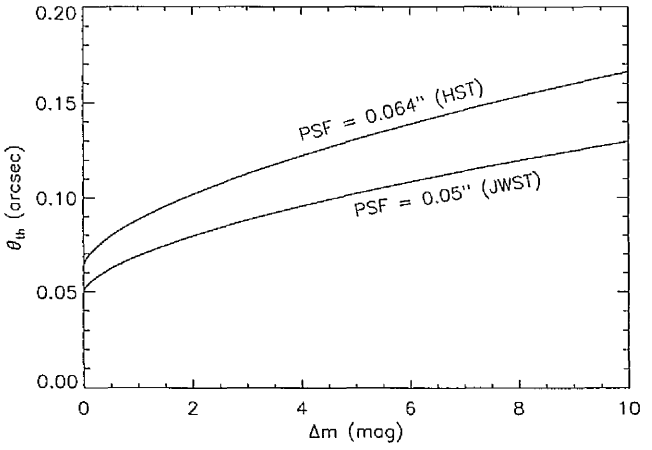

Figure 2.3: The threshold angular separation $\theta_{\rm th}$ for resolving two stars, as a function of their difference in apparent magnitude Δm. Plots are shown for $\theta_{\rm PSF}$ = 0.064 and 0.05 arcsec, corresponding to the *HST* and *JWST*, respectively.

This is of course only a simple one-dimensional criterion, but it should enable an approximate estimation of the fraction of potentially detectable lenses. However, to make the calculation more realistic, two further criteria are considered that account for limitations of real observations, regarding total amplification (§2.3.2) and signal-to-noise ratio (§2.3.3).

2.3.2 Total amplification

Microlensing surveys use various algorithms and data cuts to distinguish lensing events from other phenomena such as variable stars. Since the cross-section of a lensing event is defined as the Einstein circle, and the amplification A of a source at the Einstein radius is 1.34 (see §1.3.1), then in principle $A \geq 1.34$ for any lensing event. However, where the lens is luminous, blending means the total amplification actually seen is A', a function of both the lens flux f_{lens}, and the source flux f_{source}:

$$A' = \frac{f_{lens} + A f_{source}}{f_{lens} + f_{source}}. \tag{2.12}$$

Depending on A, the lens flux need only be a small fraction of the source flux for A' to be < 1.34. Hence if an observer requires $A \geq 1.34$, a real event may be missed. The effect of declaring events undetectable where $A' < 1.34$ is investigated. (In practice a lower amplification threshold may be set, and this method can, of

course, be used for any preferred value).

2.3.3 Signal-to-noise condition

Requiring $A' \geq 1.34$ as above represents one practical limit on lens detection. Another is the signal-to-noise (S/N) ratio. The Poisson uncertainty in a measurement of apparent brightness is simply the square root of the number of photons observed. To calculate the lens and source photon counts, N_{lens} and N_{source}, all stars are assumed to emit at a wavelength of 550 nm, in the middle of the V band. An event is then deemed detectable if, at peak magnification, the increase in source flux above its baseline is greater than the uncertainty in the total flux from both source and lens:

$$(A-1)N_{source} \geq \kappa\sqrt{N_{lens} + AN_{source}}, \tag{2.13}$$

where κ is the desired S/N ratio. Here $\kappa = 3$ is chosen.

2.4 Results and discussion

2.4.1 Comparison with observed optical depths

HG03 calculated $\tau = (0.98, 0.65, 1.63) \times 10^{-6}$ towards BW for bulge, disc and all lenses, respectively. The equivalent values predicted here are (1.06, 0.65, 1.71) $\times 10^{-6}$. HG03 noted that the value of γ made little difference to τ for disc lenses, but for bulge lenses it became 0.86×10^{-6} when $\gamma = 1$. $\tau = 0.92 \times 10^{-6}$ is predicted in this case. The results for bulge lenses differ by 7–8% from that of HG03 due to a slight difference in implementation of the bulge model normalisation. Allowing MS disc lenses to also act as sources themselves is found to make a negligible difference to the total value of τ.

The MACHO measurement (Popowski et al. 2005) of $\tau = 2.17^{+0.47}_{-0.38} \times 10^{-6}$ at $(l, b) = (1.50°, -2.68°)$ was obtained from a subsample of nine of their 83 analysed fields, the central Galactic region (CGR), which covers 4.5 deg^2 and contains 42 of the 62 RCG microlensing events seen. The coordinates $(1.50°, -2.68°)$ are a weighted average position of these fields; the unweighted average is $(l, b) = (1.55°, -2.82°)$. Optical depths were also given for a region CGR+3 that contains 3 additional fields, and for all 83 fields. In Table 2.1 the expected values are

compared with each of these results, and with τ reported for each of the individual CGR fields.

The OGLE measurement (Sumi et al. 2006) of $\tau = 2.55^{+0.57}_{-0.46} \times 10^{-6}$ at $(l, b) = (1.16°, -2.75°)$ made use of all their 32 RCG events, in 20 of their 49 fields, where $(l, b) = (1.16°, -2.75°)$ is the weighted average field position. τ was also given for each field. All these results are compared with the predictions in Table 2.2.

Note that any significant disagreement occurs only in individual fields, and that in only 1 of the 6 fields (MACHO and OGLE) with > 4 events (OGLE no. 30) does an expected value lie far outside the stated 1σ uncertainty of the corresponding measured value.

The average coordinates given by MACHO (for the CGR) and OGLE apply to subsets of their fields that span only a few degrees in l and b. Hamadache et al. (2006) do not state any mean EROS coordinates. They used all 66 of their survey fields, covering a much larger area of sky, so such an average would be meaningless. Hence they focus on the optical depth trends with l and b – which are considered shortly – rather than a single average τ. They also do not give τ measurements for each individual EROS field, so no field-by-field comparison with the model is made here.

Table 2.3 shows the percentage contributions to the total expected optical depth and the event rate from the different types of lenses. Note that, as expected, the τ fractions are equal to the mass fractions given in §2.2.2. The disc lenses contribute 37% of the optical depth and a slightly smaller fraction, 31%, of the event rate. 62% of all events have luminous (MS) lenses, the other 38% are dark (BD, WD, NS and BH). The NSs and BHs contribute 9% of the optical depth but only 4% of the event rate. This is because the events caused by stellar remnants on average have longer timescales, and thus they occur less frequently.

In their figs. 12 and 13, respectively, Sumi et al. (2006) and Popowski et al. (2005) plot average optical depths in latitude and longitude strips. Similar predicted plots are given in Fig. 2.4, with the OGLE and MACHO data points shown. τ is averaged over the ranges $-5.5° \leq l \leq 5.5°$ and $-5.5° \leq b \leq 0.0°$ for the latitude and longitude strips, respectively, in accordance with Popowski et al. (2005). These ranges also include all the events seen by Sumi et al. (2006). (Tightening these ranges to just bound the OGLE fields makes only a small difference compared to the uncertainties in the data points). In both sets of strips the model is in good agreement with both sets of data. The single data

Region/field	N_{events}*	(l, b) (°)	τ_{MACHO} $(\times 10^{-6})$	τ_{model} $(\times 10^{-6})$
CGR	42	(1.50, -2.68)†	$2.17^{+0.47}_{-0.38}$	2.43
CGR	42	(1.55, -2.82)‡	–	2.33
CGR+3	53	(1.84, -2.73)	$2.37^{+0.47}_{-0.39}$	2.34
All 83 fields	62	(3.18, -4.30)	$1.21^{+0.21}_{-0.21}$	1.32
108	6	(2.30, -2.65)	2.04 ± 0.92	2.31
109	2	(2.45, -3.20)	0.58 ± 0.41	1.96
113	3	(1.63, -2.78)	0.55 ± 0.35	2.34
114	3	(1.81, -3.50)	1.19 ± 0.74	1.87
118	7	(0.83, -3.07)	2.85 ± 1.35	2.25
119	0	(1.07, -3.83)	–	1.74
401	7	(2.02, -1.93)	5.13 ± 2.16	2.85
402	10	(1.27, -2.09)	3.95 ± 1.50	2.89
403	4	(0.55, -2.32)	1.16 ± 0.66	2.83

Table 2.1: Comparison of model and MACHO optical depths for the central Galactic region (CGR) and individual fields. *Number of events seen by MACHO. †Weighted average (l, b). ‡Unweighted average (l, b).

point at negative l is based on only one microlensing event, so its deviation from the predicted curve is of low statistical significance.

Hamadache et al. (2006) also produce similar plots in their fig. 15, but for quite different ranges of l and b. Therefore the predictions are compared with the EROS results in a separate plot, Fig. 2.5. For the latitude strips, Hamadache et al. (2006) plot τ as a function of $|b|$ (rather than b), since their survey included northern fields. (Note that they see no significant difference between the northern and southern fields, as expected, and that the model is symmetric about $b = 0$). τ is averaged over a larger range in l than above, to include all the EROS events: $-7.0° \leq l \leq 10.0°$. For the longitude strips, Hamadache et al. (2006) only average over the range $1.4° \leq |b| \leq 3.0°$. Therefore the same is done here. Again, in both sets of strips there is good agreement between the model and observations.

Region/field	N_{events}*	(l, b) (°)	τ_{OGLE} $(\times 10^{-6})$	τ_{model} $(\times 10^{-6})$
All 20 fields	32	(1.16, -2.75)†	$2.55^{+0.57}_{-0.46}$	2.43
1	0	(1.08, -3.62)	–	1.87
2	1	(2.23, -3.46)	2.48 ± 2.48	1.85
3	4	(0.11, -1.93)	4.29 ± 2.23	3.20
4	5	(0.43, -2.01)	3.15 ± 1.49	3.09
20	1	(1.68, -2.47)	1.24 ± 1.24	2.54
21	0	(1.80, -2.66)	–	2.39
22	1	(-0.26, -2.95)	0.85 ± 0.85	2.42
23	0	(-0.50, -3.36)	–	2.13
30	6	(1.94, -2.84)	9.54 ± 4.18	2.26
31	1	(2.23, -2.94)	2.26 ± 2.26	2.15
32	1	(2.34, -3.14)	0.94 ± 0.94	2.02
33	2	(2.35, -3.66)	10.42 ± 7.93	1.73
34	2	(1.35, -2.40)	4.09 ± 2.89	2.65
35	2	(3.05, -3.00)	3.21 ± 2.35	1.98
36	0	(3.16, -3.20)	–	1.85
37	2	(0.00, -1.74)	2.21 ± 1.77	3.39
38	2	(0.97, -3.42)	2.88 ± 2.25	2.01
39	3	(0.53, -2.21)	1.62 ± 0.97	2.92
45	0	(0.98, -3.94)	–	1.68
46	0	(1.09, -4.14)	–	1.56

Table 2.2: Comparison of model and OGLE optical depths. *Number of events seen by OGLE. †Weighted average (l, b).

	Location/type of lens						
	Bar	Disc	BD	MS	WD	NS	BH
Optical depth	63	37	7	62	22	6	3
Event rate	69	31	17	62	17	3	1

Table 2.3: Percentage contributions, to the total predicted optical depth and event rate, from different types of lens.

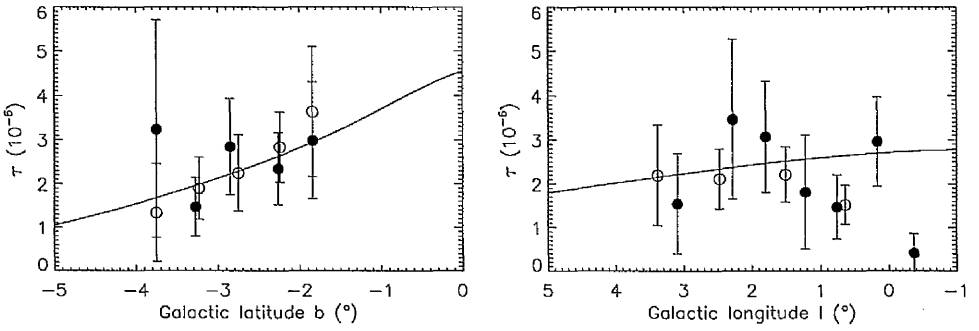

Figure 2.4: Average optical depth in latitude (left panel) and longitude (right panel) strips, for $-5.5° \leq l \leq 5.5°$ and $-5.5° \leq b \leq 0.0°$, respectively. The solid line shows the model prediction, while the open and solid circles are data points from MACHO (Popowski et al. 2005, fig. 13) and OGLE (Sumi et al. 2006, fig. 12), respectively.

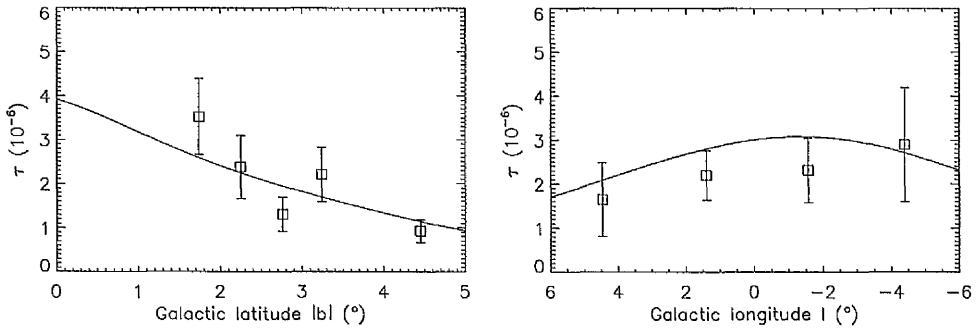

Figure 2.5: Average optical depth in latitude (left panel) and longitude (right panel) strips, for $-7.0° \leq l \leq 10.0°$ and $1.4° \leq |b| \leq 3.0°$, respectively. The solid line shows the model prediction, while the data points are from EROS (Hamadache et al. 2006, fig. 15).

2.4.2 Maps of optical depth and average event timescale

Figs. 2.6 and 2.7 are maps of expected optical depth and average event timescale. We can clearly see higher optical depths and longer timescales at negative galactic longitude. This is due to the inclination of the bar to the LOS. At positive longitude the bar is closer to us, and the LOS cuts through the bar at a steeper angle. Hence there are fewer potential lenses, in either the disc or the bar, between us and any bar source, and so τ is smaller. Also, objects rotating around the Galactic centre have a smaller component of their velocity along the LOS, so average transverse velocities will be greater, and average timescales shorter. At negative longitude, the LOS passes through more of the disc and cuts the bar at a shallower angle. Hence we see higher optical depths and smaller transverse velocities, and thus longer average timescales.

This longitudinal asymmetry is also clearly a function of latitude. In the optical depth map, the degree of asymmetry decreases with $|b|$, as would be expected since τ is proportional to mass. In the average event timescale map, however, the asymmetry is much greater at large $|b|$. As above, this is due to the inclination of the bar. Consider two lines of sight at equal and opposite l, and $b = 0$. As both lines of sight move towards larger $|b|$, they obviously pass through less of the disc, and less of the bar. As the disc is symmetric, both lines of sight pass through equal amounts of disc. However, the inclination of the bar means that the LOS at negative l will pass through less and less of the bar than the one at positive l: since the bar is further away at negative l, a LOS with large $|b|$ will be further away from the plane as it passes through the bar. Hence the relative contributions to the total event rate from bulge and disc lenses will become increasingly assymetric at large $|b|$. Therefore it is not surprising that the average event timescales should also become increasingly assymetric.

Figs. 2.6 and 2.7 also show the MACHO fields and BW. For comparison, the maps are replotted in Figs. 2.8 and 2.9 showing the OGLE fields, and in Figs. 2.10 and 2.11 showing the EROS fields. (Separate figures are given for clarity, as the MACHO, OGLE and EROS fields all overlap).

These maps are now compared with others. Evans & Belokurov (2002) produced red clump optical depth maps for three Galactic models, but while two of these appear similar to that in Fig. 2.6, they do not agree. One of those models was also used to make a timescale map, which is quite different to that in Fig. 2.7. This is not surprising since, as well as using a different mass model, their mass

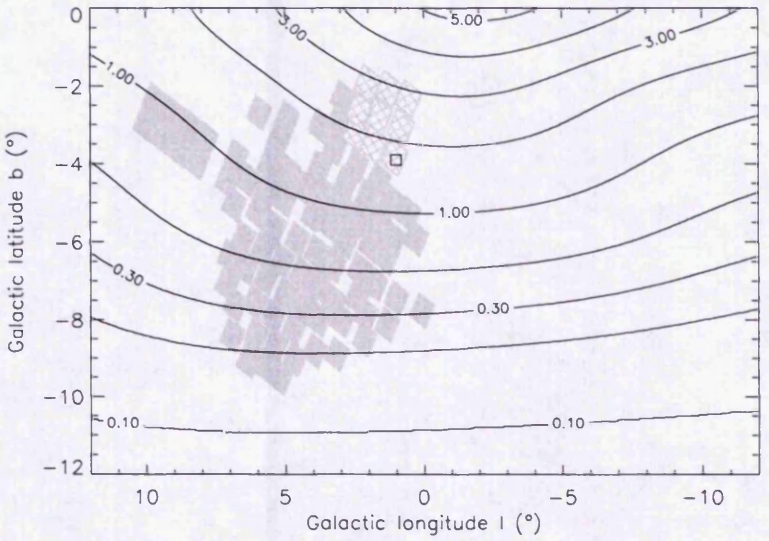

Figure 2.6: Map of the expected optical depth. The MACHO fields are shown by the grey boxes – the crosshatch pattern denotes the CGR subset listed in Table 2.1. The small square indicates BW. Contour levels are at $(0.1, 0.2, 0.3, 0.5, 1, 2, 3, 4, 5) \times 10^{-6}$.

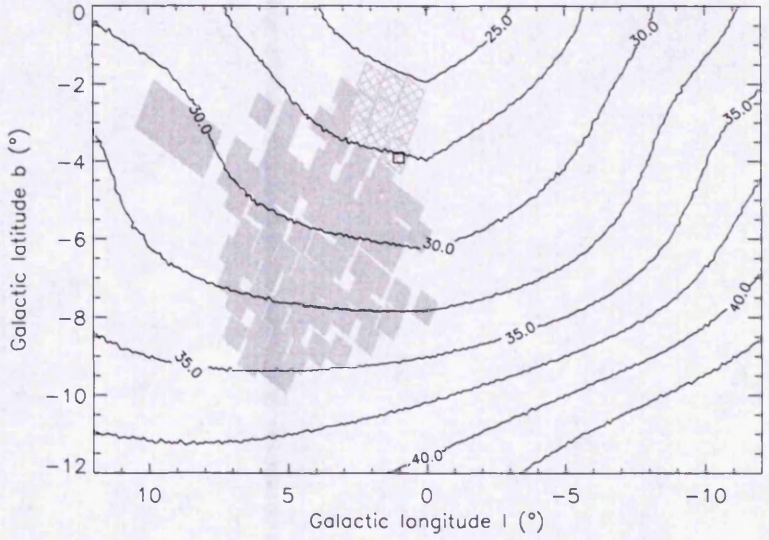

Figure 2.7: Map of the expected average event timescale. The MACHO fields and BW are indicated as in Fig. 2.6. Contour levels are at 22.5, 25, 27.5, 30, 32.5, 35, 37.5, 40 and 42.5 days.

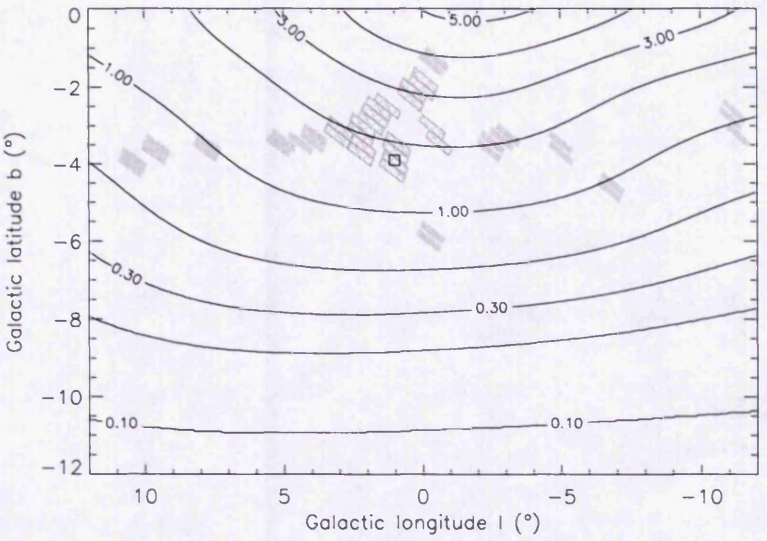

Figure 2.8: Map of the expected optical depth. Same as Fig. 2.6, but with the OGLE fields shown – the crosshatch pattern denotes the subset listed in Table 2.2.

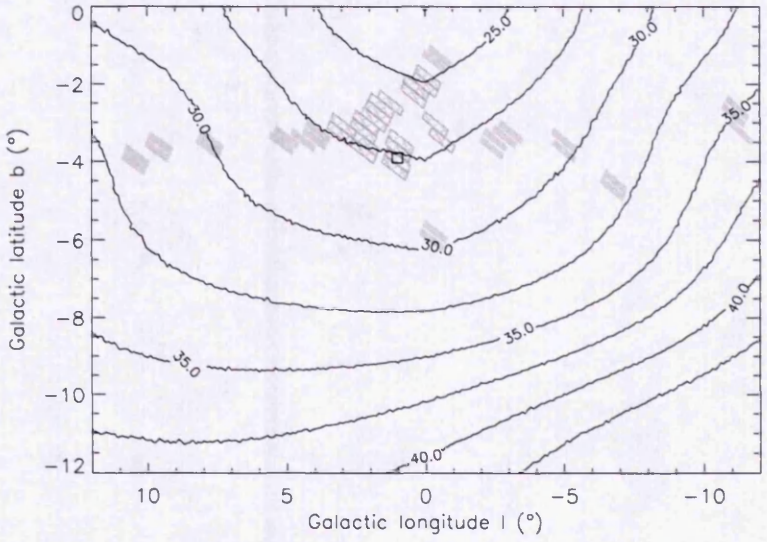

Figure 2.9: Map of the expected average event timescale. Same as Fig. 2.7, but with the OGLE fields shown – the crosshatch pattern denotes the subset listed in Table 2.2.

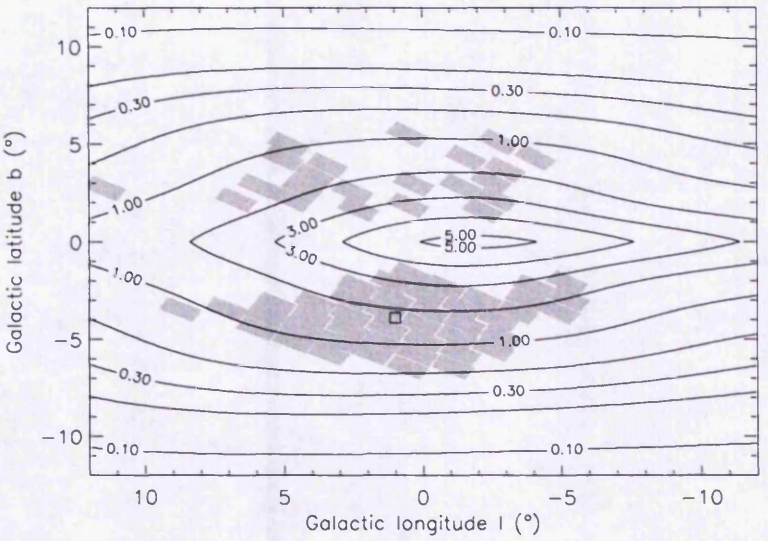

Figure 2.10: Map of the expected optical depth. Same as Fig. 2.6, but with the EROS fields shown.

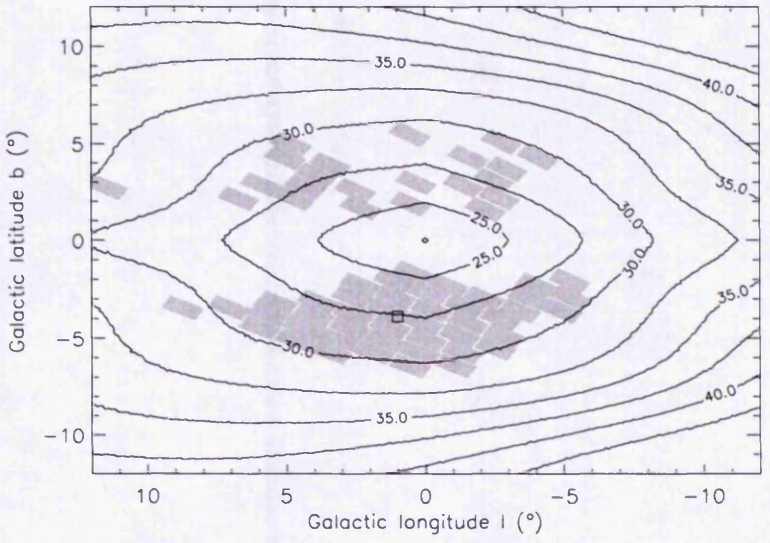

Figure 2.11: Map of the expected average event timescale. Same as Fig. 2.7, but with the EROS fields shown.

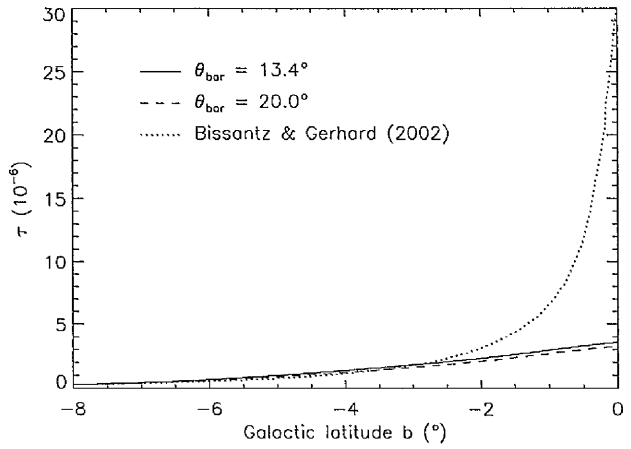

Figure 2.12: τ as a function of b, for $l = 3.9°$. The model slope is almost identical for bar angles of 13.4° and 20°. The profile of Bissantz & Gerhard (2002) diverges from the prediction at $b \approx -3°$, increasing rapidly towards the mid-plane ($b = 0°$).

function, velocities and velocity dispersions were also different to those used here. (In fact, their timescale map has two sets of contours, to show the effects of including and excluding bar streaming. Without streaming, their mean timescales are much shorter than those predicted here, and with it they are greater by a factor $\sim$3 – much longer than here. Such a large variation is puzzling, and one should be cautious about comparing their map too closely to Fig. 2.7).

In their fig. 16, Bissantz & Gerhard (2002) presented an optical depth map for RCG sources, with $\theta_{\rm bar} = 20°$. For $b \lesssim -3°$ it appears quite similar to Fig. 2.6, but moving towards the Galactic centre their τ climbs far more steeply. This is best seen by comparison with their fig. 17, where they plot τ as a function of b, for $l = 3.9°$. This is shown in Fig. 2.12: moving towards $b = 0°$, Bissantz & Gerhard's profile diverges rapidly from that predicted here. It is also clear that changing $\theta_{\rm bar}$ in the model from 13.4° to 20° does not explain this difference. Instead it is probably due to the density in their bulge mass model increasing much faster towards the mid-plane. The observational data for the mid-plane are limited due to heavy extinction, and so mass models are not well constrained in this region. Given the difficulty in obtaining any measurement of τ at small latitude, it is difficult at present to test either profile there.

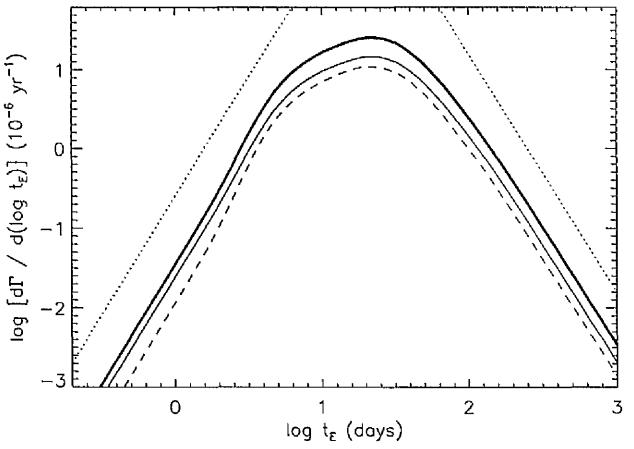

Figure 2.13: Expected microlensing event rate as a function of timescale, along the OGLE LOS, for bar (thin line), disc (dashed line) and all (bold line) lenses. The two dotted lines are asymptotic tails $d\Gamma/d(\log t_E) \propto {t_E}^3$, ${t_E}^{-3}$ for very short and long timescales, respectively.

2.4.3 Timescale distributions

Fig. 2.13 shows the expected event rate as a function of timescale along the OGLE LOS, for bar (thin line), disc (dashed line) and all (bold line) lenses. There is good agreement with the asymptotic power-law tails $d\Gamma/d(\log t_E) \propto {t_E}^3$, ${t_E}^{-3}$ (dotted lines) for very short and long timescales, respectively (Mao & Paczyński 1996). The disc lensing events have an average timescale of 26.4 days, slightly shorter than the bulge lensing events' average of 26.7 days. The average timescale for all events is 26.6 days.

In Fig. 2.14, this timescale distribution (for all lenses) is renormalised and compared with those seen by OGLE (top panel) and EROS (bottom panel), as corrected for detection efficiency (see figs. 14 and 16 in Sumi et al. 2006 and Hamadache et al. 2006, respectively). Of course the EROS distribution includes many events observed several degrees away from the OGLE LOS, but the predicted distribution does not change greatly over the EROS survey region: as already shown by Fig. 2.11, the average t_E varies by only a few days. No comparison is made with the timescale distribution seen by Popowski et al. (2005) – they assumed that the effect of blending on RCG sources is negligible, but Sumi et al. (2006) found ~38% of OGLE-II events with apparent RCG sources were really due to faint stars blended with a bright companion. Fortunately, they also

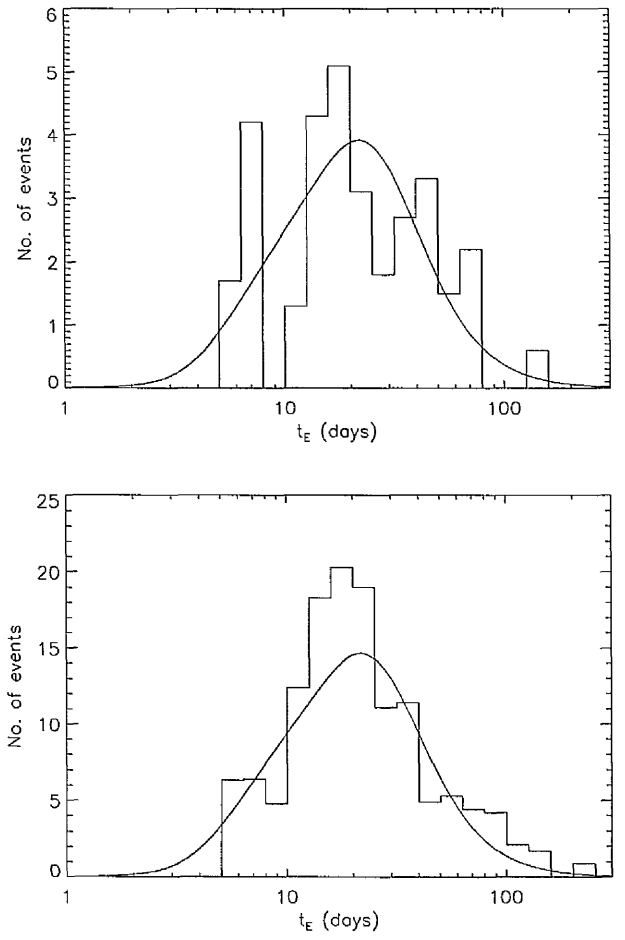

Figure 2.14: Microlensing event rate as a function of timescale. The solid line shows the prediction along the OGLE LOS. The histogram in the (top, bottom) panel shows the (OGLE, EROS) observed distribution, corrected for detection efficiency. In both panels the model distribution is normalised to have the same area as that observed.

showed that blending has little effect on estimates of τ, due to partial cancellation of its different effects – a point also made by Popowski et al. (2005), and by Hamadache et al. (2006) who estimated a 5% uncertainty. However, timescale distributions will be significantly shifted towards shorter events. As a result, the MACHO timescale distribution (not shown) has a significant excess at short timescales compared with the model prediction.

The model timescale distribution shows reasonable agreement with that of OGLE. The Kolmogorov–Smirnov (KS) test shows that the predicted and observed distributions are consistent at a 61% confidence level. The expected average timescale of 26.6 days is in good agreement with OGLE's corrected average of 28.1 ± 4.3 days, and also with EROS's corresponding value of 28.3 ± 2.8 days. The median and quartiles are (19.7, 11.5, 32.3) days, respectively. However there is poorer agreement with the distribution seen by EROS. Although the KS d-statistic is slightly smaller – 0.10 compared with 0.13 – the two distributions are only consistent at a 15% level. This is mainly due to EROS's larger sample size (120 events compared with OGLE's 32), which increases the significance of any differences between the distributions. The most important difference, with both the OGLE and EROS data, is the excess of observed long events. We return to this in §2.4.5.

Both the OGLE and EROS $t_{\rm E}$ distributions still have large uncertainties due to the limited numbers of events. It is apparent that the data have not yet reached the predicted asympototic behaviour at short and long timescales, so a more stringent test on the model is not yet possible.

Bissantz, Debattista & Gerhard (2004, see also Peale 1998) have also modelled the timescale distribution. They reproduced that from MACHO's 99 difference image analysis (DIA) events (Alcock et al. 2000) centred at $(l, b) = (2.68°, -3.35°)$. However, both these distributions are clearly shifted towards short timescales compared with the model prediction here towards the same coordinates – this is not shown, as it is very close to the solid line in Fig. 2.14.[2] Although the DIA method is less prone to the systematics of blending (Sumi et al. 2006), it is still possible that the MACHO DIA timescale distribution is somewhat affected. The most important difference between the model and that of Bissantz et al. is that in order to match the data at short timescales, they

[2]At first glance all three distributions may appear to be similar. However, MACHO plot the crossing time of the Einstein diameter, rather than the radius, in line with their different definition of $t_{\rm E}$.

Timescale	BD	MS	WD	NS	BH
Long	0.53	44	20	12	24
Short	72	27	1.5	0.078	0.0032

Table 2.4: Percentage contributions to the total predicted event rate, at long and short timescales, from the different types of lens.

adopted a Schecter mass function, $n(M) \propto M^{-2.35}$ for $M \leq 0.35$ $M_\odot$ down to 0.04 $M_\odot$, steeper than the mass function here, $n(M) \propto M^{-1.3}$ for $M \leq 0.7$ $M_\odot$. As a result, their median lens mass is much smaller than here (0.11 $M_\odot$ versus 0.35 $M_\odot$, weighted by the event rate). The different kinematics may also have a noticeable effect on the timescales, but their more realistic dynamical model does not allow a simple comparison to be made (see also chapter 4).

2.4.4 Fractional contributions to event rate – mass weightings

Fig. 2.15 shows the fractional contributions to the total expected event rate, as a function of event timescale, for the different types of lens (BD, MS, WD, NS and BH). At short timescales ($t_E \lesssim 4$ days), the brown dwarfs dominate the event rate, while at long timescales ($t_E \gtrsim 100$ days), the stellar remnants become increasingly important. There is asymptotic behaviour at both long and short timescales, and it is found that the fractional contribution from a lens of mass M is weighted by $M^2\, n(M)\, \mathrm{d}M$ and $M^{-1}\, n(M)\, \mathrm{d}M$, respectively. In appendix A these weightings are derived from equation (2.8)[3]. Table 2.4 shows that direct calculation of these asymptotic fractions from the mass function gives results that clearly agree with the trends in Fig. 2.15. These weightings are independent of the density and kinematics of the lens population, and hence provide valuable information concerning the lens mass function.

2.4.5 Long timescale excess – slow neutron stars

Fig. 2.14 has shown an excess of observed events at long timescales ($\gtrsim 100$ days) compared to the predicted distribution. The reason for this is unclear. However, the discovery of the double pulsar PSR J0737–3039A/B suggests a possible explanation – it has an unexpectedly slow proper motion, of only 10 mas yr^{-1}, at

[3]The scaling in the long event tail has already been derived by Agol et al. (2002).

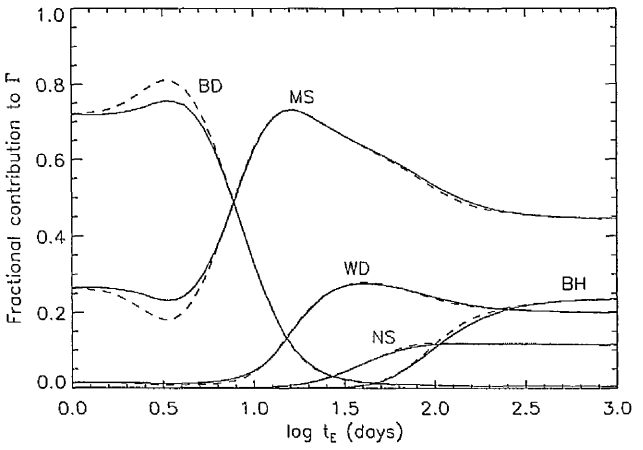

Figure 2.15: Fractional contributions to the total expected event rate, as a function of the event timescale, from BD, MS, WD, NS and BH lenses in the bar (solid lines) and disc (dashed lines). The asymptotic fractions at long and short timescales are a function of the lens mass only (see text).

a distance of ~0.5 kpc (Kramer et al. 2006). This implies a transverse velocity relative to the Sun of ~10 kms^{-1}. It is possible that binary capture could cause a large reduction in a neutron star's initial velocity. If a high fraction of Galactic NS lenses have similarly slow velocities, as members of binaries or even individually, then an excess of long timescale events should be produced. As NS lenses contribute 12% of the total predicted event rate at long timescales (see Table 2.4), the potential significance of this effect is now investigated.

As an initial approximation, a proportion $\mathrm{NS_{slow}}$ of all model NS lenses are given small velocity dispersions: $\sigma_{l,b} = 10$ kms^{-1}. This does indeed produce an excess of long events, but it is of negligible size – even with $\mathrm{NS_{slow}} = 90\%$, it would be undetectable. This is shown in Fig. 2.16 (top panel), where Fig. 2.14 (top panel) is reshown, overplotted with the distribution including slow NS lenses (bold dashed line). The two curves appear indistinguishable. The bottom panel shows the residuals from subtracting the original curve from the latter. The vertical dotted line indicates where the slow NS lenses begin to produce their excess of long events, at 59 days.

The model sources lie only in the bar (as do the observed RCG sources). For interest, disc sources are now considered – the relative transverse velocities between disc lenses and disc sources will be smaller than between disc lenses and

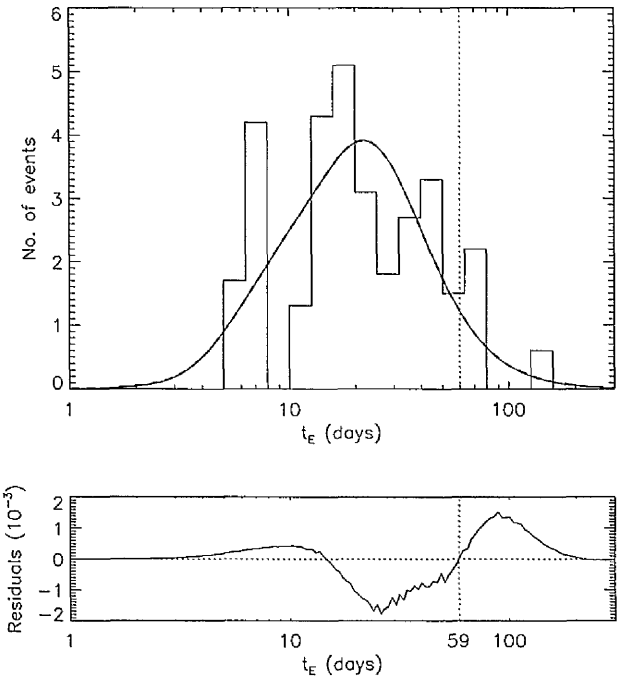

Figure 2.16: Top panel: Microlensing event rate as a function of timescale. Same as top panel of Fig. 2.14, but overplotted with the model distribution including slow NS lenses (bold dashed line). Bottom panel: Residuals from subtracting the original curve from the latter. The vertical dotted line indicates where the slow NS lenses begin to produce a (negligible) excess of long events, at 59 days.

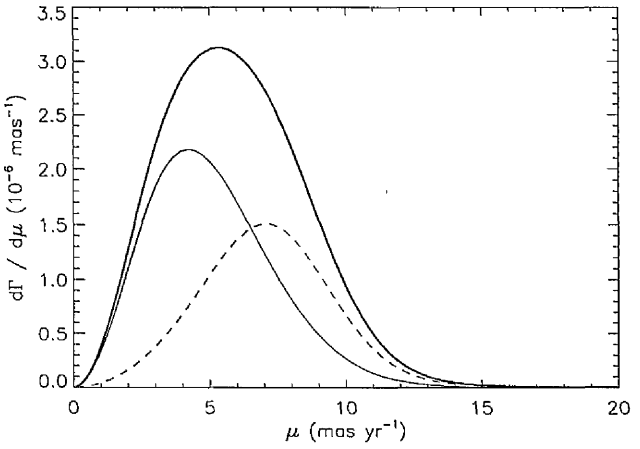

Figure 2.17: Predicted event rate as a function of lens-source relative proper motion, along the OGLE LOS, for bar (thin line), disc (dashed line) and all (bold line) lenses.

bulge sources. Including disc sources in the model, by allowing MS lenses to also act as sources, should therefore produce more long events. This is found to be the case, but the effect is still negligible.

It may thus be concluded that the observed excess of long events cannot possibly be explained by a population of slow neutron stars.

2.4.6 Lens detection

Fig. 2.17 shows the expected event rate as a function of lens-source relative proper motion, for bar (thin line), disc (dashed line) and all (bold line) lenses. As expected, due to their relative distances, the average μ is higher for lenses in the disc than in the bar.

Fig. 2.18 shows the predicted cumulative fractions of MS lenses that are detectable, as a function of elapsed time after the event. Plots are shown for $\theta_{\rm PSF} = 0.05$ and 0.064 arcsec, and for each of the three detection conditions: lens resolution (§2.3.1), total amplification $A' \geq 1.34$ (§2.3.2), and S/N ≥ 3 (§2.3.3). Table 2.5 gives the percentages of detectable MS lenses at $\Delta t = 10$ and 20 yrs, for each case. Note that after 10 yrs, 1–2 % of lenses are expected to be detected with the *HST*. This agrees, at least within an order of magnitude, to observational results discussed in §5.2. The lower limit on detection comes

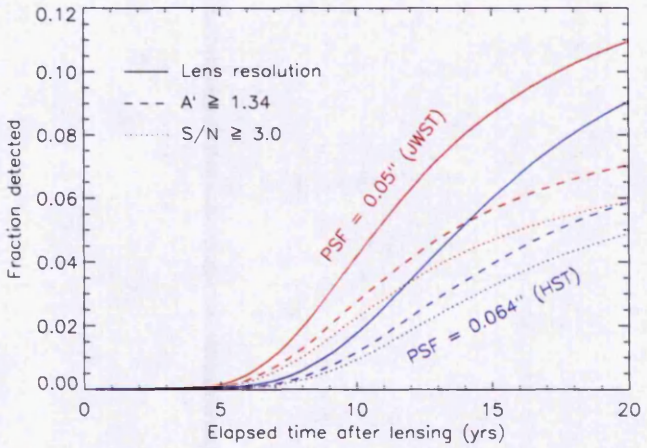

Figure 2.18: Predicted cumulative fraction of detectable MS lenses, as a function of elapsed time after the event. Plots are shown for $\theta_{\rm PSF} = 0.05$ and 0.064 arcsec, and for each of the three detection conditions (see text).

Δt (yrs)	PSF (arcsec)	Resolvable	$A' > 1.34$	$\kappa > 3$
10	0.05	2, 7, 4	2, 4, 3	1, 4, 2
	0.064	1, 3, 2	1, 2, 1	0, 2, 1
20	0.05	9, 14, 11	6, 9, 7	5, 8, 6
	0.064	6, 13, 9	4, 8, 6	4, 7, 5

Table 2.5: Predicted percentages of detectable MS lenses, for a given PSF at a time Δt after lensing, for the three detection conditions described. The sets of three numbers are for (bar, disc, all) lenses.

from the S/N condition: even with $A' \geq 1.34$, there may be too much noise. Although $< 10\%$ of all luminous lenses are expected to be realistically detectable 10–20 yrs after the event, this still represents a useful number of cases. With the first observations occuring over 10 yrs ago, and hundreds of events yr^{-1} now being detected, routine follow-up observations should enable increasing numbers of lenses to be observed and their masses measured (see also §1.4.3, and chapter 5).

2.4.7 Einstein radius distribution

Finally, the event rate is predicted as a function of Einstein radius, θ_{E}. Of particular interest is any similarity to the trends seen as a function of event timescale. Fig. 2.19 shows the expected event rate as a function of θ_{E} towards the OGLE LOS, for bar (thin line), disc (dashed line) and all (bold line) lenses. As a function of timescale (see Fig. 2.13), the predicted event rate shows good agreement with the asymptotic power-law tails $\mathrm{d}\Gamma/\mathrm{d}(\log t_{\mathrm{E}}) \propto {t_{\mathrm{E}}}^3$, ${t_{\mathrm{E}}}^{-3}$ for very short and long timescales, respectively (Mao & Paczyński 1996). Here there is similarly good agreement, for disc and all lenses, with asymptotic power-law tails $\mathrm{d}\Gamma/\mathrm{d}(\log \theta_{\mathrm{E}}) \propto {\theta_{\mathrm{E}}}^3$, ${\theta_{\mathrm{E}}}^{-3}$ at small ($\lesssim 0.1$ mas) and large ($\sim$2 mas) θ_{E}, respectively. However, this is not true for the bar lenses, whose contribution to the event rate drops quickly at larger θ_{E}. This trend is explained shortly.

Figure 2.20 shows the various fractional contributions to the predicted event rate from the different types of lens, for bar, disc and all lenses. We see that (for all lenses) the fractional contributions at large ($\sim$2 mas) and small ($\lesssim 0.1$ mas) θ_{E} are very close to those seen at long and short t_{E}, respectively, in §2.4.4 – see Table 2.6. This is because the timescale is proportional to the Einstein radius: $t_{\mathrm{E}} = D_{\mathrm{d}}\, \theta_{\mathrm{E}}/v$. Hence when θ_{E} is very (large, small), it becomes the dominant factor over D_{d} and v, and t_{E} will also become (large, small).

However, whereas there is little difference between the contributions from bar and disc lenses as a function of timescale, here they are quite different. For bar lenses, the event rate contribution peaks at successively larger values of θ_{E} for BD, MS, WD, NS and BH lenses. From equation (1.4),

$$\theta_{\mathrm{E}} = \left(\frac{4GM}{c^2} \frac{D_{\mathrm{ds}}}{D_{\mathrm{d}} D_{\mathrm{s}}} \right)^{1/2},$$

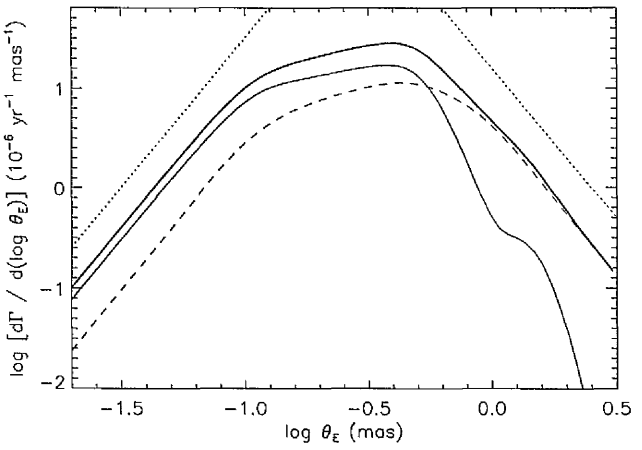

Figure 2.19: Predicted event rate as a function of Einstein radius, along the OGLE LOS, for bar (thin line), disc (dashed line) and all (bold line) lenses. The two dotted lines are asymptotic tails $d\Gamma/d(\log \theta_E) \propto {\theta_E}^3$, ${\theta_E}^{-3}$ for small and large θ_E, respectively.

	BD	MS	WD	NS	BH
Long timescale	0.53	44	20	12	24
$\theta_E = 2.0$ mas	0.37	40	18	14	27
Short timescale	72	27	1.5	0.078	0.0032
$\theta_E = 0.01$ mas	72	27	1.5	0.077	0.0029

Table 2.6: Percentage contributions to the total predicted event rate from the different lenses, at long and short timescales, and large ($\sim$2 mas) and small ($\lesssim$ 0.1 mas) θ_E. The values at $\theta_E = (2.0, 0.01)$ mas are close to those at (long, short) timescales.

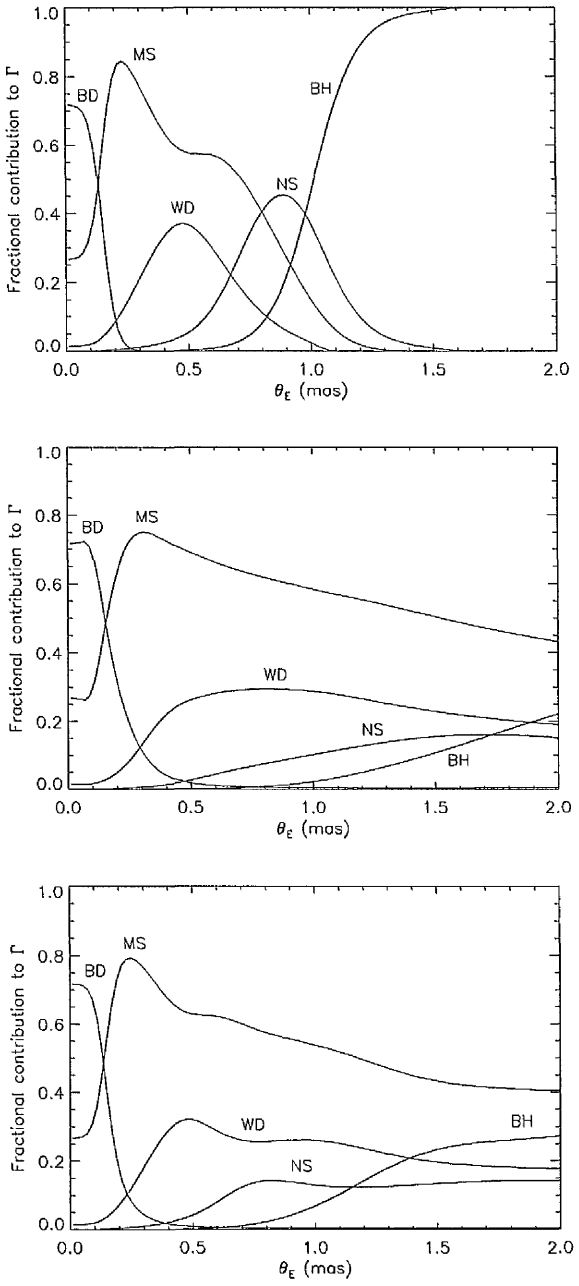

Figure 2.20: Fractional contributions to the total expected event rate as a function of Einstein radius, from BD, MS, WD, NS and BH lenses. (Top, middle, bottom) panel: (bar, disc, all) lenses.

we see that $\theta_{\rm E} \propto M^{1/2}$. In the G2 model of the bulge the matter density increases steeply towards the centre. Therefore most bar lenses and sources will be concentrated in a relatively small region of the Galaxy. As they also outnumber the lenses and sources in the less dense disc, $D_{\rm d}, D_{\rm s}$ and $D_{\rm ds}$ will vary relatively little, allowing M to be the dominant factor in the equation. Therefore more massive lenses will generally have larger Einstein radii. This is clearly seen with the bar lenses. This also means that, since there are few very massive lenses, the total contribution from all bar lenses will be small at large $\theta_{\rm E}$, as seen in Fig. 2.19. Disc lenses, however, are spread over a much wider range of distances, reducing the influence of M. Hence, although the event rate contributions still peak at greater M for more massive lenses, the peaks are much wider, especially at larger $\theta_{\rm E}$.

2.5 Summary and conclusions

In this chapter a simple Galactic model, normalised by *HST* star counts, has been used to predict the microlensing optical depth. Combined with simple kinematic models, maps and distributions of τ and $t_{\rm E}$ have also been predicted. It has been shown that the fraction of long and short events contributed by a lens of mass M is weighted by $M^2\, n(M)\, {\rm d}M$ and $M^{-1}\, n(M)\, {\rm d}M$, respectively. If the tails of this distribution can be accurately determined from observations, we have a direct probe of the lens mass function. Similar asymptotic behaviour has been seen as a function of Einstein radius. It has been estimated that a few per cent of luminous lenses should be detected from follow-up observations of events, by both the *HST* and *JWST*, after 10–20 yrs.

It is remarkable that this empirically normalised model based on the *COBE* G2 model (Dwek et al. 1995) shows good agreement with data recently published by the MACHO and OGLE collaborations (Popowski et al. 2005; Sumi et al. 2006) for the optical depth in various Galactic fields, and with the trends with l and b seen by MACHO, OGLE and EROS (Hamadache et al. 2006). The maps of optical depth and average event timescale cover a large area of the sky, and can be compared with future determinations of τ in similar areas when they become available. The expected distribution of the event timescale also appears to show good agreement with the recently published OGLE data (Sumi et al. 2006).

However, there is slightly poorer agreement with the corresponding EROS distribution (Hamadache et al. 2006), which is based on more events. The principle difference between the model and the data is the greater number of observed long events. Following the discovery of a slow-moving binary pulsar, the potential of a population of slow-moving neutron star lenses to explain this excess has been examined, but only a negligible effect was found.

The numbers of microlensing events in the recent OGLE, MACHO and EROS analyses – 32, 42 and 120, respectively – are still small, so the test on the models is not yet stringent. When the much larger databases of all microlensing events (of the order of thousands) are analysed, then a full comparison with the models will become much more discriminating.

References

Afonso C. et al., 2003, A&A, 404, 145

Agol E., Kamionkowski M., Koopmans L.V.E., Blandford R.D., 2002, ApJ, 576, L131

Alcock C. et al., 2000, ApJ, 541, 734

Bissantz N., Gerhard O., 2002, MNRAS, 330, 591

Bissantz N., Debattista V.P., Gerhard O., 2004, ApJ, 601, L155

Blum R.D., 1995, ApJ, 444, L89

Cox A.N., 1999, Allen's Astrophysical Quantities, 4th edn. Springer–Verlag, New York, p. 489

Dwek E. et al., 1995, ApJ, 445, 716

Evans N.W., Belokurov V., 2002, ApJ, 567, L119

Griest K., 1991, ApJ, 366, 412

Hamadache C. et al., 2006, A&A, 454, 185

Han C., Chang H.-Y., 2003, MNRAS, 338, 637

Han C., Gould A., 1995, ApJ, 447, 53

Han C., Gould A., 2003, ApJ, 592, 172 (HG03)

Holtzman J.A., Watson A.M., Baum W.A., Grillmair C.J., Groth E.J., Light R.M., Lynds R., O'Neil E.J., 1998, AJ, 115, 1946

Kiraga M., Paczyński B., 1994, ApJ, 430, L101

Kozłowski S., Woźniak P.R., Mao S., Smith M.C., Sumi T., Vestrand W.T., Wyrzykowski Ł., 2006, MNRAS, 370, 435

Kramer M. et al., 2006, Sci, accepted, preprint astro-ph/0609417

Kuijken K., Rich R.M., 2002, AJ, 124, 2054

Mao S., Paczyński B., 1996, ApJ, 473, 57

Paczyński B., 1991, ApJ, 371, L63

Paczyński B., 1996, ARA&A, 34, 419

Peale S.J., 1998, ApJ, 509, 177

Popowski P. et al., 2001, in Menzies J.W., Sackett P.D., eds, ASP Conf. Ser. Vol. 239, Microlensing 2000: a New Era in Microlensing Astrophysics, Astron. Soc. Pac., San Francisco, p. 244

Popowski P. et al., 2005, ApJ, 631, 879

Stanek K.Z., 1995, ApJ, 441, L29

Sumi T., Eyer L., Woźniak P.R., 2003, MNRAS, 340, 1346

Sumi T. et al., 2006, ApJ, 636, 240

Wood A., Mao S., 2005, MNRAS, 362, 945

Zheng Z., Flynn C., Gould A., Bahcall J.N., Salim S., 2001, ApJ, 555, 393

Zoccali M., Cassisi S., Frogel J.A., Gould A., Ortolani S., Renzini A., Rich R.M., Stephens A.W., 2000, ApJ, 530, 418

Chapter 3

Optical depth as a function of source apparent magnitude

This chapter considers the discrepancies in optical depth measurements obtained from RCGs and from all stars, and investigates the effects of the different flux limits involved. τ is predicted as a function of source apparent magnitude, and the resulting trends are explained and compared with the latest EROS data. Combining the optical depth predictions with observed values, constraints are placed on the inclination angle of the Galactic bar. Parts of the work in this chapter appear in Wood (2006).

3.1 Introduction

As mentioned previously, thousands of microlensing events in our Galaxy have now been discovered by OGLE (e.g. Woźniak et al. 2001), MACHO (e.g. Thomas et al. 2005), MOA (e.g. Sumi et al. 2003) and EROS (e.g. Afonso et al. 2003), and one of the most important measurements that can be made from these observations is of the optical depth, τ – the probability of seeing a microlensing event. However, the measured value appears to depend strongly on the method used to obtain it.

As also discussed previously, Popowski et al. (2005) reported $\tau_{\rm MACHO} = 2.17^{+0.47}_{-0.38} \times 10^{-6}$ at $(l, b) = (1.50°, -2.68°)$, and more recently from the OGLE-II survey, Sumi et al. (2006) found $\tau_{\rm OGLE} = 2.55^{+0.57}_{-0.46} \times 10^{-6}$ at $(l, b) = (1.16°, -2.75°)$. The MACHO value was based on the lensing of 42 red clump giants (RCGs), and used standard photometric fitting. The OGLE analysis instead used difference image analysis (DIA, see §1.4.2), but was similarly based on the lensing of 32 red giants, red super giants and RCGs, and obtained an optical depth consistent with the previous MACHO result. However, both these values are significantly lower than two other recent measurements, which were based on the lensing of all stars. Using 28 MOA DIA events, Sumi et al. (2003) found $\tau = 3.36^{+1.11}_{-0.81} \times 10^{-6} [0.77/(1 - f_{\rm disc})]$, where $f_{\rm disc}$ is the contribution from disc sources – the coordinates of this value are given in Sumi et al. (2006): $(l, b) = (3.0°, -3.8°)$. Alcock et al. (2000) had previously found $\tau = 3.23^{+0.52}_{-0.50} \times 10^{-6} [0.75/(1 - f_{\rm disc})]$ at $(l, b) = (2.68°, -3.35°)$, from 99 MACHO DIA events. The latest measurement comes from the EROS-2 survey of bulge RCGs, which yielded 120 events: Hamadache et al. (2006) give the trend $\tau = (1.62 \pm 0.23) \exp[-a(|b| - 3 \text{ deg})] \times 10^{-6}$, where $a = (0.43 \pm 0.16 \text{ deg}^{-1})$, in the latitude range $1.4° < |b| < 7.0°$. This agrees well with previous EROS values, and with the recent MACHO and OGLE-II measurements.

The question naturally arises as to why the RCG-based optical depths appear to be lower than those from all stars. One possibility is a dependence on the flux limits of the two methods. RCGs are bright; the latter method will include much fainter stars, and so probe sources at greater distances, which will have a higher optical depth (Stanek 1995).

This potential explanation of the discrepancy is investigated using Monte Carlo simulations of Galactic microlensing, and the optical depth as a function of source apparent magnitude is then predicted. The model Galaxy is barred,

and in light of observations by the *Spitzer Space Telescope* (*SST*), that support a bar inclination angle much larger than suggested by previous studies (see §3.2.1), the effect on the expected τ of changing the bar angle is determined. Combining these results with the observed optical depths, upper limits are placed on the bar angle. §3.2 describes the model. The results and discussion are presented in §3.3: the model results are given in §3.3.1, and comparisons are made with the latest EROS-2 data in §3.3.2. A summary and conclusions follow in §3.4.

3.2 The model

3.2.1 Bulge and disc mass models

The mass models and parameters of the Galactic bulge (bar) and disc are as described in chapter 2. They are based on those of Han & Gould (2003), who empirically normalised the G2 bulge model of Dwek et al. (1995, table 1) with *Hubble Space Telescope* star counts, and extended the local disc model of Zheng et al. (2001) to the whole disc. Dwek et al. tested a series of models against images of the Galactic bulge from the *Cosmic Background Explorer* (*COBE*) satellite, and found their G2 model to provide one of the best fits. This model bar extends from 3–13 kpc and is inclined to the Galactic centre line of sight (LOS) at an angle of $\theta_{\rm bar} = 13.4°$. Gerhard (2002) states that physical models can be found for the *COBE* bar with angles in the range $15° \lesssim \theta_{\rm bar} \lesssim 35°$, and many studies assume $\theta_{\rm bar} \approx 20°$. However, more recent data from GLIMPSE (Galactic Legacy Infrared Mid-Plane Survey Extraordinaire), using the *SST*, support a much larger value of $(44 \pm 10)°$ (Benjamin et al. 2005), while from EROS-2, Hamadache et al. (2006) report $\theta_{\rm bar} = (49 \pm 8)°$, which is consistent with original OGLE-I results (Stanek et al. 1994). Hence, predictions are also made here for Dwek et al.'s E2 model, which has the largest bar angle of their models: $\theta_{\rm bar} = 41.3°$.

3.2.2 Source population

The expected $\tau_{\rm OGLE}$, $\tau_{\rm MACHO}$ and $\tau_{\rm MOA}$ are to be calculated. Therefore for each LOS, the apparent magnitude distribution of the model sources must match the observed distribution. Sumi (2004) fitted the I-band stellar distributions in 48

	l (°)	b (°)	Angular separation (°)
OGLE	1.16	-2.75	
Field 34	1.35	-2.40	0.40
MACHO	1.50	-2.68	
Field 20	1.68	-2.47	0.28
MOA	3.0	-3.8	
Field 36	3.16	-3.20	0.6

Table 3.1: Selection of the OGLE-II Galactic bulge fields that are closest to the lines of sight of the OGLE, MACHO (RCG) and MOA optical depth measurements.

OGLE-II Galactic bulge fields with the power-law plus Gaussian luminosity function

$$\phi_I(I) = p_0 10^{p_1 I} + p_2 \exp\left[-\frac{(I - \langle I\rangle_{\rm RC})^2}{2\sigma^2_{I,\rm RC}}\right], \tag{3.1}$$

where p_0, p_1, p_2 and $\sigma_{I,\rm RC}$ are free parameters, and $\langle I\rangle_{\rm RC}$ is measured as described in his paper. The power-law part contains red giants and bright main-sequence stars, which lie throughout the bar. The Gaussian component consists of RCGs, which in the model are more concentrated in the central part of the bulge, occupying the region 6–10 kpc. (This concentration is found to improve the match to the observed magnitude distributions, and is not unreasonable, as RCGs are older, evolved stars, and hence more likely to exist only in more densely populated regions).

Sumi (2004) thus provides, for each of these fields, an observed distribution of apparent magnitude. The positions of these fields are listed in table 1 of Udalski et al. (2002). The fields closest to the OGLE, MACHO (RCG) and MOA lines of sight are selected, as shown in Table 3.1. The MACHO (DIA) LOS is not considered, as explained below.

As described in §3.2.3, the apparent magnitude of each source is calculated by first assigning it an absolute magnitude, and then correcting for its distance. Hence for each LOS a separate model distribution of absolute magnitude is required that will, with distance corrections, reproduce the observed distribution of apparent magnitude. Of course in reality the absolute magnitude distribution should be virtually the same for each direction in Table 3.1, since over these small angular separations the mass function is expected to vary little. Here, the

	$I_{0,\min}$	$I_{0,\max}$
OGLE	12.1	15.3
MACHO	13.9	16.2
	($V = 16.37$)	($V = 20.19$)
MOA	13.6	20.8

Table 3.2: Defined ranges of detectable apparent magnitudes for OGLE, MACHO and MOA.

artificial absolute magnitude distributions are only used as a means to ensure the model distributions of apparent magnitude match those observed for each direction. It is assumed that the forms of the two distributions are the same, i.e. a power-law plus Gaussian. For each of the three OGLE-II fields listed in Table 3.1, an appropriate absolute magnitude distribution can easily be generated, by suitably adjusting the (extinction-corrected) fitted parameters of the apparent magnitude distribution found by Sumi (2004). (These parameters are not given in Sumi (2004), and are provided by Sumi, private communication).

Sumi et al. (2003, table 5) and Sumi et al. (2006, table 4) list the extinction-corrected I-band apparent magnitudes of all the MOA and OGLE sources used in their respective measurements of τ. The minimum and maximum magnitudes given in each case are taken to define ranges of detectable apparent magnitudes. Popowski et al. (2005), in their table 2, provide uncorrected V-band apparent magnitudes. Since these MACHO sources are all RCGs, their apparent magnitudes are converted to I-band using the following relation for RCGs from Sumi et al. (2003):

$$I = (1.45 \pm 0.12)\,(V - I) + 12.7. \tag{3.2}$$

MACHO source extinction is then accounted for by simply shifting the minimum and maximum MACHO magnitudes by the mean A_I for the corresponding OGLE-II field, as given in table 3 of Sumi (2004): for field 20, $A_I = 0.951$. (Strictly speaking the extinction should instead be calculated for each source individually, following equation (2.3), but this is neglected as in the region occupied by model RCGs, the expected A_I differs from the mean value by ≤ 0.05 mag – a negligible amount). Although Alcock et al. (2000) also list the apparent magnitudes of the MACHO sources used in their DIA measurement, these are in V-band and do not consist of only RCGs. Therefore an I-band magnitude range cannot be reliably defined for the model. The defined ranges of detectable, extinction-corrected apparent magnitudes I_0 for OGLE, MACHO and MOA are given in Table 3.2.

	(l, b) (°)	$\tau_{\rm obs}$ $(\times 10^{-6})$	$\tau_{\rm model,G2}$ $(\times 10^{-6})$	$\tau_{\rm model,E2}$ $(\times 10^{-6})$
OGLE	(1.16, -2.75)	$2.55^{+0.57}_{-0.46}$	2.14	1.57
MACHO	(1.50, -2.68)	$2.17^{+0.47}_{-0.38}$	2.19	1.61
MOA	(3.0, -3.8)	$3.36^{+1.11}_{-0.81}$ $(2.59^{+0.84}_{-0.64})$	1.38	1.01

Table 3.3: The expected G2 optical depths agree well with those reported by OGLE and MACHO, but not with MOA's values. (The numbers in parentheses are without the DIA correction for disc sources – see text).

3.2.3 Optical depth

The expected $\tau_{\rm OGLE}$, for example, can now be calculated as follows. First a distance $D_{\rm s}$ is chosen for a given source along the OGLE LOS. It is assigned an absolute magnitude using the artificial distribution constructed for the nearest OGLE-II field, #34. The source's apparent magnitude is then calculated by accounting for its distance.

If this apparent magnitude falls within the defined range of magnitudes detectable by OGLE, the source is included in the calculation of τ using equation (2.7) as described in §2.2.5. This process is then repeated for many sources. The expected $\tau_{\rm MACHO}$ and $\tau_{\rm MOA}$ are similarly calculated.

3.3 Results and discussion

3.3.1 Model results

Fig. 3.1 shows that the model well reproduces the observed distributions of apparent magnitude for fields 20, 34 and 36. Table 3.3 shows that the expected values of $\tau_{\rm OGLE}$ and $\tau_{\rm MACHO}$ also agree well with the observed values, for the G2 model. However, the expected $\tau_{\rm MOA}$ lies $\sim 2.4\sigma$ below the reported value. As the MOA measurement is sensitive to *all* sources along the LOS, a correction was applied to account for disc sources. This is expressed by the $f_{\rm disc}$ term in the τ measurements quoted in §3.1. Such adjustments typically raise τ by $\sim$25%. Note that the model underpredicts $\tau_{\rm MOA}$ by a much greater margin, hence the disagreement cannot be attributed to the correction applied by MOA. It therefore appears that the discrepancy in the survey measurements cannot be simply explained by a dependance on their different flux limits.

However, there may be other ways in which τ depends on the source flux.

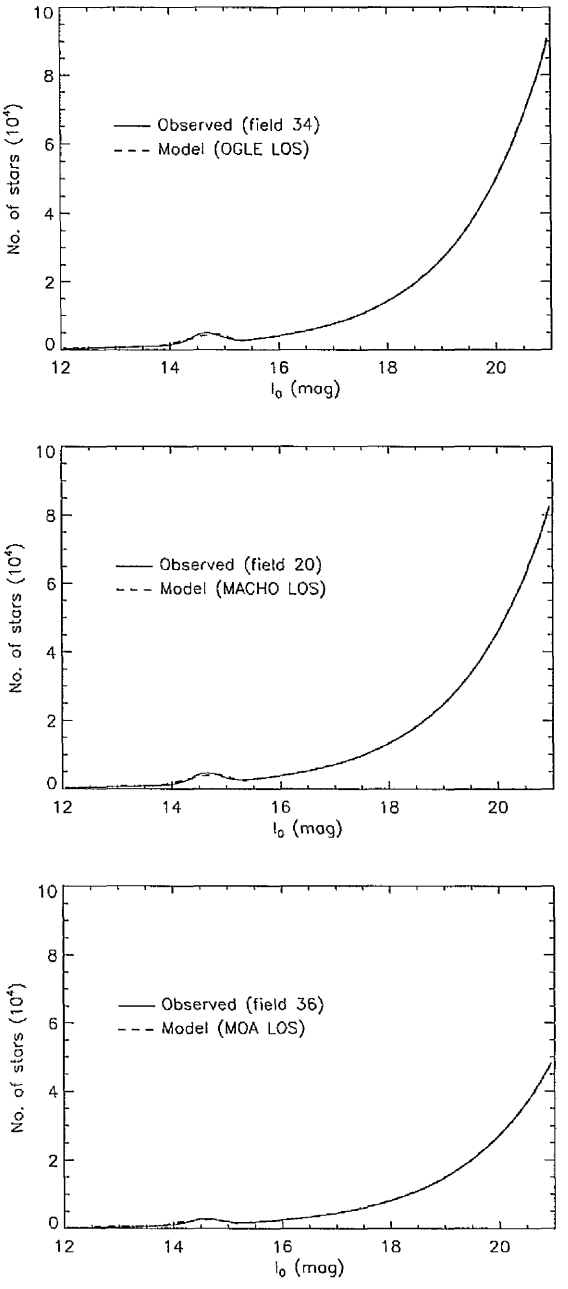

Figure 3.1: (Top, middle, bottom) panel: Apparent magnitude distributions, for stars observed in OGLE-II field (34, 20, 36) by Sumi (2004), and model stars along the (OGLE, MACHO, MOA) LOS. These plots are for the G2 model – there is negligible difference with E2. The model curves are normalised to the same area as the corresponding observed curves.

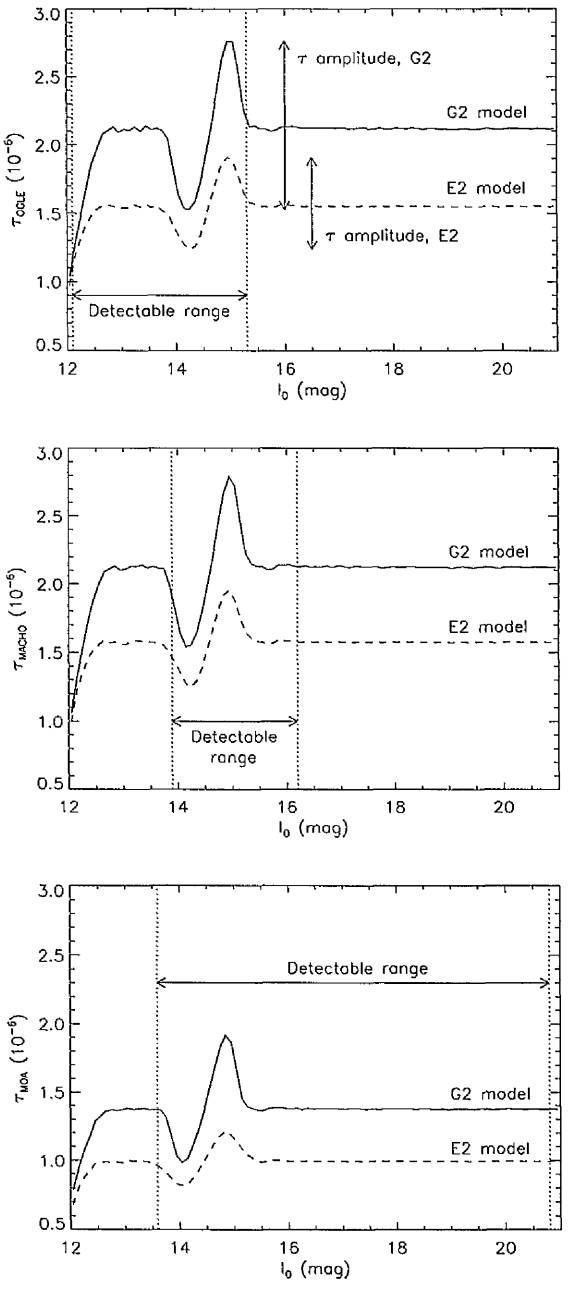

Figure 3.2: (Top, middle, bottom) panel: Expected ($\tau_{\rm OGLE}$, $\tau_{\rm MACHO}$, $\tau_{\rm MOA}$) as a function of source apparent magnitude, for the G2 and E2 models. The detectable magnitude ranges given in Table 3.2 are shown. In the top panel, the amplitude of the $\tau_{\rm OGLE}$ oscillation (see text) is indicated for both the G2 and E2 models.

So far the predicted optical depths have been calculated by summing over all the source stars whose apparent magnitudes fall within specified ranges. By repeating this process for many small bins of I_0, τ can be predicted as a function of I_0. This is plotted in Fig. 3.2, for the OGLE, MACHO and MOA coordinates. The detectable magnitude ranges given in Table 3.2 are also shown. For each LOS the absolute expected value of τ is higher for the G2 bar than the E2, but its trend with magnitude is similar. These trends are explained as follows.

τ increases rapidly over the range $12 \lesssim I_0 \lesssim 13$. Almost all sources of magnitude $\sim$12 will be on the near side on the bulge, so as I_0 increases fainter and more distant stars, with higher optical depths, come into view. For $I_0 \gtrsim 15.5$, τ is approximately constant. This is because the power-law part of the source magnitude distribution spans a wide range of I_0. Hence these stars can be either bright or faint whether they are near or far, and thus will show little or no correlation between apparent magnitude and distance. So, when calculating the average τ for a given apparent magnitude, the lower optical depth of the closer stars is balanced by the higher τ of those more distant.

In comparison, the Gaussian (RCG) part of the source distribution covers only a very narrow range of absolute magnitudes. The RCGs' distribution in apparent magnitude will be broader, due to variations in their distance, but as they are more concentrated in the centre of the bulge, this broadening is not great. Therefore the vast majority of RCGs will lie within a small range of apparent magnitude, and hence show a strong correlation between apparent magnitude and distance. At $I_0 \sim$14 we see many RCGs, and they greatly outnumber the other sources. Most of the RCGs at this magnitude lie on the near side of the bulge, and τ is lower. As I_0 increases, the average distance of the RCGs (and so of all sources) being observed shifts towards the far side of the bulge, and τ increases. As I_0 becomes fainter still, $\gtrsim 15$, we see fewer and fewer RCGs, and the average distance of all the observed sources moves back towards the centre of the bulge, where it then remains, and τ becomes approximately constant. The amplitude of this oscillation in τ (hereafter the τ *amplitude*) caused by the RCGs along the OGLE LOS is indicated in the top panel of Fig. 3.2.

This strong correlation displayed by the RCGs is illustrated as follows. In Figs. 3.3 and 3.4, contours are plotted of source counts as a function of distance and apparent magnitude along each LOS, for the G2 and E2 models, respectively. The two components of the source population are clearly distinguishable. For

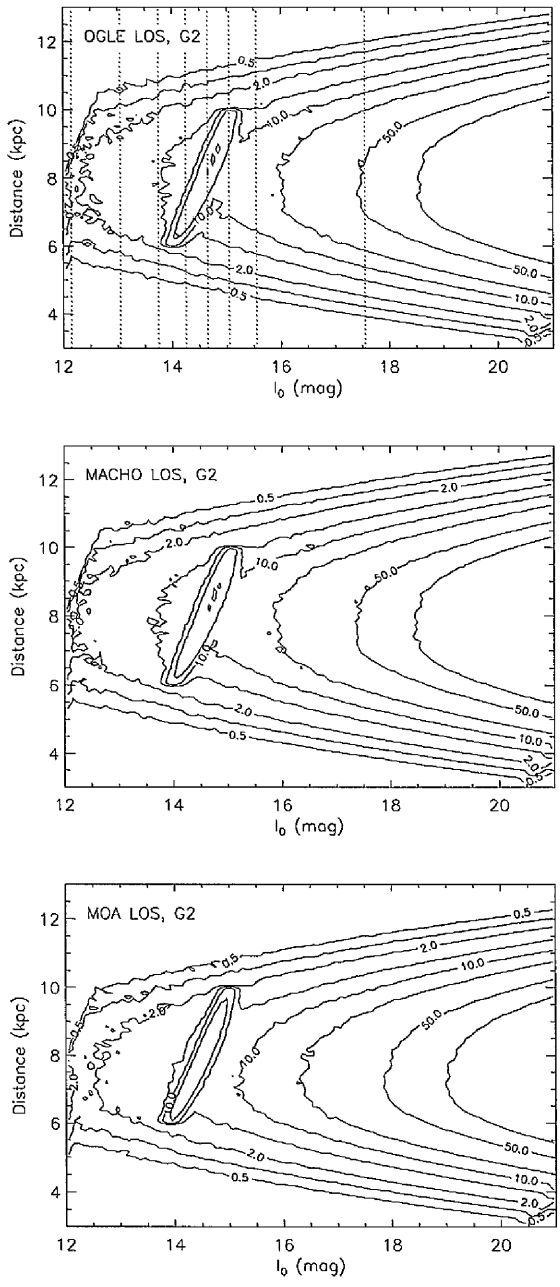

Figure 3.3: (Top, middle, bottom) panel: G2 model source counts as a function of distance and apparent magnitude, for the (OGLE, MACHO, MOA) coordinates. The RCG component is clearly visible (see text). The vertical dotted lines (top panel) correspond to the slices shown in Fig. 3.5 (see text). The normalisation is arbitrary. Contour levels are at (0.5, 1.0, 2.0, 5.0, 10.0, 20.0, 50.0, 100.0).

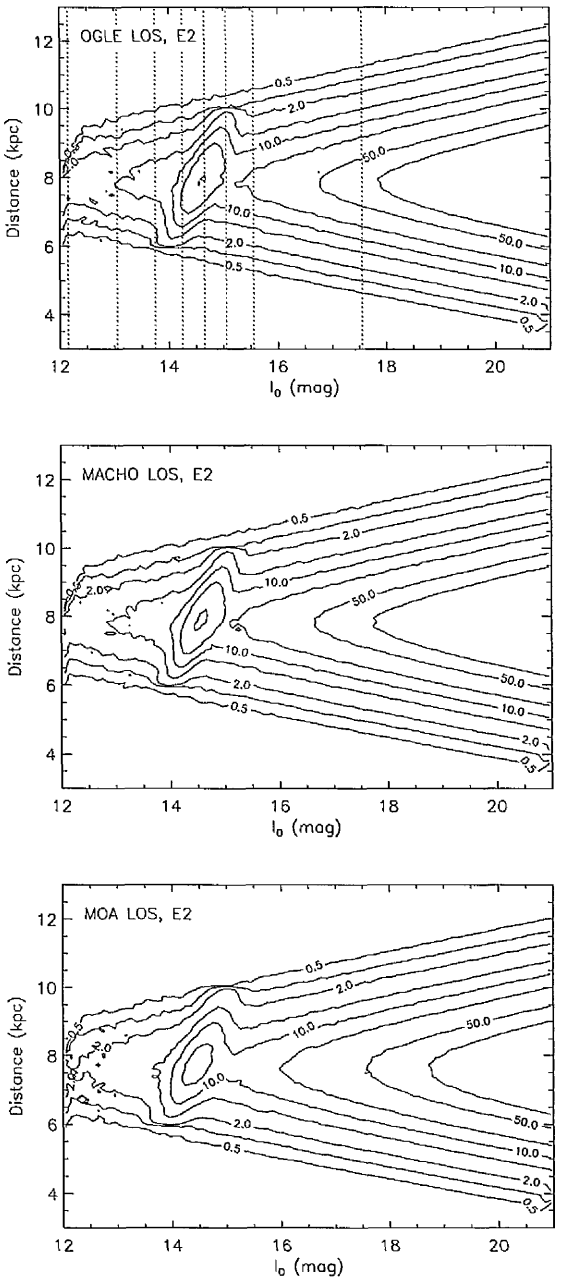

Figure 3.4: Model source counts as a function of distance and apparent magnitude. Same as Fig. 3.3, but for the E2 model, with the vertical dotted lines corresponding to the slices shown in Fig. 3.6 (see text). The normalisation is arbitrary, but consistent with Fig. 3.3.

the G2 model, most of the RCGs appear as a narrow diagonal line in the range $14.0 \lesssim I_0 \lesssim 15.0$. For E2, this region is wider (for a given distance) and shallower. These differences in shape are primarily due to the different bar angles of the G2 and E2 models (13.4° and 41.3°, respectively). The red giants and other stars form a smoother background, with a steep increase in numbers, and a broadening in distance, as I_0 increases. In the top panels of Fig. (3.3, 3.4), the vertical dotted lines indicate slices of this distribution – for the OGLE LOS – that are shown in Fig. (3.5, 3.6). Finally, the top panel of Fig. 3.7 gives the average distance of model OGLE sources as a function of I_0. The slice magnitudes are indicated, and the bottom panel shows how they intersect the $\tau_{\rm OGLE}$ trend from Fig. 3.2. Note that the trends of average source distance and optical depth with I_0 are almost identical, as would be expected for the reasons given above.

The expected oscillation in τ caused by the RCGs is clearly significant. For example, Fig. 3.2 shows that the τ amplitude along the OGLE LOS is $\sim 1.2 \times 10^{-6}$. This is a deviation of $\sim \pm 30\%$ from the approximately constant optical depth at fainter magnitudes (hereafter $\tau_{\rm flat}$), where far fewer RCGS are seen: $\tau \sim 2.1 \times 10^{-6}$. For comparison, OGLE's measured value of $2.55^{+0.57}_{-0.46} \times 10^{-6}$ has an uncertainty of only $\sim \pm 20\%$, so the predicted oscillation ought to be detectable if enough sources are observed at the correct magnitudes.

Fig. 3.8 shows that the expected amplitudes of $\tau_{\rm OGLE}$, $\tau_{\rm MACHO}$ and $\tau_{\rm MOA}$ all decrease with increasing bar angle. This provides a potential constraint on $\theta_{\rm bar}$, should the expected τ amplitude be observed and its magnitude accurately measured. Another constraint is shown by Fig. 3.9, where the expected optical depths $\tau_{\rm OGLE}$, $\tau_{\rm MACHO}$ and $\tau_{\rm MOA}$ display a similar dependance on $\theta_{\rm bar}$. The corresponding observed values are overplotted, with their 1σ uncertainties, and from the intersections with the predicted OGLE and MACHO curves, 1σ upper limits on $\theta_{\rm bar}$ are obtained. (There is no intersection between the predicted and observed $\tau_{\rm MOA}$). These limits are given in Table 3.4. Note that the large bar angle of the E2 model ($\theta_{\rm bar} = 41.3°$) is ruled out at the 1σ level, as are those from GLIMPSE ($\theta_{\rm bar} = (44 \pm 10)°$) and EROS ($\theta_{\rm bar} = (49 \pm 8)°$).

3.3.2 Comparison with EROS data

The EROS-2 survey (Hamadache et al. 2006) has found the largest sample of clump-giant events so far, 120, compared with 32 and 62 for the latest OGLE and MACHO surveys, respectively. This sample may be sufficient to enable a

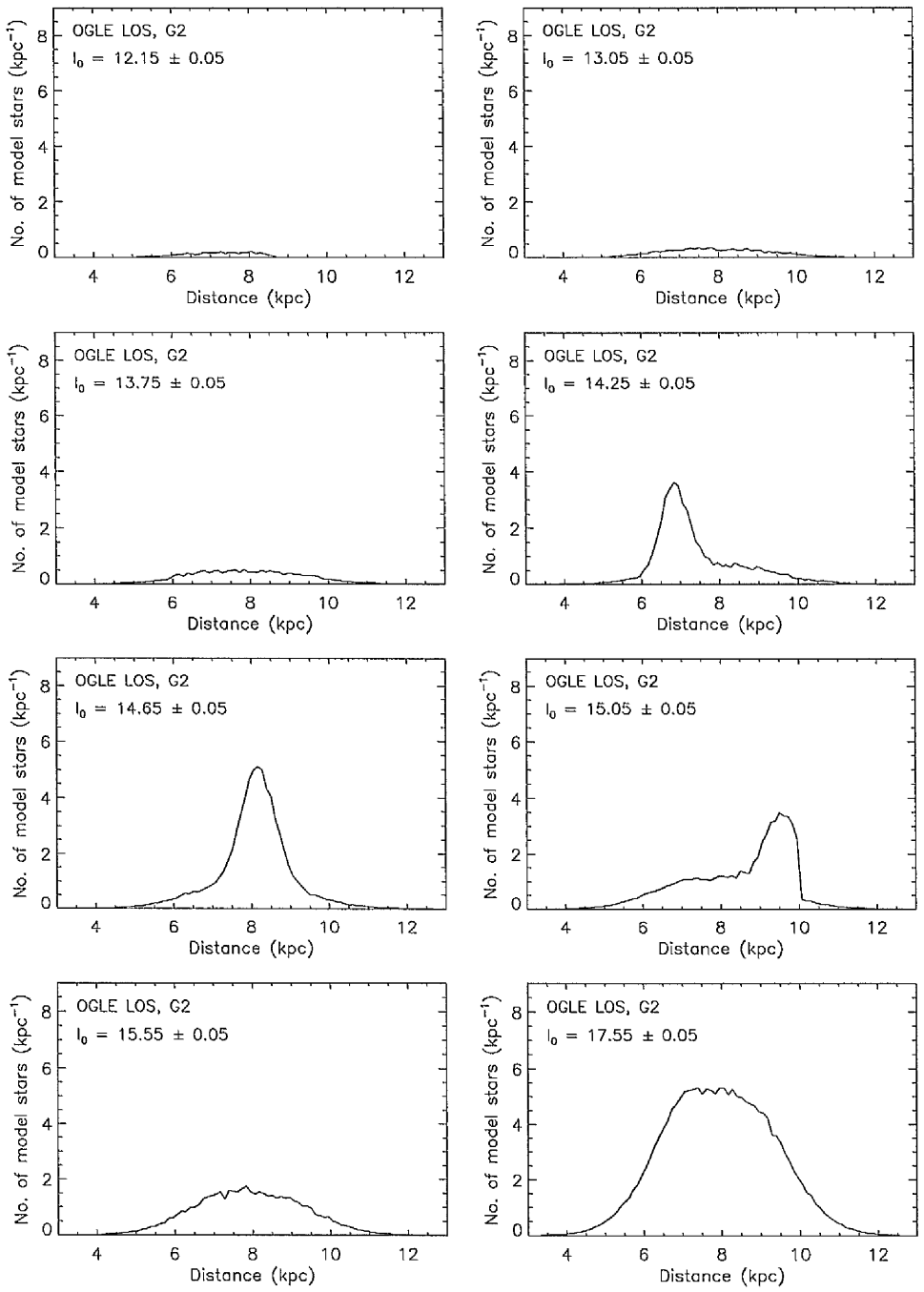

Figure 3.5: Model source counts as a function of distance (OGLE LOS, G2 model), for selected apparent magnitudes I_0 (with I_0 bin widths of 0.1 mag). These magnitudes are indicated in the panels, and correspond to the slices indicated in Fig. 3.3 (top panel).

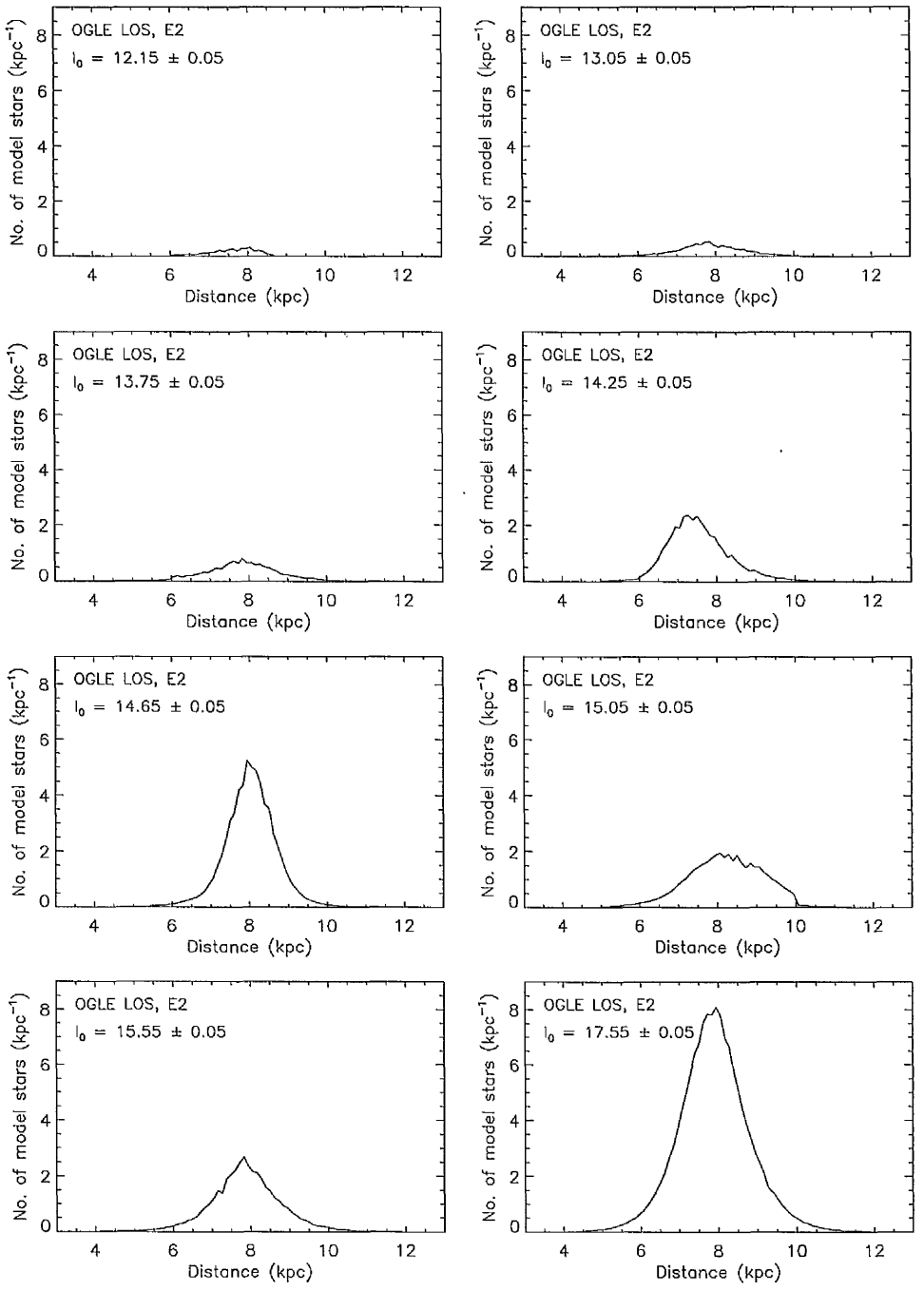

Figure 3.6: Model source counts as a function of distance. Same as Fig. 3.5, but for the E2 model, with the selected magnitudes corresponding to the slices indicated in Fig. 3.4 (top panel).

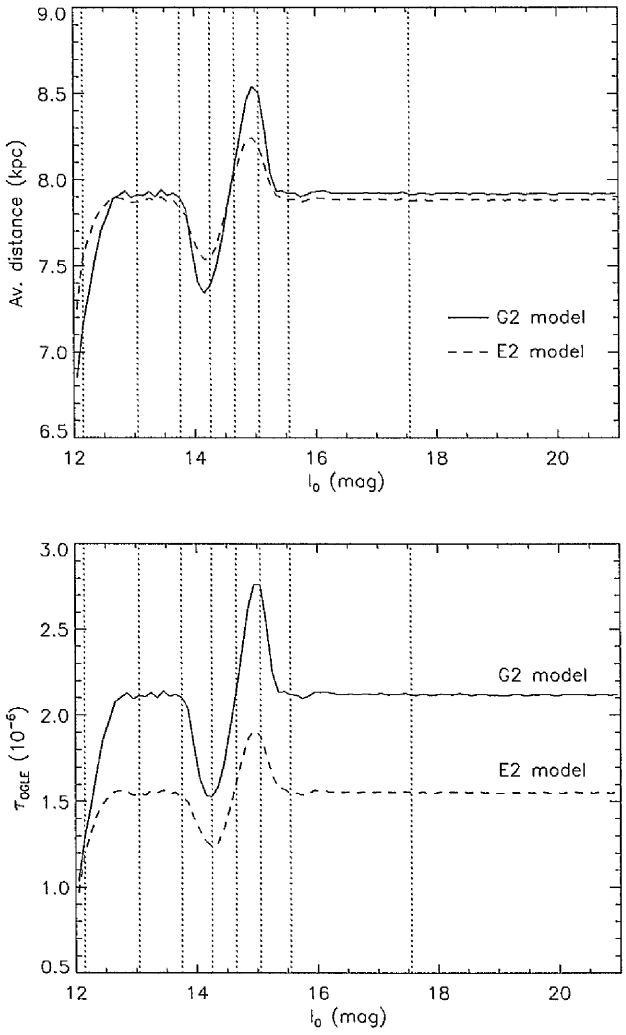

Figure 3.7: Top panel: Average distance of model OGLE sources as a function of magnitude. Bottom panel: $\tau_{\rm OGLE}$ as a function of magnitude (same as top panel of Fig. 3.2). The vertical dotted lines correspond to the slice magnitudes indicated in Figs. 3.3 – 3.6.

	(l, b) (°)	$\theta_{\rm bar,G2}$ (°)	$\theta_{\rm bar,E2}$ (°)
OGLE	(1.16, -2.75)	15.8	20.4
MACHO	(1.50, -2.68)	24.6	31.0

Table 3.4: 1σ upper limits on $\theta_{\rm bar}$, from combining the expected optical depths with those measured by OGLE and MACHO (see text). Values are shown for the G2 and E2 bar models.

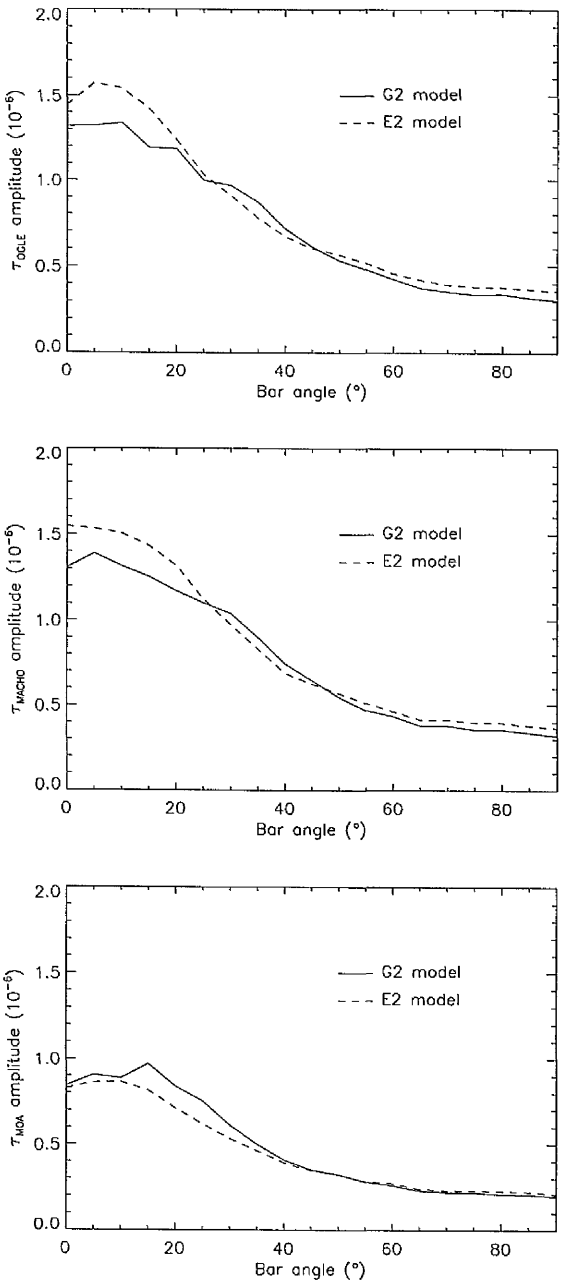

Figure 3.8: (Top, middle, bottom) panel: Oscillation amplitude of expected ($\tau_{\rm OGLE}$, $\tau_{\rm MACHO}$, $\tau_{\rm MOA}$) as a function of $\theta_{\rm bar}$, for the G2 and E2 models.

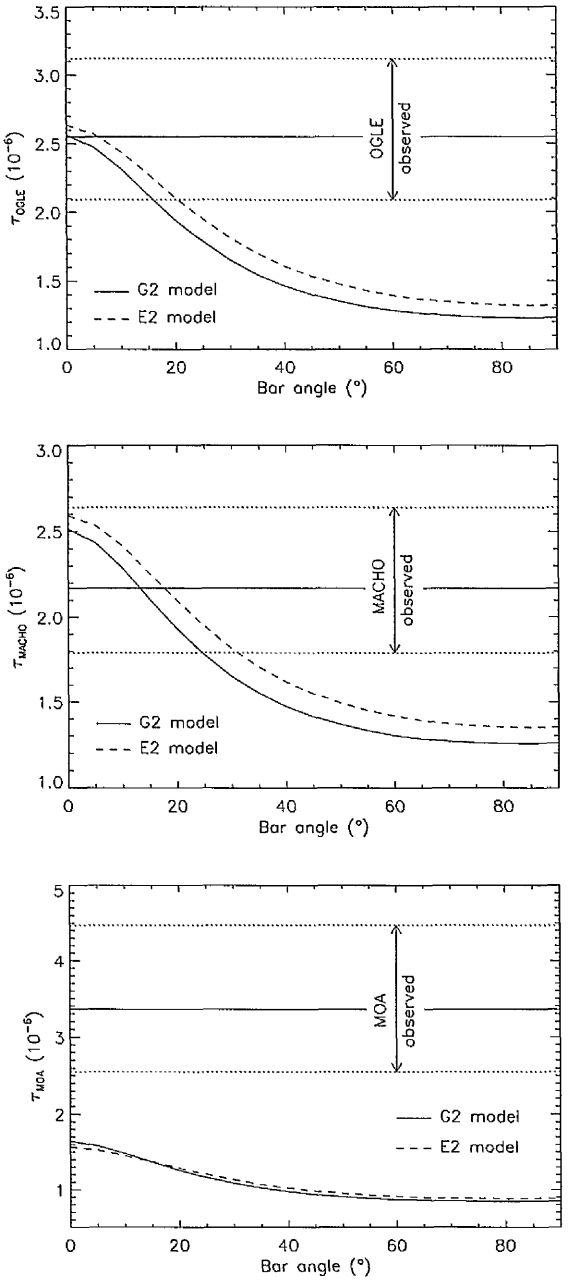

Figure 3.9: (Top, middle, bottom) panel: Expected ($\tau_{\rm OGLE}$, $\tau_{\rm MACHO}$, $\tau_{\rm MOA}$) as a function of $\theta_{\rm bar}$, for the G2 and E2 models. The horizontal lines show the value measured by (OGLE, MACHO, MOA) with its 1σ uncertainties.

useful comparison of the predicted optical depth trends with observational data. Since the EROS-2 survey (like all microlensing surveys) was conducted across many fields rather than for a specific LOS, any observed oscillation in τ similar to the prediction will be somewhat smoothed out. However, this effect should not be strong, as the predicted trend is similar for different lines of sight towards the bulge (as shown in Fig. 3.2).

To make the comparison, unpublished EROS-2 data has been supplied by Rich et al. (private communication). They find, from studies with artificial stars, that clump giant fluxes are smeared by $\sim$20% rms, which does not affect their optical depth calculations averaged over the whole clump, but will of course reduce the τ amplitude by smoothing out the predicted oscillation. This flux smearing effect is added to all of the model stars, using a Gaussian with $\sigma = 0.2$. It is found that although the τ amplitude is indeed reduced, the oscillation is still clear, as shown in Fig. 3.10.

$\tau_{\rm EROS}$ is now found as a function of source magnitude, using equation (1.17):

$$\tau = \frac{\pi}{2u_0(\max)} \frac{\sum_{i=1}^{N_{\rm ev}} t_{{\rm E},i}/\epsilon(t_{{\rm E},i})}{\sum_{j=1}^{N_*} T_j}$$

where each event i has a timescale $t_{{\rm E},i}$ and detection efficiency $\epsilon(t_{{\rm E},i})$, each monitored star j is observed for a time T_j, the total numbers of events and stars are $N_{\rm ev}$ and N_*, respectively, and the maximum impact parameter $u_0(\max) = 0.75$ (Hamadache et al. 2006). The uncertainty is also determined by following Hamadache et al. (2006), who added in quadrature a 5% systematic part – due to blending effects – and a larger statistical part, estimated according to Han & Gould (1995):

$$\sigma(\tau) = \tau \frac{\sqrt{\langle t_{\rm E}^2/\epsilon^2 \rangle}}{\langle t_{\rm E}/\epsilon \rangle} \frac{1}{\sqrt{N_{\rm ev}}}. \qquad (3.3)$$

EROS stars were observed in two non-standard bands, $R_{\rm EROS}$ and $B_{\rm EROS}$, where $R_{\rm EROS} = I_{\rm OGLE}$. Hamadache et al. (2006) divided each of their 66 bulge fields into 32 subfields, eliminating from the analysis a total of 46 subfields that did not follow the expected reddening law. For the remaining 2063 subfields (another 3 were also removed), they defined a reddening-free magnitude $R_{\rm EROS} - 1.9\,(B - R)_{\rm EROS}$ (hereafter $RF_{\rm EROS}$).

Fig. 3.11 shows $\tau_{\rm EROS}$ as a function of this reddening-free source apparent magnitude. The observed trend is now compared with the flux-smeared predicted

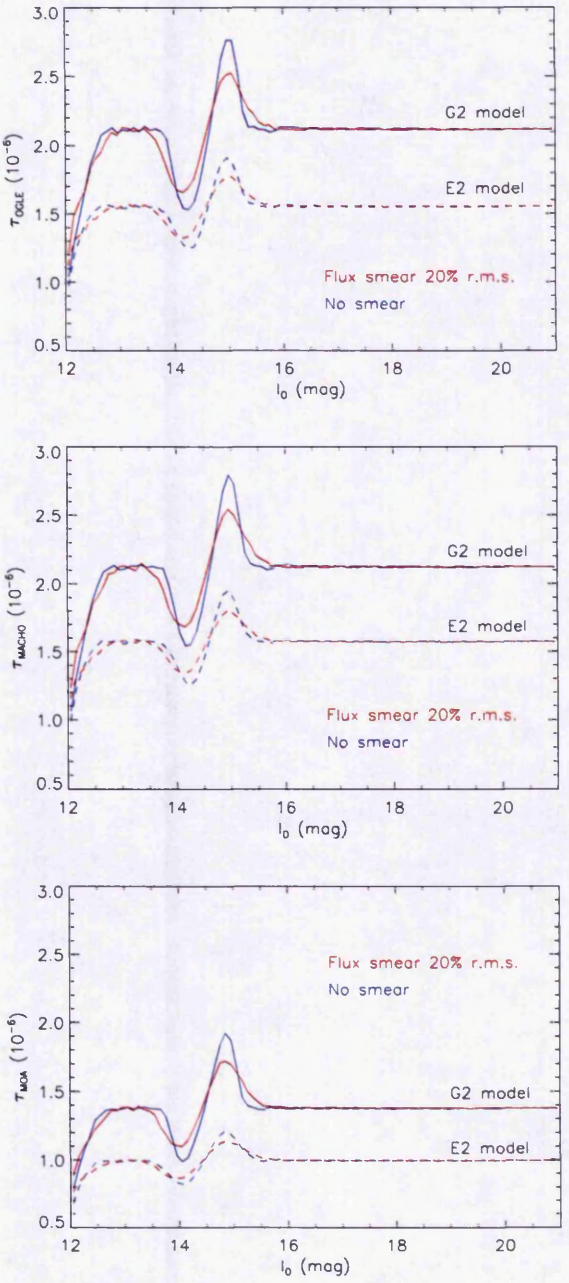

Figure 3.10: (Top, middle, bottom) panel: Expected ($\tau_{\rm OGLE}$, $\tau_{\rm MACHO}$, $\tau_{\rm MOA}$) as a function of source apparent magnitude, with and without stellar flux smearing of 20% rms, as indicated. The curves with no smearing are the same as in Fig. 3.2.

trends, using a χ^2 test, to see if the former is better fitted by an oscillating or constant optical depth.

The offset between the two magnitude scales, $RF_{\rm EROS}$ and I_0, must first be determined. The centres of the RCG clumps are taken as reference points. For the (OGLE, MACHO, MOA) LOS, the Gaussian component shown in Fig. 3.1 peaks at $I_{0,\ \rm clump}$ = (14.75, 14.65, 14.55) $\pm$ 0.05 (for bin widths of 0.1 mag). For the E2 model, the magnitudes are slightly brighter: $I_{0,\ \rm clump}$ = (14.65, 14.55, 14.45) $\pm$ 0.05. For each EROS subfield, Hamadache et al. modelled the stellar density in colour-magnitude space as a power-law plus Gaussian, in order to find the magnitude, $RF_{\rm EROS,\ clump}$, and colour of the clump centre. Fig. 3.11 shows the distribution of $RF_{\rm EROS,\ clump}$ for all the subfields. Due to the many different lines of sight observed by EROS, this distribution is quite broad, spanning the range 12.57–13.92 mag. Hence the magnitude offset is treated as a free parameter in the χ^2 fit, but with limits $12.57 \leq I_{0,\ \rm clump} \leq 13.92$. Since the width of the oscillation and the absolute values of the τ amplitude and $\tau_{\rm flat}$ will also change slightly for each EROS field, three further free parameters are allowed in the fit: the model trend may also be stretched along the magnitude axis, and both shifted and stretched along the τ axis – though not stretched in the former case by more than an arbitrary limit of 50%, since Fig. 3.2 shows that the width of the oscillation does not vary much with direction. Finally, to allow for other slight changes in the shape of the oscillation with direction and bulge model, all six of the predicted trends (three lines of sight, G2 and E2 models) are tested. These χ^2 values are compared with that for a freely-fitted constant optical depth. The results are shown in Table 3.5. Also indicated are the probabilities p that the given values of χ^2 would occur by chance.

An oscillating τ appears to provide a better fit to the data than a constant optical depth. There is a mostly negligible change in χ^2 with direction, and a small preference for the G2 model. Fig. 3.11 shows the best fit oscillation, with the OGLE G2 trend: $I_{0,\ \rm clump}$ is shifted by -1.18 mag, and $\tau_{\rm flat}$ by -0.47×10^{-6}. The curve has been stretched by factors of 1.15 and 1.25 along the magnitude and τ axes, respectively. However, the significance of the χ^2 preference for an oscillating τ, rather than a constant value, is low. A reasonable magnitude binning gives only eight data points. Whereas the oscillating τ fit has four free parameters, thus giving four degrees of freedom (dof), the constant τ fit has of course just one free parameter, and seven dof. Considering p is helpful: taking $p < 0.05$ to be

significant, it appears that only the G2 – and not the E2 – oscillating τ provides a fit that is not significantly discrepant to the data.

So far the EROS trend has been found with correction for extinction. As stated above, any smoothing effects from the survey's multiple lines of sight are not expected to be strong. This assumption can be tested, by removing any such effect with a further correction: τ is found as a function of magnitude *relative to the clump centres.* This method 'lines up' all the clump centres in each subfield. It will also of course remove extinction effects. Therefore τ is plotted as a function of $R_{\rm EROS}$ rather than $RF_{\rm EROS}$, and since $R_{\rm EROS} = I_{\rm OGLE}$, there will be no complications arising from using two different magnitude scales.

Fig. 3.12 shows $\tau_{\rm EROS}$ as a function of $R_{\rm EROS} - R_{\rm EROS,\ clump}$. If the predicted oscillation is present in the data it should now be more pronounced, and so provide a better χ^2 fit than above. This is indeed the case, as shown in Table 3.6. The same free parameters are included in the fit as before, except of course for any shift in magnitude, which is no longer applicable. Hence there are now three free parameters and five dof. The fit to a constant τ is also improved, but an oscillation is still preferred. The best fit oscillation – which is now with the MACHO E2 trend – is shown in Fig. 3.12: $\tau_{\rm flat}$ has been shifted by -0.05×10^{-6}, and the curve has been stretched by factors 1.50 and 1.60 along the magnitude and τ axes, respectively. (Note that the factor of 1.50 is at the (arbitrary) 50% limit. The fits improve with further magnitude stretching, the best possible fit being for a factor 2.50 (MACHO G2 model), with $\chi^2 = 1.44$, but this is well beyond the limit and is ignored). However, with two fewer dof, the χ^2 preference for an oscillation is still of low significance – the constant τ fit is not significantly discrepant to the data.

It is possible that the EROS-2 event detection efficiency may be a function of magnitude. However, it would not be a strong dependance, and any variation would be smooth. It could not therefore hide any real oscillation of τ, or generate a false one (Rich, private communication). It appears that the available data are still insufficient to accurately determine the dependance of the optical depth on source apparent magnitude.

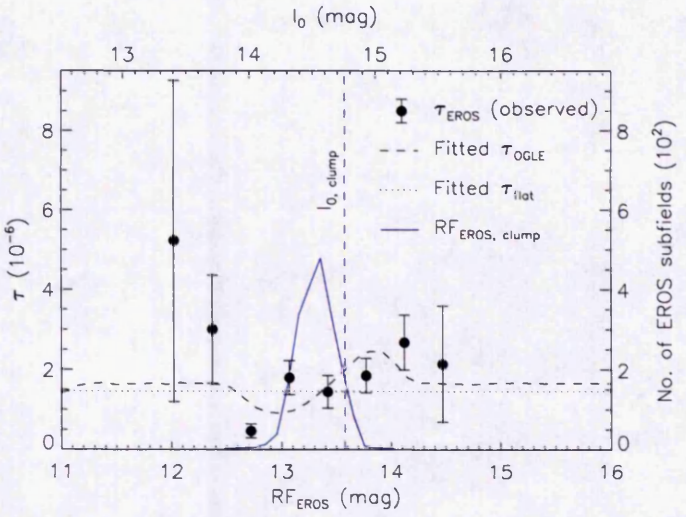

Figure 3.11: Observed $\tau_{\rm EROS}$, and fitted model $\tau_{\rm OGLE}$, as functions of the reddening-free magnitude $RF_{\rm EROS} = R_{\rm EROS} - 1.9\,(B-R)_{\rm EROS}$, and I_0, respectively. The I_0 magnitude scale is stretched, relative to $RF_{\rm EROS}$, by the fitting factor (see text). Also shown are the fitted $\tau_{\rm flat}$, the distribution of clump centres $RF_{\rm EROS,\ clump}$ for the 2063 EROS subfields, and the model clump centre $I_{0,\ \rm clump}$ (see text).

	G2	E2
OGLE	9.44	10.37
MACHO	9.56	10.44
MOA	9.44	10.96
Average	9.48 ($p > 0.05$)	10.59 ($p < 0.05$)
Constant τ	14.15 ($p < 0.05$)	
$\Delta\chi^2$	4.67	3.56

Table 3.5: χ^2 values from fitting the observed $\tau_{\rm EROS}$ as a function of reddening-free magnitude, $RF_{\rm EROS}$, with the predicted (oscillating) trends for different lines of sight and bulge models as indicated, and with a constant optical depth. The probabilities p that the given values of χ^2 would occur by chance are also indicated. An oscillating τ provides a better fit, but at a low significance (see text).

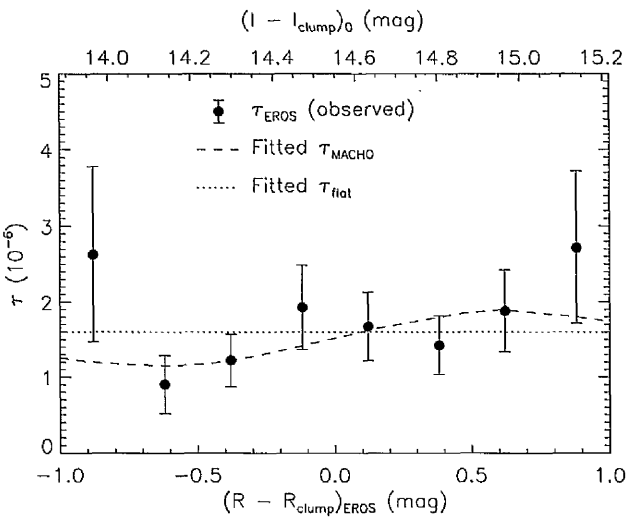

Figure 3.12: Observed $\tau_{\rm EROS}$, and fitted model $\tau_{\rm MACHO}$, as functions of magnitude relative to the clump centre, $R_{\rm EROS} - R_{\rm EROS,\ clump}$ and $I_0 - I_{0,\ \rm clump}$, respectively (see text). The latter magnitude scale is stretched relative to the former by the fitting factor. Also shown is the fitted $\tau_{\rm flat}$.

	G2	E2
OGLE	2.07	1.84
MACHO	1.91	1.83
MOA	1.99	1.93
Average	1.99 ($p > 0.75$)	1.87 ($p > 0.75$)
Constant τ	4.24 ($p > 0.75$)	
$\Delta\chi^2$	2.25	2.37

Table 3.6: χ^2 values from fitting the observed $\tau_{\rm EROS}$ as a function of $R_{\rm EROS} - R_{\rm clump}$ with the predicted (oscillating) trends, for different lines of sight and bulge models as indicated, and with a constant optical depth. The probabilities p that the given values of χ^2 would occur by chance are also indicated. An oscillating τ provides a better fit, but at a low significance (see text).

3.4 Summary and conclusions

It does not appear that the discrepancy in optical depth measurements between the RCG and all-star analyses can be explained by a dependence of the lensing surveys on their flux limits. The model reproduces the OGLE and MACHO values based on RCGs, but underpredicts MOA's all-star value by $\sim 2.4\sigma$. Another potential explanation for the discrepancy is blending. Sumi et al. (2006) found $\sim$38% of OGLE-II events with apparent RCG sources were really due to faint stars blended with a bright companion. However, they also showed that blending has little effect on estimates of τ due to partial cancellation of its different effects, a point also made by Popowski et al. (2005) and Hamadache et al. (2006). Sumi et al. (2006) also state that the DIA method is less sensitive to the systematics of blending in crowded fields. Though it is of course possible that MOA's value may yet be lowered with more data, it is supported by MACHO's earlier DIA value.

τ is expected to be generally constant as a function of source apparent magnitude for $I_0 \gtrsim 13.0$, except in the range $13.5 \lesssim I_0 \lesssim 15.5$, where many RCGs are detected. These stars dominate the source counts at such magnitudes, and show a strong correlation between distance and apparent magnitude, causing a significant oscillation in τ. The amplitude of this oscillation is found to decrease with increasing bar angle, providing a potential constraint on $\theta_{\rm bar}$. A further constraint comes from a similar dependance of τ with $\theta_{\rm bar}$: combining the predicted trends with the measured values provides 1σ upper limits, which rule out the large bar angles reported by GLIMPSE and EROS.

From the EROS-2 survey, $\tau_{\rm EROS}$ has been found as a function of source apparent magnitude. The predicted oscillation is not only consistent with the observed trend, but provides a better χ^2 fit than a constant optical depth, though the significance of this preference is low due to insufficient data. However, with ongoing surveys detecting increasing numbers of RCG events (and $\sim$500 yr^{-1} of all kinds), it should soon be possible to make a more useful and definite comparison.

References

Afonso C. et al., 2003, A&A, 404, 145

Alcock C. et al., 2000, ApJ, 541, 734

Benjamin R.A. et al., 2005, ApJ, 630, L149

Dwek E. et al., 1995, ApJ, 445, 716

Gerhard O., 2002, in Da Costa G.S., Sadler E.M., eds., ASP Conf. Ser. Vol. 273, The Dynamics, Structure & History of Galaxies: A Workshop in Honour of Professor Ken Freeman, Astron. Soc. Pac., San Francisco, p. 73

Hamadache C. et al., 2006, A&A, 454, 185

Han C., Gould A., 1995, ApJ, 449, 521

Han C., Gould A., 2003, ApJ, 592, 172

Popowski P. et al., 2005, ApJ, 631, 879

Stanek K.Z., 1995, ApJ, 441, L29

Stanek K.Z., Mateo M., Udalski A., Szymański M., Kałużny J., Kubiak M., 1994, ApJ, 429, L73

Sumi T., 2004, MNRAS, 349, 193

Sumi T. et al., 2003, ApJ, 591, 204

Sumi T. et al., 2006, ApJ, 636, 240

Thomas C.L. et al., 2005, ApJ, 631, 906

Udalski A. et al., 2002, Acta Astron., 52, 217

Wood A., 2006, MNRAS, in prep.

Woźniak P.R., Udalski A., Szymański M., Kubiak M., Pietrzyński G., Soszyński I., Żebruń K., 2001, Acta Astron., 51, 175

Zheng Z., Flynn C., Gould A., Bahcall J.N., Salim S., 2001, ApJ, 555, 393

Chapter 4

Modelling proper motions and dispersions

This chapter examines the stellar proper motions and velocity dispersions in the Galactic bulge. Building on a relatively simple kinematic model, we see how each stage of development brings the predicted trends closer to those observed in several MACHO survey fields. The sensitivity of event timescale predictions to the different kinematic assumptions is then considered.

4.1 Introduction

The parameters of the bulge at the centre of our own Galaxy are still not well understood. Numerous attempts have been made to develop self-consistent dynamical models (e.g., Häfner et al. 2000; Bissantz, Debattista & Gerhard 2004), but they have been hampered by limited good observational data, and few lines of sight, with which to compare their predictions.

Microlensing surveys of the Galactic bulge, such as OGLE (Udalski et al., 1992) and MACHO (Alcock et al., 1993), involve prolonged monitoring of dozens of densely-populated stellar fields. A few thousand microlensing events have now been found, and high-resolution follow-up observations of many of these have been made with the *Hubble Space Telescope* (*HST*). Kozłowski et al. (2006, hereafter K06) used second-epoch observations of 35 bulge fields – centred around microlensing events seen by MACHO – to measure high-precision proper motions μ_l and μ_b of 15,863 stars. They then determined the stellar proper motion dispersions in the Galactic latitude (l) and longitude (b) directions, σ_l and σ_b, respectively, as functions of both l and b. From simple straight-line fits, they found small but clearly present gradients. The anisotropy ratio σ_l/σ_b also showed weak trends with both l and b. Comparing their results with previous similar studies – an analysis of two *HST* fields by Kuijken & Rich (2002), and the proper motion catalogue of Sumi et al. (2004), produced from the OGLE-II database – revealed good agreements.

The clearest trends found by K06 were increases in σ_l and σ_l/σ_b towards the Galactic plane, and, within the plane, an increase in σ_b and decrease in σ_l/σ_b towards the Galactic centre. K06 speculated on reasons for these slopes, but there are no clearly convincing explanations. As K06 stated, we now have new constraints on dynamical inner Galactic models, and dramatically improved number statistics, but a detailed modelling of the measurements was beyond the scope of their study.

Binney (2005) discussed the progress of three sophisticated dynamical modelling techniques with regard to major observational advances expected from the *Gaia* space mission. However, it is useful to consider what can be achieved with simpler, less computationally expensive kinematic models. Such a model was used in chapter 2 where predictions of microlensing optical depths and event timescale distributions were made, in good agreement with the latest observations. Furthermore, with a simpler model it is somewhat easier to test, illustrate

and understand the relative effects of various different dynamical assumptions about the Galactic bulge.

In this chapter an attempt is made to reproduce the proper motion and dispersion trends observed by K06, with Monte Carlo simulations using the Galactic model from chapter 2. The kinematic part of the model is then developed, with analysis of the effect of each modification. The initial model is described in §4.2. The calculations, model developement and results are discussed in §4.3 and §4.4, including a look at the effects of the model development on the predictions of event timescales. A summary and conclusions are given in §4.5.

4.2 Initial model

4.2.1 Mass model

The mass models and parameters of the Galactic bulge (bar) and disc are described in detail in chapter 2. They are based on those of Han & Gould (2003), who empirically normalised the G2 bulge model of Dwek et al. (1995, table 1) with *HST* star counts, and extended the local disc model of Zheng et al. (2001) to the whole disc.

4.2.2 Kinematic model

The initial kinematic model is also described in detail in chapter 2, but for clarity and completeness the essential details are repeated here. Stellar velocity components in l and b are given by equation (2.5):

$$v_l = v_{\rm rot} + v_{{\rm rand},l}, \qquad v_b = v_{{\rm rand},b},$$

where $v_{\rm rot}$, the longitudinal component of the rotation velocity, and $v_{\rm rand}$, the random velocity, are from Han & Gould (1995): for the disc $v_{\rm rot} = 220$ kms^{-1}, and for the bar $v_{\rm rot}$ is given by projecting $v_{\rm max} = 100$ kms^{-1} across the line of sight (LOS) according to equation (2.6):

$$\begin{aligned} v_{\rm rot} &= v_{\rm max}\left(\frac{x}{1\ {\rm kpc}}\right) && (R < 1\ {\rm kpc},\ \text{solid body rotation}), \\ v_{\rm rot} &= v_{\rm max}\left(\frac{x}{R}\right) && (R \geq 1\ {\rm kpc},\ \text{flat rotation}), \end{aligned}$$

where $R = (x^2 + y^2)^{1/2}$, and the coordinates (x, y, z) have their origin at the Galactic centre, with the x and z axes pointing towards the Earth and the north Galactic pole (NGP), respectively. The observer velocity is assumed to follow the Galactic disc rotation, adjusted for the Sun's peculiar motion. The random velocity components $v_{\mathrm{rand},l}$ and $v_{\mathrm{rand},b}$ are assumed to have Gaussian distributions, with dispersions taken from Han & Gould (1995): for the disc, $\sigma_{l,b} = (30, 20)$ kms^{-1}; for the bar, Han & Gould calculated dispersions from the tensor virial theorem (TVT). Adjusting their values to the G2 bar angle $\theta_{\mathrm{bar}} = 13.4°$ gives $\sigma_{x,y,z} = (110, 78.4, 65.1)$ kms^{-1}, with a normalisation to the observed mean LOS dispersion of $\sim$110 kms^{-1}.

4.3 Dispersion and covariance calculations

Model stars are generated along the lines of sight to each field analysed by K06, assigning random velocities according to the model described above. The average proper motion dispersions σ_l and σ_b are then found for each field. Following K06, the anistropy ratio σ_l/σ_b and the normalised covariance term $\mathrm{C}_{lb} = \sigma_{lb}/(\sigma_l\sigma_b)$ are also calculated.

4.4 Model development, results and discussion

4.4.1 Initial model

Fig. 4.1 shows the observed trends of σ_l, σ_b and the ratio σ_l/σ_b with l and b, together with the predictions – these are shown for model bulge stars and all stars, since the stellar samples analysed by K06 were contaminated with stars from the disc population. The individual measurements and predictions for each field are shown with data points, and the trends are indicated with the solid lines. Where no clear trend was observed, the weighted average is shown instead with a dashed line. The predicted trends are compared with the data using a χ^2 test, the results of which are given in Table 4.1. For comparison, Table 4.2 shows the results of a similar χ^2 test using the fitted trends or weighted average trends, as appropriate, given by K06. In each case there are 35 data points, with two free parameters for a simple linear fit, and none where weighted averages are used. Hence there are 33 and 35 degrees of freedom, respectively.

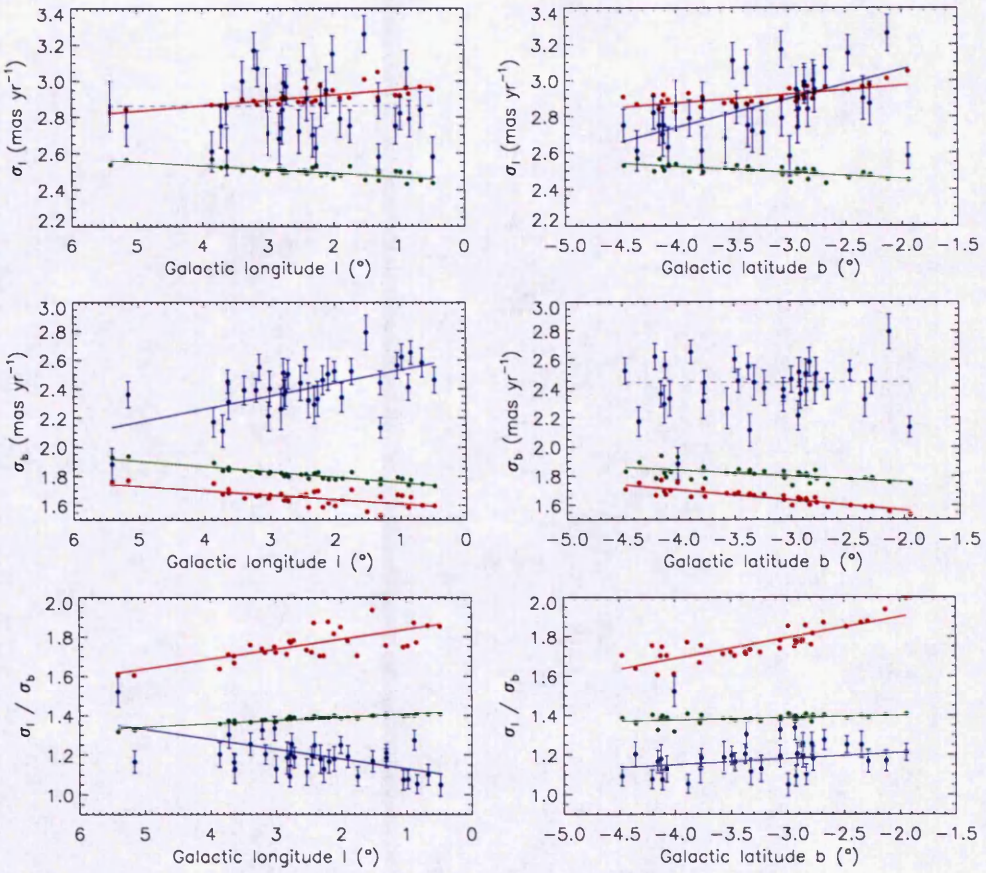

Figure 4.1: Proper motion dispersions σ_l (top panels), σ_b (middle panels), and the anistropy ratio σ_l/σ_b (bottom panels), as functions of Galactic latitude (l) and longitude (b), for the fields analysed by K06. The (green, red) data points are initial model predictions for (bar, all) stars. The blue data points show the observed values. Linear trends and weighted averages are indicated by the solid and dashed lines, respectively (see text).

	l	b
σ_l	12.15, 51.98	10.61, 52.83
σ_b	220.70, 145.84	218.53, 142.16
σ_l/σ_b	225.92, 31.43	220.26, 29.65

Table 4.1: χ^2 values from fitting the predicted dispersion trends, as functions of l and b, to the data given by K06. The pairs of numbers are for (all, bar) stars.

	l	b
σ_l	10.44	9.70
σ_b	7.41	10.58
σ_l/σ_b	3.74	4.74

Table 4.2: χ^2 values from fitting the dispersion trends/weighted averages given by K06, as functions of l and b, to their data.

It is clear that including disc stars increases the overall σ_l, but decreases the overall σ_b. This effect is explained in §4.4.11. By inspection, there is quite good agreement between the predictions (for all stars) and the observations of σ_l, for both its trends and values, although the observed trend with b is noticeably steeper. However, the model otherwise matches the data with little success. Trends, field-by-field values or both are significantly different. The simple initial kinematic model must therefore be developed and made more realistic. The following sections §4.4.2 – §4.4.7 describe the stages of this development, and how they affect the predictions.

4.4.2 Using the tensor virial theorm

The first step is to re-examine the bulge velocity dispersions. There are two motivations for this, as mentioned in §2.2.4. Firstly, the dispersions were calculated for the G2 model from the TVT by Han & Gould (1995), but their calculation was of course performed without the normalisation of G2 by star counts that was applied by Han & Gould (2003), and is included in the model. Secondly, the calculation contained a mistake as pointed out by Blum (1995). A derivation of the TVT is given by Binney & Tremaine (1987). It incorporates the following four tensors:

The potential energy tensor $\mathbf{W}$ of the bulge is given by

$$W_{jk} = -\frac{1}{2}G \int \int \rho(\mathbf{x})\rho(\mathbf{x}') \frac{(x'_j - x_j)(x'_k - x_k)}{|\mathbf{x}' - \mathbf{x}|^3} d^3\mathbf{x}' d^3\mathbf{x}, \tag{4.1}$$

where x_j and x_k are a particle's coordinates in any two perpendicular directions (x, y or z), the prime denotes a second particle, and $\mathbf{x}$ and $\mathbf{x}'$ are dummy variables of integration. The total potential energy is given by trace ($\mathbf{W}$). The kinetic

energy tensor $\mathbf{K}$, given by

$$K_{jk} = \frac{1}{2} \int \rho \overline{v_j v_k} d^3\mathbf{x}, \tag{4.2}$$

can be split up into the contributions from ordered and random motion:

$$K_{jk} = T_{jk} + \frac{1}{2}\Pi_{jk}, \tag{4.3}$$

where

$$T_{jk} = \frac{1}{2} \int \rho \overline{v}_j \overline{v}_k d^3\mathbf{x} \quad \text{and} \quad \Pi_{jk} = \int \rho \sigma_{jk}^2 d^3\mathbf{x}. \tag{4.4}$$

The total kinetic energy is given by trace $(\mathbf{T}) + \frac{1}{2}$ trace $(\mathbf{\Pi})$. We can express Π_{jk} in terms of the total bulge mass M as follows:

$$\Pi_{jk} = \int \rho \sigma_{jk}^2 d^3\mathbf{x} = \overline{\sigma^2}_{jk} \int \rho d^3\mathbf{x} = \overline{\sigma^2}_{jk} M. \tag{4.5}$$

Finally we have the moment of inertia tensor $\mathbf{I}$, given by

$$I_{jk} = \int \rho x_j x_k d^3\mathbf{x}. \tag{4.6}$$

The TVT then states that

$$\frac{1}{2}\frac{dI_{jk}^2}{dt^2} = 2T_{jk} + \Pi_{jk} + W_{jk}. \tag{4.7}$$

For a system in a steady state, such as the Galactic bulge, $\ddot{\mathbf{I}} = 0$. Therefore, using equation (4.5), we can rearrange equation (4.7) to give a simple expression for the velocity dispersions:

$$\overline{\sigma^2}_{jk} = \frac{-(W_{jk} + 2T_{jk})}{M}. \tag{4.8}$$

The dispersions required here are the diagonal terms σ_{xx}, σ_{yy} and σ_{zz}. First, as a check, the numerical integration of equation (4.1) is performed for a Plummer potential (see e.g. Binney & Tremaine 1987), since in this case $\mathbf{W}$ can also be easily found analytically (Binney & Tremaine 1987, p. 68). As expected, both methods give the same result.

The model gives a total mass $M = 9.2 \times 10^9$ $M_\odot$. This is reasonably close to the value $M = 1.3 \times 10^{10}$ $M_\odot$ derived photometrically by Dwek et al. (1995)

(for a Salpeter initial mass function extended down to 0.1 $M_\odot$), but only half that calculated by Han & Gould (1995): $M = 1.8 \times 10^{10}$ $M_\odot$. The new model dispersions are $\sigma_{x',y',z'} = (81.1, 52.8, 51.8)$ kms^{-1}, where the coordinates (x', y', z') have their origin at the Galactic centre and the axes x' and z' point along the longest (major) bulge axis, and towards the NGP, respectively. The projected velocity dispersions are given by

$$\begin{aligned} \sigma_x^2 &= \sigma_{x'}^2 \cos^2\theta + \sigma_{y'}^2 \sin^2\theta, \\ \sigma_y^2 &= \sigma_{x'}^2 \sin^2\theta + \sigma_{y'}^2 \cos^2\theta, \\ \sigma_z &= \sigma_{z'}. \end{aligned} \tag{4.9}$$

For $\theta_{\rm bar} = 13.4°$, normalising to the observed mean LOS dispersion of $\sim$110 kms^{-1} gives $\sigma_{x,y,z} = (110, 75.4, 71.4)$ kms^{-1}. Compared to the dispersions used so far, $\sigma_{x,y,z} = (110, 78.4, 65.1)$ kms^{-1}, there is only a small decrease in σ_y, but a larger increase in σ_z.

Fig. 4.2 shows the resulting predicted trends. We see that the slopes are not significantly affected by the changes to the dispersions, but as expected there is a small decrease in σ_l, and a slightly larger increase in σ_b. This moves the predicted ratio σ_l/σ_b closer to the observed values, but the overall agreement with the data is still poor. The χ^2 test results are given in Table 4.3. (For σ_l as a function of b, $\chi^2 = 9.33$. This is lower than the corresponding value in Table 4.2, 9.70, hence it appears in this case that K06 did not actually find the best-fit trend. However, given the uncertainties in the fit parameters, this difference is small).

4.4.3 Variable σ_z

The bulge velocity dispersions calculated from the TVT are average values for the whole bar. Applying these averages across the bar is, though, somewhat unrealistic. σ_z in particular will vary with the radial distance R from the centre. Since

$$\sigma_z^2 \propto z_0^2 \rho_0 \propto \Sigma_0, \tag{4.10}$$

where ρ_0 is the central density, z_0 is the scale height and Σ_0 is the central surface density (Binney & Tremaine 1987, p. 282), we can express σ_z as a function of R:

$$\sigma_{z,R} = \sigma_{z,0} \left(\frac{\Sigma_{0,R}}{\Sigma_{0,0}} \right)^{1/2}. \tag{4.11}$$

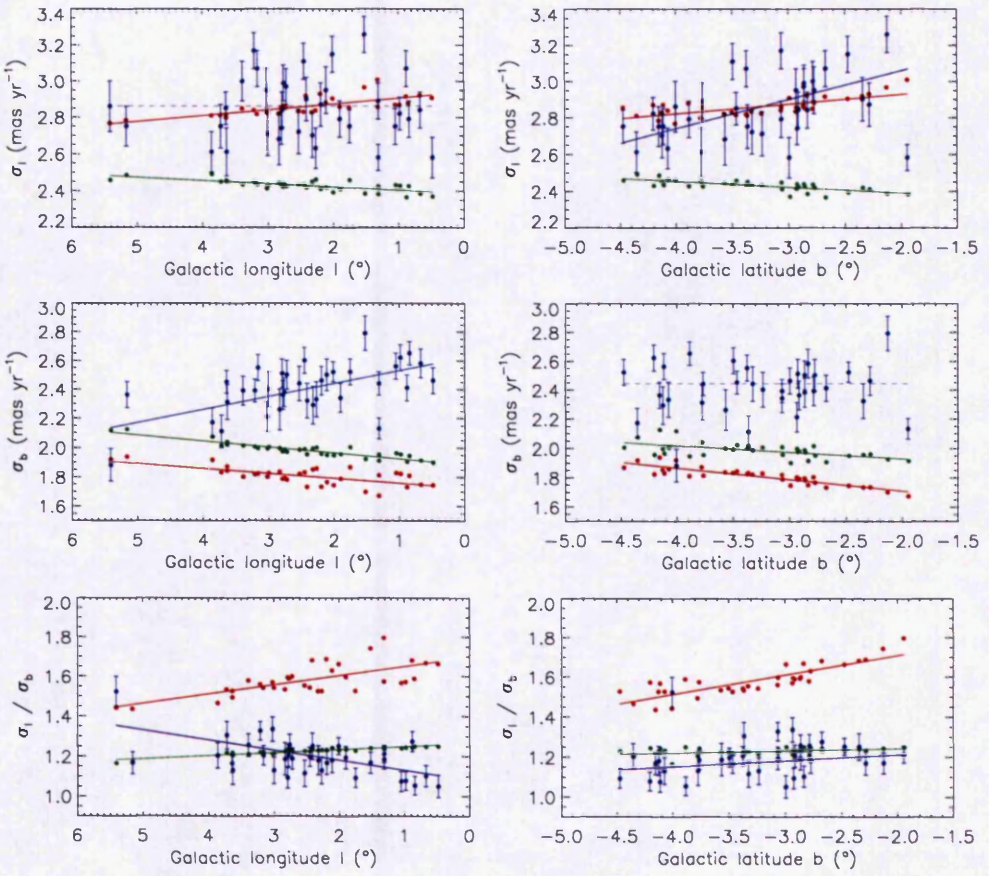

Figure 4.2: Trends of the dispersions σ_l, σ_b, and the anistropy ratio σ_l/σ_b with l and b – same as Fig. 4.1, but with model dispersions calculated from the TVT (see text).

	l	b
σ_l	10.97, 70.55	9.33, 71.34
σ_b	144.84, 81.09	142.61, 77.20
σ_l/σ_b	113.01, 7.23	108.07, 5.76

Table 4.3: χ^2 values from fitting the predicted dispersion trends to the data – same as Table 4.1, but with model dispersions calculated from the TVT.

We can then integrate equation (4.11) over the bulge to find the central velocity dispersion $\sigma_{z,0}$ necessary to give an average $\sigma_z = 71.4$ kms^{-1}. This calculation yields $\sigma_{z,0} = 108$ kms^{-1}.

With σ_z now a function of R in the model, there is a dramatic improvement in agreement between the predictions and data for σ_b, as shown in Fig. 4.3 and Table 4.4 (σ_l is of course unaffected). The predicted values have risen sufficiently to be consistent with many of the observed data points. The trend with b has become flatter, and is fairly consistent with the lack of any observed trend. The slope with l has changed from negative to positive, although it is still much flatter than the observed positive slope. As a result, the predicted anisotropy ratio also improves its match to the observed trends with both l and b.

Note that, since the average σ_z has not changed, the velocity dispersions should still satisfy the TVT. However, with the following modifications to the model in this chapter, no effort is made to ensure the TVT remains satisfied.

4.4.4 Solid body rotation in the inner disc

So far the bulge has been assumed to rotate as a solid body for $R < 1$ kpc, but the disc has been given an entirely flat rotation curve. In fact the Galactic rotation curve is poorly measured for $R \lesssim 2$ kpc (see e.g. Merrifield 1992). Hence solid body rotation is now assumed in the model disc for $R < 1.5$ kpc. The projected disc velocity is calculated in the same way as for the bulge (see equation 2.6).

With disc stars now moving at slower speeds for $R < 1.5$ kpc, the average difference between the velocities of bulge and disc stars in this region will be smaller. Hence σ_l (for all stars) should be reduced. This effect is clearly seen in Fig. 4.4. The slopes of σ_l also change, moving from small positive gradients to flat or slightly negative. These changes mean that while the predicted σ_l trends now show a poorer match to the observations, the anisotropy ratio trends are in good agreement. These changes are reflected in the χ^2 test results (Table 4.5).

4.4.5 Gradient in the bulge rotation

The most striking difference now between the predicted trends and those observed is that of σ_l with b. This is the steepest of the measured slopes, yet the model gives a flat distribution. K06 suggested the rise of σ_l towards the plane is likely due to increasing disc contamination and/or a possible gradient in the bulge rotation

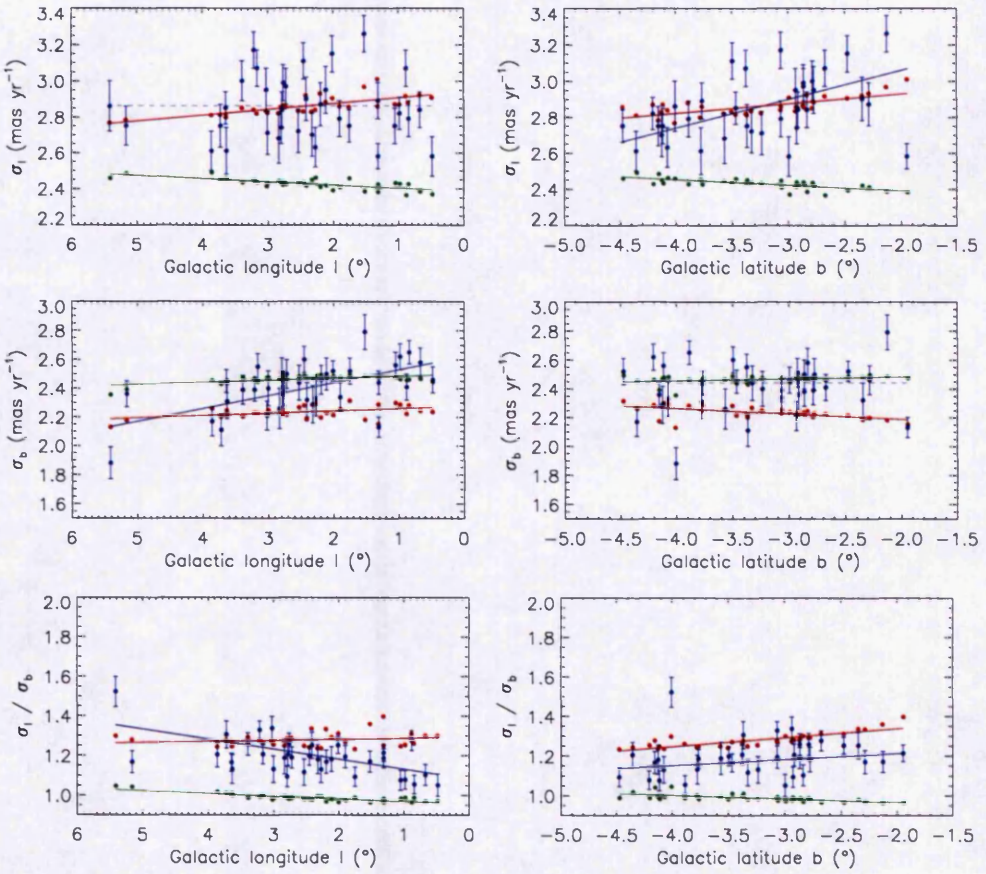

Figure 4.3: Trends of the dispersions σ_l, σ_b, and the anistropy ratio σ_l/σ_b with l and b – same as Fig. 4.2, but with the model σ_z varying as a function of radius (see text).

	l	b
σ_l	10.97, 70.55	9.33, 71.34
σ_b	19.91, 10.30	21.49, 11.27
σ_l/σ_b	10.95, 30.04	10.30, 31.10

Table 4.4: χ^2 values from fitting the predicted dispersion trends to the data – same as Table 4.3, but with the model σ_z varying as a function of radius.

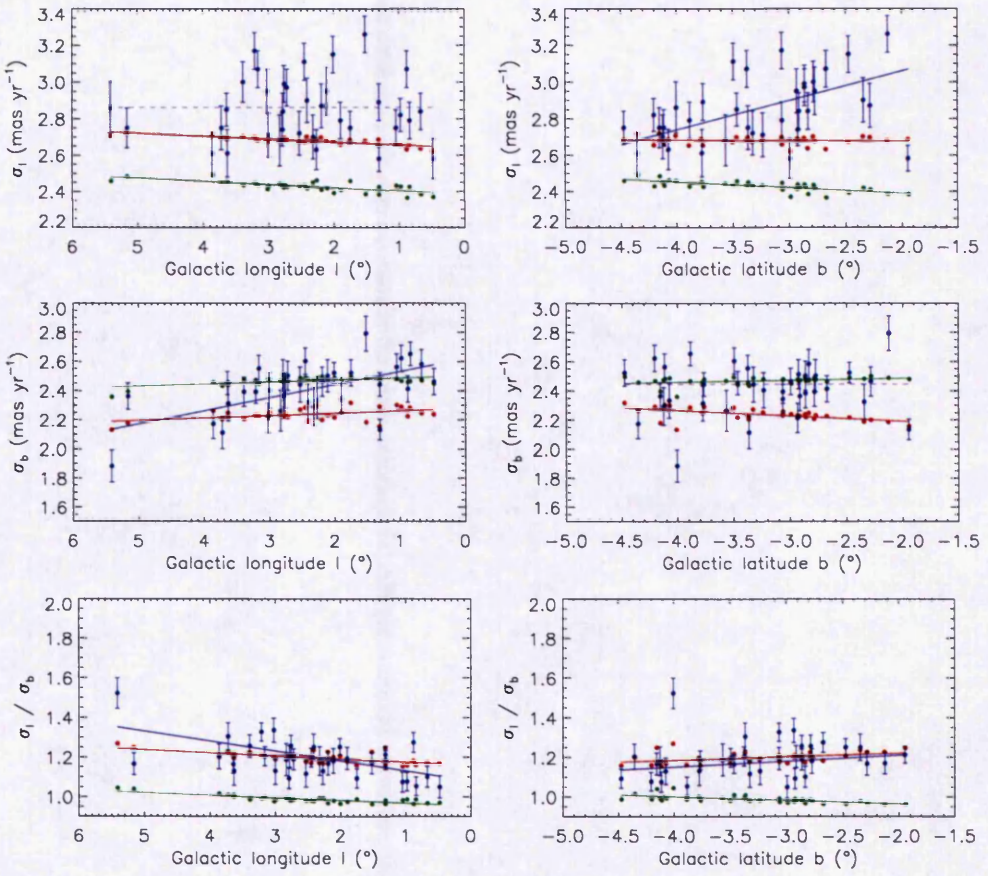

Figure 4.4: Trends of the dispersions σ_l, σ_b, and the anistropy ratio σ_l/σ_b with l and b – same as Fig. 4.3, but with solid body rotation in the model inner disc (see text).

	l	b
σ_l	20.10, 70.55	19.98, 71.34
σ_b	19.91, 10.30	21.49, 11.27
σ_l/σ_b	4.17, 30.04	4.81, 31.10

Table 4.5: χ^2 values from fitting the predicted dispersion trends to the data – same as Table 4.4, but with solid body rotation in the model inner disc.

speed. Fig. 4.4 does not support the former proposal, as the predicted trends with or without disc stars are the same.

However, the bulge rotation speed may well be a function of $|b|$, and such a dependence is now added to the model. As with the previous modifications, a simple function is adopted to illustrate the nature of any resulting effect. So far $v_{\max} = 100$ kms^{-1} has been used. Now $v_{\max}$ is taken to vary linearly with z, from 150 kms^{-1} in the plane to zero at $|z| = 2$ kpc. At this height the mass density is negligible: the z scale height in the G2 model is 0.405 kpc. On the z axis, 2 kpc equates to an angle $b \sim 14°$. The rotational velocity is projected across the LOS as before according to equation (2.6).

Fig. 4.5 shows a significant effect on σ_l. It increases in value, and most importantly shows a clear rise towards the plane, in agreement with the observations – Table 4.6 shows that χ^2 has approximately halved for all stars. Both these effects on σ_l can be easily explained: for any given value of l or b, there is now a greater range of possible stellar velocities, and hence an increase in the dispersions. Moving towards the plane, stars on the near and far sides of the bulge are travelling at greater speeds across the LOS, in opposite directions, thus increasing σ_l.

4.4.6 Streaming motions

One final extra component of stellar velocities is now considered. In addition to the rotational motions already described, some previous studies have considered streaming motions parallel to the major axis of the bar (e.g. Mao & Paczyński 2002). This is added to the model, with bulge stars moving parallel to the x' axis in the same direction as their rotational motion. A large constant velocity of 100 kms^{-1} is initially assumed, to ensure any resulting effect is clearly seen. Fig. 4.6 shows that adding streaming motions significantly worsens the model's agreement with the observations. σ_l now rises as l moves towards the centre. As a function of b the trend is unchanged, but σ_l has increased in value and now shows a poorer match to the data points – Table 4.7 shows that χ^2 has significantly increased. Therefore such streaming motions are not retained in the model. Hereafter, the *final model* refers to the kinematic model including the dispersions $\sigma_{x,y,z}$ recalculated from the TVT, variable σ_z, solid body disc rotation for $R < 1.5$ kpc, and a gradient in the bulge rotation.

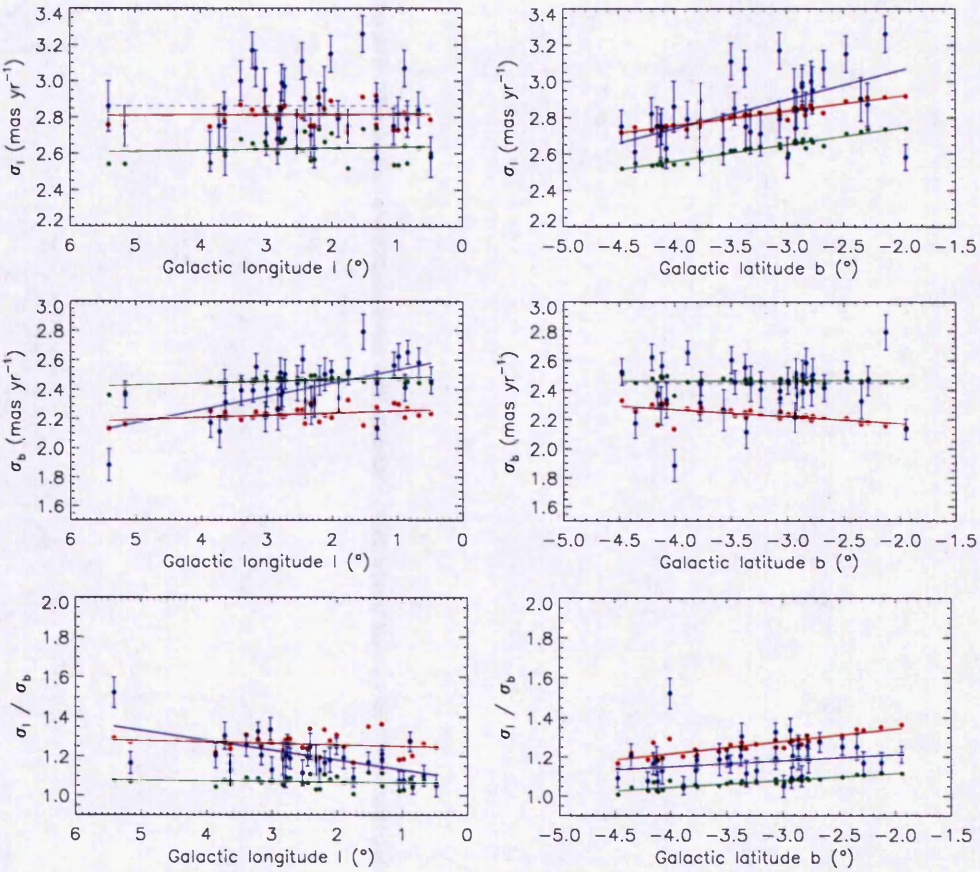

Figure 4.5: Trends of the dispersions σ_l, σ_b, and the anistropy ratio σ_l/σ_b with l and b – same as Fig. 4.4, but with a gradient in the model $v_{\max}$ (see text).

	l	b
σ_l	10.80, 27.40	9.41, 25.82
σ_b	20.89, 10.19	22.57, 11.04
σ_l/σ_b	8.27, 13.60	8.82, 13.31

Table 4.6: χ^2 values from fitting the predicted dispersion trends to the data – same as Table 4.5, but with a gradient in the model $v_{\max}$.

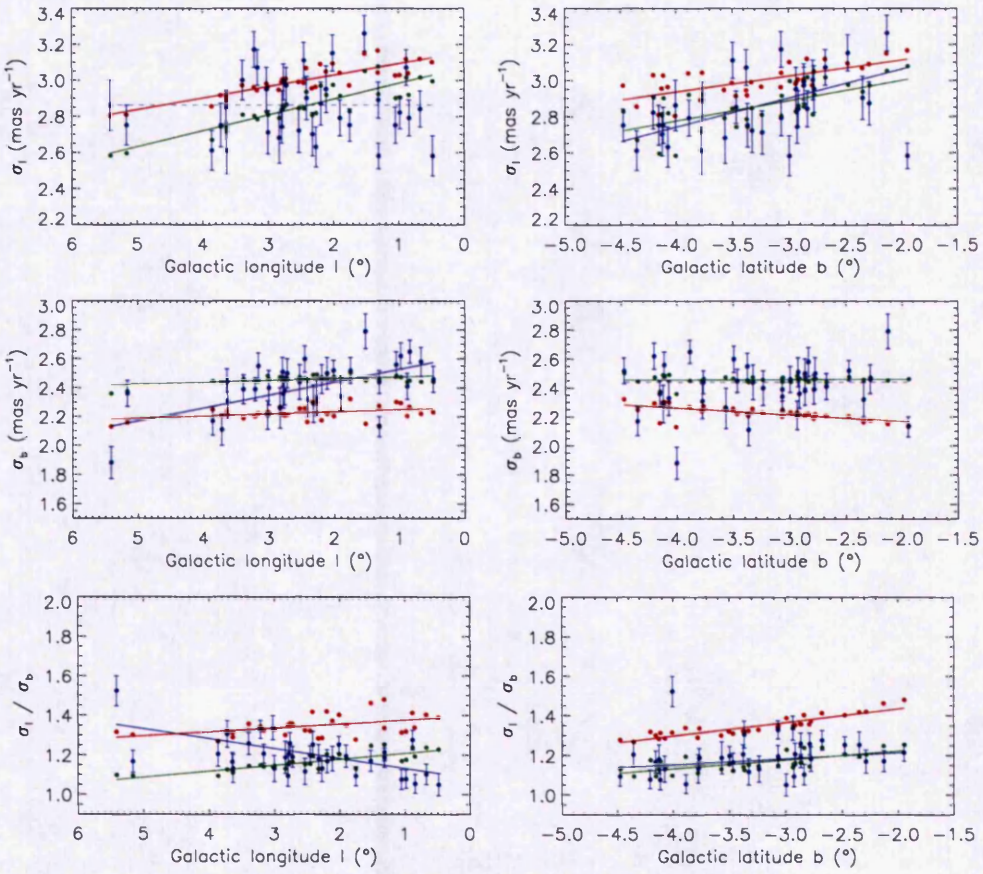

Figure 4.6: Trends of the dispersions σ_l, σ_b, and the anistropy ratio σ_l/σ_b with l and b – same as Fig. 4.5, but with model bar streaming motions (see text).

	l	b
σ_l	20.07, 13.90	16.54, 9.08
σ_b	20.95, 10.14	22.66, 11.01
σ_l/σ_b	23.25, 8.06	21.52, 4.98

Table 4.7: χ^2 values from fitting the predicted dispersion trends to the data – same as Table 4.6, but with model bar streaming motions.

4.4.7 Magnitude cuts

There is one more simple adjustment that can be made to the model, which is to simulate the stellar magnitude limits of the observations. K06 used only stars in the magnitude range $18.0 < I < 21.5$ to trace the kinematic parameters of the bulge[1], but stated that their results were insensitive to the details of the magnitude cuts – a point also noted by Kuijken & Rich (2002). Using the mass-M_I relation of Kroupa & Tout (1997), only stars in this magnitude range are selected. Fig. 4.7 shows that the model predictions are also quite insensitive to these magnitude cuts. The trends are unchanged, but the dispersions are slightly increased. This is explained in §4.4.10. Table 4.8 shows a small overall reduction in χ^2. Note also that, for each of the χ^2 values given for all stars, the probability such a value would occur by chance is now > 0.99.

4.4.8 χ^2 reduction

The improvement in the model's reproduction of the observed dispersion trends has been reflected in the χ^2 tests. Table 4.9 shows the reduction in the χ^2 values. Those given in Table 4.1 (initial model), for all stars, are compared with the corresponding values in Table 4.8 (final model with magnitude cuts). This comparison is most usefully done with respect to the χ^2 values of the best-fit trends or weighted averages (as appropriate) given by K06. Hence the χ^2 values in Table 4.9 are expressed as percentages of those in Table 4.2. For the σ_l trends, χ^2 was initially quite close to that of the K06 trend, and there is a small reduction after the model development. For the σ_b trends, the reduction in χ^2 is of a factor $\sim$10. This causes a large reduction in χ^2 for the trends of the anisotropy ratio, of a factor $\sim$25.

4.4.9 Covariance

K06 found that their estimates of C_{lb} were all negative and scattered uniformly in the range $-0.20 < C_{lb} < -0.02$, but stated the expected covariance was only $C_{lb} \sim 0.02$. They ruled out any observational biases, and concluded there must be a correlation between μ_l and μ_b. This implies a significant tilt of the bulge velocity ellipsoid with respect to the Galactic plane.

[1]This stellar sample is dominated by the bulge main-sequence population near the turn-off point.

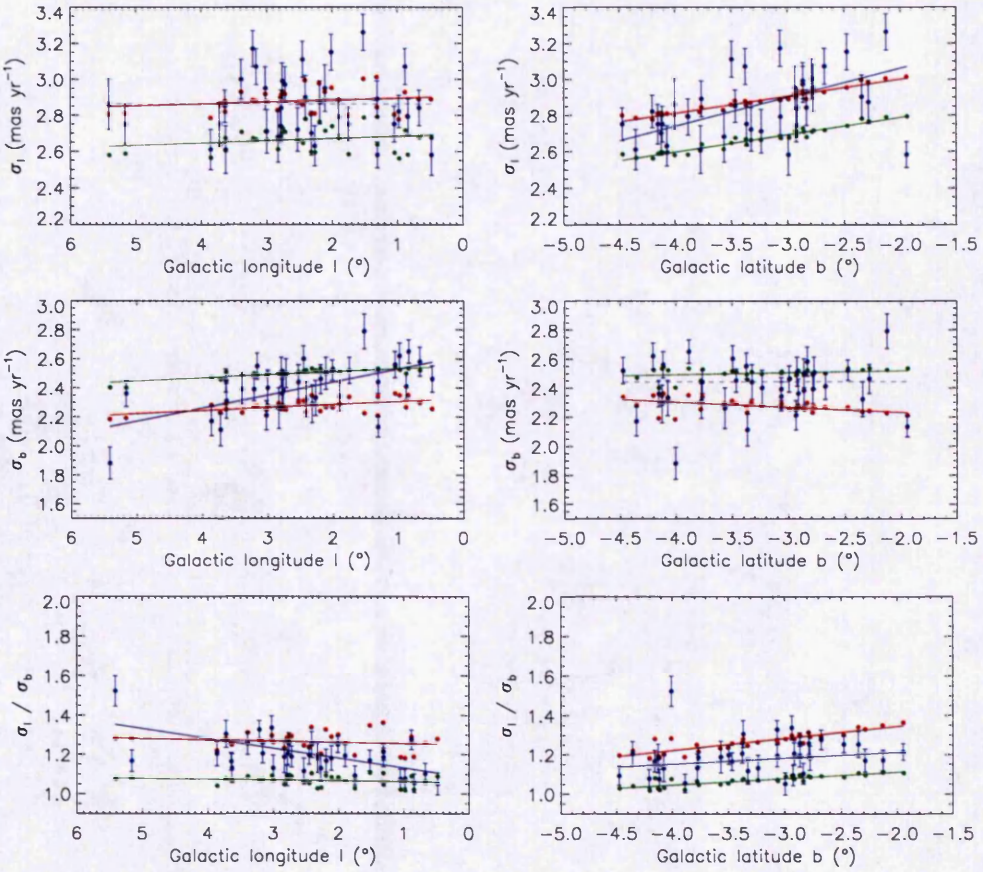

Figure 4.7: Trends of the dispersions σ_l, σ_b, and the anistropy ratio σ_l/σ_b with l and b – same as Fig. 4.5, but with model magnitude cuts (see text).

	l	b
σ_l	10.75, 21.97	9.32, 20.40
σ_b	15.20, 11.70	17.03, 13.04
σ_l/σ_b	8.45, 13.84	8.91, 13.61

Table 4.8: χ^2 values from fitting the predicted dispersion trends to the data – same as Table 4.6, but with model magnitude cuts.

	l	b
σ_l	116.4, 103.0	109.4, 96.1
σ_b	2978.4, 205.1	2065.5, 161.0
σ_l/σ_b	6040.6, 225.9	4646.8, 188.0

Table 4.9: The reduction in χ^2 values after development of the model (see text). The pairs of numbers are for the initial model, and for the final model with magnitude cuts.

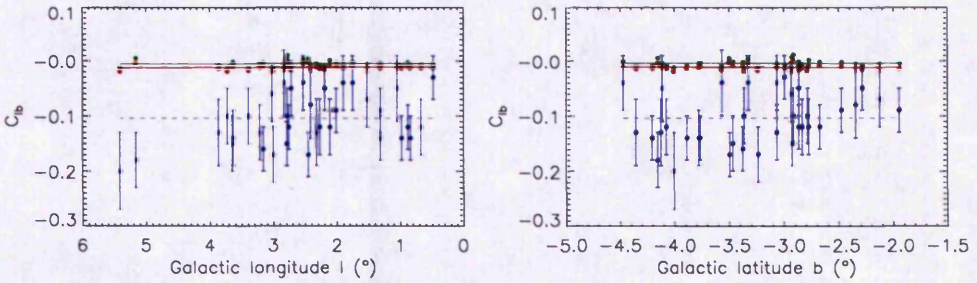

Figure 4.8: (Left, right) panel: Covariance term C_{lb} as a function of (l, b). The (green, red) data points are predictions for (bar, all) stars. The blue data points show the observed values. Linear trends and weighted averages are indicated by the solid and dashed lines, respectively.

Fig. 4.8 shows the observed and predicted covariances. The model predicts $C_{lb} \sim 0.01$. Such a small value is to be expected given that the model treats motions in l and b independently. Tilting the bulge velocity ellipsoid is beyond the scope of the simple kinematic model presented here.

4.4.10 Proper motions and dispersions as functions of distance

Kuijken & Rich (2002) devised an approximate distance measure,

$$M* = I - 2(V - I), \tag{4.12}$$

chosen to remove the slope of the main sequence in the colour-magnitude diagram. K06 found the average proper motions and dispersions as functions of $M*$, towards Baade's window (BW), and their plots are given in Fig. 4.9.

Fig. 4.10 shows the predicted $\langle \mu_l \rangle$ and $\langle \mu_b \rangle$ as functions of absolute distance towards BW, for the final model. Of the modifications made to the initial model,

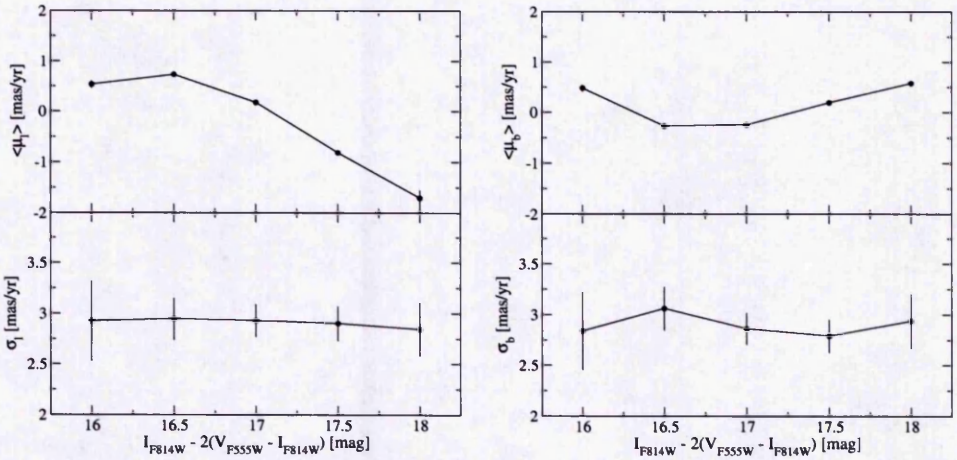

Figure 4.9: Observed average proper motions and dispersions of stars towards BW, against an approximate distance measure $M*$ (see text), from K06 (fig. 7).

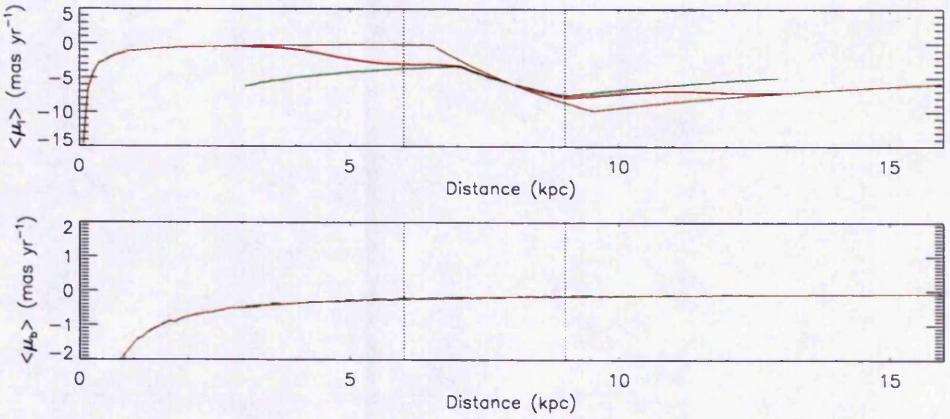

Figure 4.10: (Top, bottom) panel: expected average proper motions ($\langle\mu_l\rangle$, $\langle\mu_b\rangle$) as a function of distance towards BW, for bulge (green line), disc (brown line) and all (red line) stars. The vertical dotted lines indicate the apparent region of comparison to the observed trends (see text).

none has a large effect on the trend of $\langle \mu_b \rangle$, and only solid body disc rotation has a large effect on the trend of $\langle \mu_l \rangle$, as seen by the breaks in the disc stars' curve. The steep changes in $\langle \mu_l \rangle$ and $\langle \mu_b \rangle$ at small distances are due to the Sun's peculiar motion.

These predictions appear to agree quite well with the observations. K06 stated that they do not see very faint stars that are more likely to be on the far side of the bulge, and their magnitude cuts were designed to select only bulge stars. Hence the observed trends should only be compared with the predictions in the bulge region. K06's $\langle \mu_l \rangle$ trend is very similar to that predicted in Fig. 4.10 for all stars in the region 6–9 kpc, close to the Galactic centre. For $\langle \mu_b \rangle$, K06 did not appear to find any systematic trend with distance. This would be consistent with the approximately flat predicted trend in the bulge region.

Fig. 4.11 shows the predicted dispersions as functions of distance. The basic trend is for the dispersions to decrease with distance, as expected from projection effects. These trends are more strongly influenced by the modifications to the model than were $\langle \mu_l \rangle$ and $\langle \mu_b \rangle$. Four sets of panels are therefore shown, to illustrate the effects of each model adjustment.

Fig. 4.11(a) is generated with the initial model, including $\sigma_{x,y,z}$ recalculated from the TVT (as expected, the recalculation has little effect on this trend). The dispersions of the separate populations of bulge and disc stars generally fall smoothly with distance. However, the solid body rotation of the inner bulge causes a small peak in the overall $\langle \sigma_l \rangle$. Here, the rotation speeds of the bulge stars are smaller than in the region of flat rotation, increasing the average difference between the longitudinal velocities of bulge and disc stars, and hence increasing the overall $\langle \sigma_l \rangle$. This peak is disrupted by a spike in the disc stars' $\langle \sigma_l \rangle$, which is due to the discontinuity in the model disc rotation at the Galactic centre (a sudden switch from large positive σ_l to large negative σ_l).

Fig. 4.11(b) includes the effect of variable σ_z in the bulge. The trend of $\langle \sigma_b \rangle$ is now very different for the bulge stars: the rise in σ_z towards the centre is reflected in a similar rise in $\langle \sigma_b \rangle$.

Fig. 4.11(c) includes the effect of solid body rotation in the inner disc. This removes the discontinuity in the disc stars' longitudinal motions at the Galactic centre, and hence removes the spike in $\langle \sigma_l \rangle$. It also reduces the rotation speeds of the inner disc stars, bringing them closer to the speeds of the bulge stars, and hence removing the peak in $\langle \sigma_l \rangle$.

Fig. 4.11(d) includes the effect of a gradient in the bulge rotation. This has a slight smoothing effect on the trend of $\langle \sigma_l \rangle$ for all stars.

These dispersion trends towards BW do not appear to match those observed. While K06 found flat trends with $M*$, the model has both σ_l and σ_b falling with increasing distance. However, there may in fact be agreement. As discussed above, the plots from K06 given in Fig. 4.9 only cover a relatively small distance range, possibly 6–9 kpc. In this region, the predicted dispersions fall by < 0.5 mas yr^{-1}, which would be consistent with the observed flat trends, within the uncertainties in the data.

The effects of the magnitude cuts discussed in §4.4.7 can now be explained. Remember that applying the cuts did not significantly change the trends of σ_l or σ_b with l or b, but the dispersions were slightly increased. The magnitude cuts mostly select stars in the bulge. Fig. 4.11 shows that this eliminates nearby stars with high dispersions, and also the more distant stars with the lowest dispersions. However, the LOS cone will of course contain many more of the distant stars than those nearby, so the magnitude cuts will remove more stars with small dispersions, causing the slight increase in the predicted σ_l and σ_b.

4.4.11 Proper motion distributions

Fig. 4.12 shows the probability distributions of μ_l and μ_b for the final model (they are not significantly changed by the model modifications described above).

Note that the disc stars cause two distinct peaks in μ_l. This is due to most of the disc undergoing flat rotation, hence most disc stars along the LOS move with either a large positive, or large negative, μ_l. Of course, a similar effect is expected for the bulge stars, as the bulge also has mostly flat rotation, but instead a single broad curve is seen in Fig. 4.12. We return to this matter shortly.

The shapes of these predicted trends generally agree with those seen by K06. They found the distributions of μ_l and μ_b separately for the bulge and disc stars, which they distinguished by their colours: red and blue, respectively. Their plots are given in Fig. 4.13. K06 only saw those disc stars on the near side of the Galactic centre, hence their blue curve corresponds to the predicted disc star peak around $\mu_l = 0$. Both the predictions and observations find that disc stars on the near side of the bulge are shifted towards positive μ_l relative to the bulge stars. This is expected, as these disc stars are of course closer to us, and have greater rotational speeds (and nearby stars also have larger proper motions due

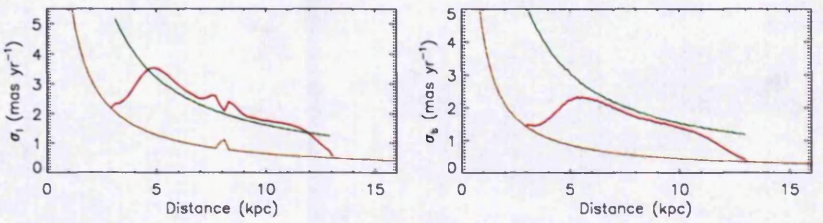

(a) Initial model with $\sigma_{x,y,z}$ recalculated from the TVT.

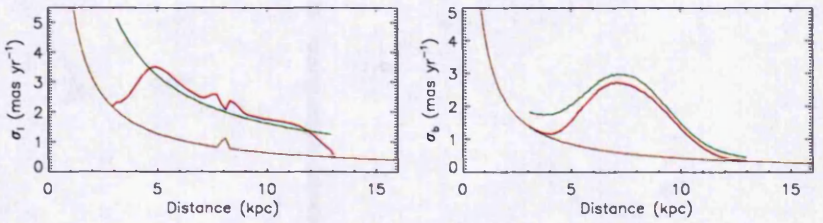

(b) As above, with variable σ_z in the bulge.

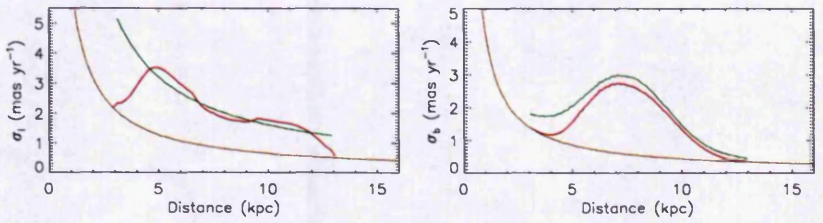

(c) As above, with solid body rotation in the inner disc.

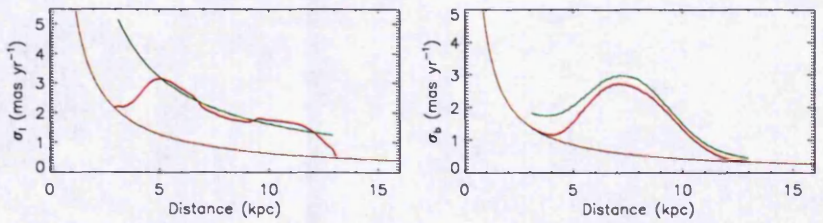

(d) As above, with a gradient in the bulge rotation.

Figure 4.11: (Left, right) panels: expected (σ_l, σ_b) as a function of distance towards BW, for bulge (green line), disc (brown line) and all (red line) stars, and for different model adjustments as indicated.

to projection). K06 also saw a slightly wider μ_b distribution for red stars than for blue stars. The model similarly predicts a wider curve (although much wider than observed) for bulge stars than those in the disc, due to the bulge stars' larger σ_z.

As mentioned above, there should be a shift in μ_l between bulge stars on the near and far sides of the Galactic centre. Sumi, Eyer & Woźniak (2003) measured proper motions of stars in the OGLE-II database, and found that red clump giants (RCGs) on the far side of the bulge had an average proper motion of $\sim$1.5$\pm$0.11 mas yr^{-1} toward negative l relative to near-side RCGs. The predicted μ_l and μ_b distributions shown in Fig. 4.12 are replotted in Fig. 4.14, for bulge and disc stars, with those on the near and far sides shown separately. We do indeed see the expected shift for bulge stars. The vertical dotted lines in Fig. 4.14 indicate this shift is $\sim$3 mas yr^{-1}, which is quite close to that given by Sumi, Eyer & Woźniak (2003). Note that observational studies divide stars into near and far side groups based on their magnitudes, with faint stars *more likely* to lie on the far side. Hence both groups may be contaminated by non-negligible numbers of stars wrongly assigned to them. In contrast, the model stars' exact distances are known. Hence it is to be expected that the predicted shift in bulge stars' proper motions would be slightly larger than any measured shift, since the predicted value is unaffected by such contamination.

The reason this shift in σ_l is smaller for bulge stars than for those in the disc is simple: the flat rotation speed of the bulge is much lower than in the disc – 100 kms^{-1} and 220 kms^{-1}, respectively (as given in §4.2.2). Hence the difference in longitudinal velocities across the LOS between near and far side stars is larger in the disc than in the bulge, as shown by Fig. 4.12. In addition, this larger difference in disc stars' μ_l clearly explains why – as briefly mentioned in §4.4.1, and illustrated by Fig. 4.1 – the overall expected σ_l, in any field observed by K06, is increased when disc stars are included in the calculation. It was also noted that, in contrast, σ_b is *decreased* when disc stars are included. Fig. 4.12 again provides the explanation: for μ_b, there is a much wider velocity spread for *bulge* stars. Therefore, including disc stars reduces the width of the μ_b probability distribution (compare the green and red curves in the right panel), and hence σ_b is lower. These expected differences in the bulge and disc dispersions may be easily tested observationally, by selecting a population of stars that preferentially lie in the bulge, such as RCGs.

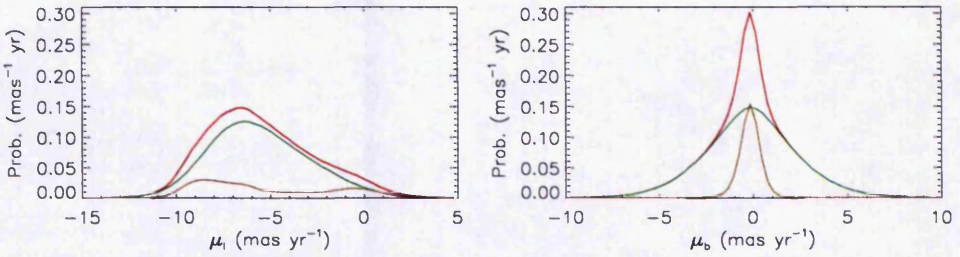

Figure 4.12: (Left, right) panel: expected probability distribution of (μ_l, μ_b), for bulge (green line), disc (brown line) and all (red line) stars. The distributions are normalised such that the curve for all stars has an area of unity.

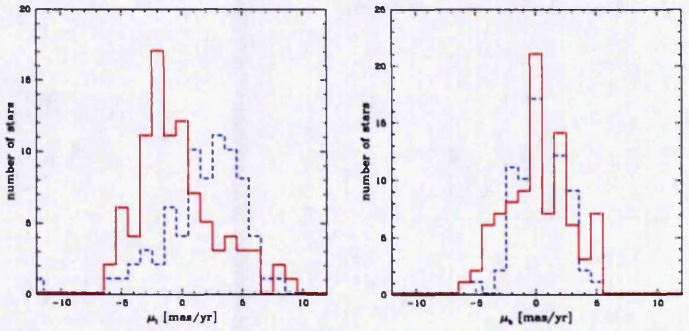

Figure 4.13: (Left, right) panel: proper motions (μ_l, μ_b) of red (solid line) and blue (dashed line) stars observed by K06 (fig. 6).

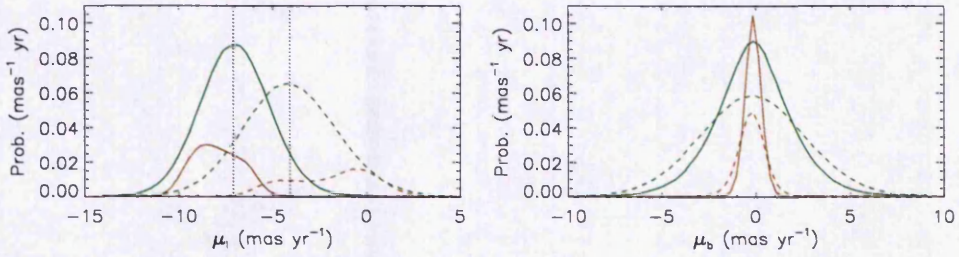

Figure 4.14: (Left, right) panel: expected probability distribution of (μ_l, μ_b), for bulge (green line) and disc (brown line) stars. Stars on the near and far sides of the Galactic centre are shown with the dashed and solid lines, respectively. The vertical dotted lines indicate that the shift in μ_l between bulge stars on the near and far sides is $\sim$3 mas yr^{-1}. The distributions are normalised as in Fig. 4.12.

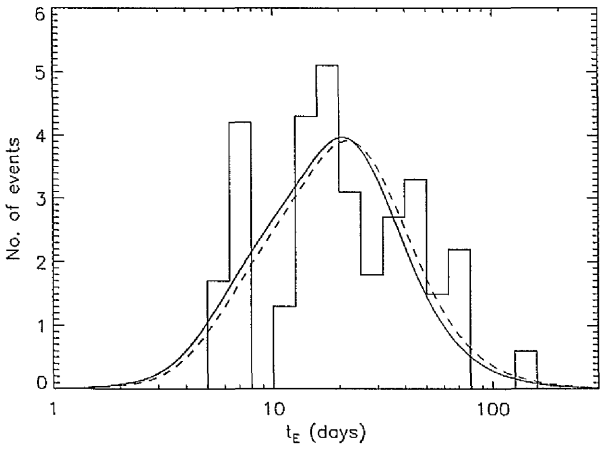

Figure 4.15: Microlensing event rate as a function of timescale. The (dashed, solid) line shows the (initial, final) model prediction along the OGLE LOS. The histogram shows OGLE's observed distribution. The model distributions are normalised to have the same areas as that observed.

4.4.12 Event timescale distributions

As shown in chapter 2, the simple initial model matched observed microlensing event timescale distributions with notable success. A few modifications to that model have now enabled a much better match to observed trends in proper motion dispersions. It is important to determine the effect of these model developments on predictions of event timescales.

In Fig. 2.14, the event rate as a function of timescale, $t_{\rm E}$, predicted by the initial model was compared with the distributions seen by OGLE (Sumi et al. 2006) and EROS (Hamadache et al. 2006). This prediction was made for the OGLE coordinates $(l, b) = (1.16°, -2.75°)$. It is given again in Fig. 4.15 (dashed line), along with that observed by OGLE, and the corresponding prediction of the final model (solid line). We see that there is little difference between the two predictions. (This is not due to any partial cancellation of larger competing effects from the individual modifications). The initial and final models give average timescales of 26.6 and 24.4 days, respectively, both in good agreement with OGLE's average of 28.1 ± 4.3 days, though the latter prediction is $> 1\sigma$ below EROS's 28.3 ± 2.8 days. The predicted median and quartiles are (19.7, 11.5, 32.3) and (18.3, 10.6, 29.7) days, respectively.

There are slightly greater differences further away from the Galactic centre.

Fig. 2.9 gave a map of predicted average timescale across the bulge, for the initial model. It is given again in the top panel of Fig. 4.16, with the final model map in the bottom panel. (These two maps are shown separately, rather than being overplotted, for clarity). In general, $\langle t_{\rm E} \rangle$ in any particular direction is reduced by a few days with the final model. This difference is of the same order as the current uncertainties in measured values of $\langle t_{\rm E} \rangle$, and so the work in chapter 2 need not be revised.

4.5 Summary and conclusions

This chapter has considered stellar proper motions and dispersions towards the Galactic bulge. Recent observations by K06 have been compared with predictions from a simple Galactic kinematic model that has successfully predicted microlensing event timescale distributions. This model has been modified to become increasingly realistic: by recalculating the bulge velocity dispersions from the TVT; by varying σ_z as a function of R; by including solid body rotation in the inner Galactic disc; and by adding a gradient in the bulge rotation. Streaming motions parallel to the bulge major axis, and stellar magnitude cuts have also been investigated.

Each stage of development has been analysed to show its effects on the dynamical predictions. The final kinematic model has shown good agreement with longitudinal and latitudinal trends of the dispersions and the anistropy ratio seen by K06. Predicted trends of average proper motion and dispersion with distance towards BW, and the expected proper motion probability distributions, also appear to be consistent with observations by K06 and Sumi, Eyer & Woźniak (2003). The only area of significant disagreement is the covariance. As expected, the model covariance is negligible, whereas K06 clearly detected a correlation between longitudinal and latitudinal motions, implying a significant tilt of the bulge velocity ellipsoid. Such a tilt is beyond the scope of the simple kinematic model presented here.

The modifications to the model cause a small change in the expected microlensing event timescales. Along the OGLE LOS, the average $t_{\rm E}$ is reduced by $\sim$2 days, and generally by a few days for lines of sight across the bulge. However, this is within the uncertainties of measured average timescales.

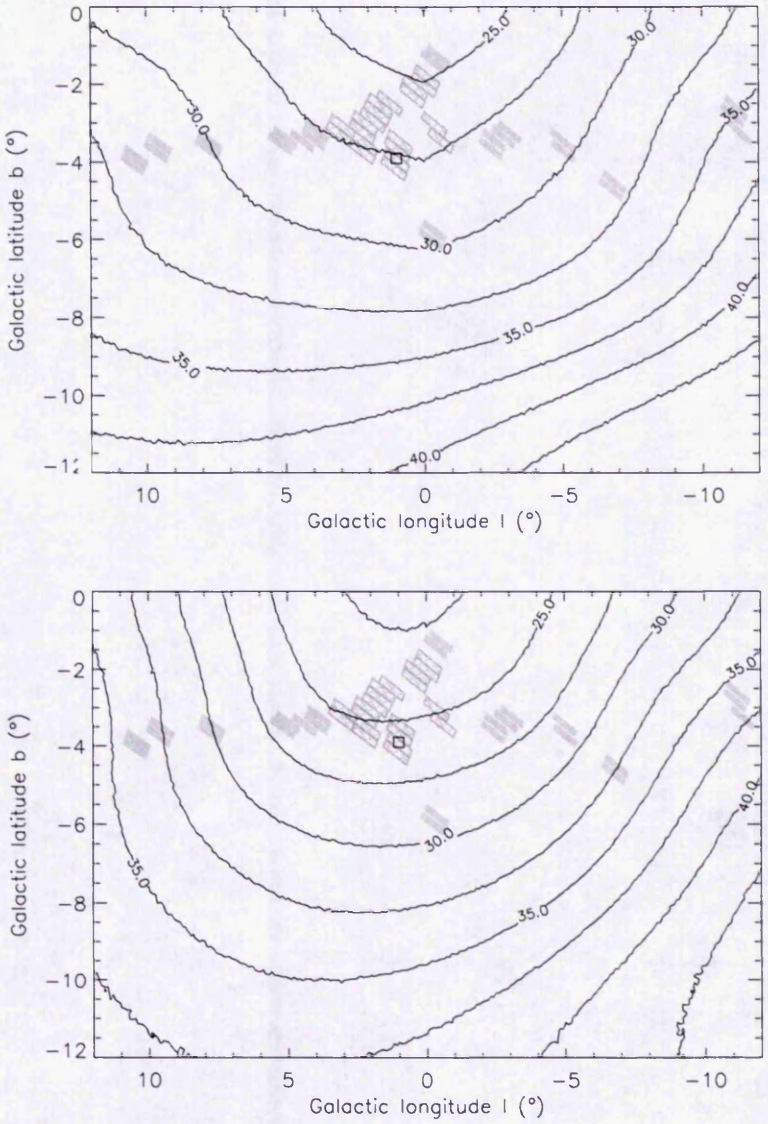

Figure 4.16: Map of the expected average event timescale, for the initial (top panel, same as Fig. 2.9) and final (bottom panel) models. The OGLE fields are shown by the grey boxes – the crosshatch pattern denotes the subset listed in Table 2.2, which were included in OGLE's reported $t_{\rm E}$ distribution. The small square indicates BW. Contour levels are at 22.5, 25, 27.5, 30, 32.5, 35, 37.5, 40 and 42.5 days.

References

Alcock C. et al., 1993, Nat, 365, 621

Binney J., 2005, in Turon C., O'Flaherty K.S., Perryman M.A.C., eds, ESA SP-576, The Three-Dimensional Universe with Gaia, p. 89

Binney J., Tremaine S., 1987, Galactic Dynamics, Princeton University Press, New Jersey

Bissantz N., Debattista V.P., Gerhard O., 2004, ApJ, 601, L155

Blum R.D., 1995, ApJ, 444, L89

Dwek E. et al., 1995, ApJ, 445, 716

Häfner R., Evans N.W., Dehnen W., Binney J., 2000, MNRAS, 314, 433

Hamadache C. et al., 2006, A&A, 454, 185

Han C., Gould A., 1995, ApJ, 447, 53

Han C., Gould A., 2003, ApJ, 592, 172

Kuijken K., Rich R.M., 2002, AJ, 124, 2054

Kozłowski S., Woźniak P.R., Mao S., Smith M.C., Sumi T., Vestrand W.T., Wyrzykowski Ł., 2006, MNRAS, 370, 435 (K06)

Kroupa P., Tout C.A., 1997, MNRAS, 287, 402

Mao S., Paczyński B., 2002, MNRAS, 337, 895

Merrifield M.R., 1992, AJ, 103, 1552

Sumi T., Eyer L., Woźniak P.R., 2003, MNRAS, 340, 1346

Sumi T. et al., 2004, MNRAS, 348, 1439

Sumi T. et al., 2006, ApJ, 636, 240

Udalski A., Szymański M., Kałużny J., Kubiak M., Mateo M., 1992, Acta Astron., 42, 253

Zheng Z., Flynn C., Gould A., Bahcall J.N., Salim S., 2001, ApJ, 555, 393

Chapter 5

Maximum likelihood analysis of the first directly detected microlens towards the bulge

This chapter presents an analysis of the first direct detection of a microlens towards the Galactic bulge. A maximum likelihood method is used to constrain the lens mass, and the distances to the lens and source. The relative influence of each observational constraint is also shown. Parts of the work in this chapter appear in Kozłowski et al. (2006b).

5.1 Introduction

As discussed in previous chapters, determining the optical depth can reveal much about the general shape and structure of the Galactic bulge and halo. However, it does not reveal the individual masses of lensing objects. The lens mass function can be probed by analysing the distribution of event timescales, but ideally it would be found directly from lens mass measurements.

As discussed in §1.4.3, this requires the lens mass degeneracy to be broken. A partial break comes from knowing the lens-source relative proper motion. To measure this, the lens must be individually resolved, which is potentially possible with current telescopes some years after an event, when the lens and source have moved sufficiently far apart. However, there are great practical difficulties. As shown in §2.4.6, even the *Hubble* and *James Webb* space telescopes (*HST* and *JWST*) will only resolve a lens and source for a few per cent of events $\sim$10 yrs after lensing. One of the main problems is that most lenses cannot be seen at all, being either dark objects or stars that are too faint. Thousands of events have been recorded, nearly all towards the bulge, but so far only one direct detection of a microlens has been published, towards the Large Magellanic Cloud (LMC).[1] This lens was detected 6.3 yrs after lensing, 134 mas away from the source, by the MACHO collaboration using the Wide Field Planetary Camera 2 (WFPC2) on the *HST* (Alcock et al. 2001). This detection of the lens, combined with parallax signatures exhibited during the event, enabled Gould, Bennett & Alves (2004) to produce the first precise mass measurement of an isolated star other than the Sun: $M = 0.097 \pm 0.016$ M$_\odot$. Since all other techniques exploit stellar companions, this remains the only such measurement to date, except for a crude estimation of the lens mass for an OGLE bulge event by Jiang et al. (2004): 0.36 M$_\odot$ $< M <$ 1.48 M$_\odot$.

This chapter presents the first direct detection of a microlens towards the bulge. At the time of writing, data analysis of the event is still being performed by the author's collaborators. When complete, five observational parameters will enable a precise estimation of the lens's mass and distance from a maximum likelihood calculation. At this stage three parameters have been securely determined, and preliminary likelihood calculations are presented here. The full analysis will appear in Kozłowski et al. (2006b). *Essential details of the collaborators' work*

[1] Another possible detection, also towards the LMC, has very recently been reported by Kallivayalil et al. (2006).

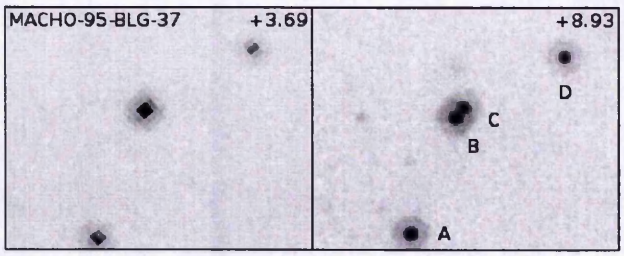

Figure 5.1: (Left, right) panel: (WFPC2, ACS) I-band image taken (3.69, 8.93) yrs after the peak of the event MACHO-95-BLG-37. The components A, B, C and D were all blended in the original MACHO seeing disc. The assumed source and lens pair are labelled B and C.

are given in §5.2, all other work in this chapter is by the author. The maximum likelihood method is presented in §5.3, and the results and discussion in §5.4. A summary and conclusions are given in §5.5.

5.2 Observations

As discussed in chapter 4, Kozłowski et al. (2006a) conducted a proper motion survey of stars in 35 bulge fields, each centred on a microlensing event seen by MACHO. They used *HST* images from two epochs 5–10 yrs apart. The first set were taken with the WFPC2, and the second with the High Resolution Channel of the Advanced Camera for Surveys (ACS). Images were obtained in I-band, with some additional first-epoch images in V-band. The *HST* observations are described in more detail in Kozłowski et al. (2006a).

The MACHO data are now analysed with difference image analysis to identify the lensed stars, and the *HST* images are then examined for any visible microlenses. Out of 34 events[2], 3 candidate lenses are found. In the most convincing case, for the event MACHO-95-BLG-37,[3] the lens and source are well resolved. Fig. 5.1 shows the two *HST* I-band images, taken 3.69 and 8.93 yrs after the peak of microlensing. The components B and C are assumed to be the lens and source. Which one is the lens, and which is the source, is currently unclear from the observations. This problem is addressed in §5.4.

[2]Of the 35 original events, one did not appear in the final MACHO catalog of Thomas et al. (2005).

[3]A full list of event parameters is given in table 3, Thomas et al. (2005), under MACHO ID 109.20635.2193.

Note that we have 3 lens detections from follow-up observations after ~10 yrs of a sample of 34 events – a detection rate of ~9%. This is the same order of magnitude as predicted in §2.4.6: 1–2 % of lenses should be detected after 10 yrs with the *HST* (using the ACS). If only the most convincing of the 3 detections is considered, the actual detection rate falls to ~3%, in good agreement with the predictions. (Of course, this agreement is based on small statistics).

The best-fit separation between the MACHO-95-BLG-37 lens and source is ~106 mas, giving a relative proper motion $\mu = 11.82 \pm 0.32$ mas yr^{-1}. The longitudinal and latitudinal components of this motion are $\mu_l = 11.64 \pm 0.75$ mas yr^{-1} and $\mu_b = 2.06 \pm 0.75$ mas yr^{-1}, respectively. The observed magnitudes of components B and C are $I_{\rm B} = 18.45 \pm 0.03$ and $I_{\rm C} = 19.07 \pm 0.04$, respectively.

With these parameters, the assumption that the components B and C really are the lens and source can be tested – it is possible that they are, instead, so closely aligned by chance. The source may have actually been another star that was only visible when lensed, and the lens may also have been another, faint, star or a dark object. Given the measured relative proper motion of B and C, their separation at the time of the lensing event is found to be in the range -10.42–0.93 mas (where the minus sign corresponds to the direction of motion). This is consistent with exact alignment. The number density of stars brighter than I = (18.45, 19.07) is (0.0848, 0.1763) arcsec^{-2}. Thus the average number of stars within a circle of radius $(10.42 + 0.93)/2 = 5.68$ mas, brighter than I = (18.45, 19.07), is $(8.6, 17.8) \times 10^{-6}$. So the Poisson probability of having one star of I = (18.45, 19.07) within 5.68 mas of a source is $(3.2, 6.5) \times 10^{-6}$. Therefore, the probability that these two stars are aligned by chance is tiny. Furthermore, the probability that they should be so aligned, in the same direction as an unrelated microlensing event and at the time of lensing, is negligible. Hence it is safe to assume that these two stars are the lens and source.

The first-epoch *HST* images of the MACHO-95-BLG-37 stars were taken in two bands, I and V. This additional V-band image provides valuable extra information. However, complications that need not be discussed here mean that the V-band magnitudes of B and C have yet to be securely determined. Their combined flux is known – $V_{\rm B+C} = 19.52$ – but the relative fluxes are currently uncertain. The ratio is ~1:1. Preliminary estimates do, though, allow the image components to be approximately placed on a colour-magnitude diagram. This is shown in Fig. 5.2. Star C is certainly on the main sequence. Star B may be

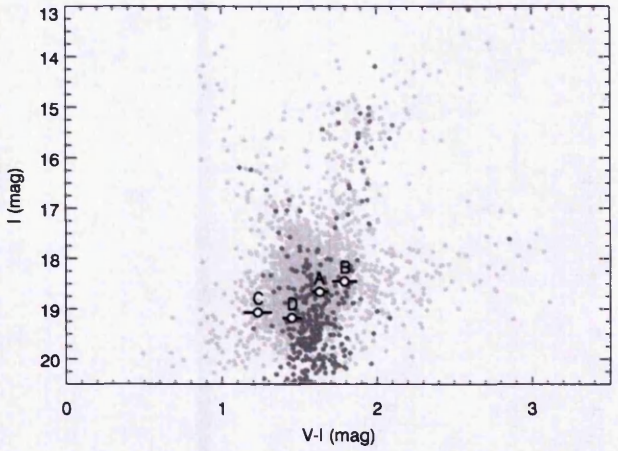

Figure 5.2: Colour-magnitude diagram of the MACHO-95-BLG-37 field, from observations by the *HST* (black dots) and OGLE-II (grey dots, Udalski et al. 2002). The open circles indicate the approximate positions of the components A–D.

either on the main sequence, or a red clump giant at a distance of ~40 kpc, a possibility that can be ignored.

Further complications, concerning unexpected anomalies in the original MACHO data, mean that the event timescale is also not precisely known. The value originally reported by Thomas et al. (2005), $t_{\rm E} \sim 19$ days, is thus incorrect. Preliminary estimates show that $40 \lesssim t_{\rm E} \lesssim 45$ days.

5.3 Maximum likelihood method

Most previous maximum likelihood analyses of microlensing events (e.g., Bennett et al. 2002; Bond et al. 2004; Smith et al. 2005) have used purely analytical likelihood functions. A more empirical approach is taken here. In chapter 2, a Monte Carlo model predicted microlensing optical depths and event timescales towards the bulge, in good agreement with measurements from MACHO, OGLE and EROS. This model is now used to generate events along the line of sight to MACHO-95-BLG-37. As the real lens is seen, dark lenses are not considered, leaving only main-sequence (MS) stellar lenses. These are assigned apparent magnitudes using the mass-M_I relation of Kroupa & Tout (1997), and the extinction $A_I = 0.74$ measured by Sumi (2004). MS lenses are assumed to have masses in the range 0.08–1.0 $M_\odot$, with more massive bodies having become dark stellar

remnants (see §2.2.2).

The differential event rate for each lens, from equation (2.8), is weighted by a likelihood L:

$$L \propto \exp\left[-0.5 \times \sum_{i=1}^{3}\left(\frac{p_{i,\ \mathrm{model}} - p_i}{\sigma_{p_i}}\right)^2\right], \tag{5.1}$$

where the model values of the event parameters $p_{1,2,3} = (\mu_l, \mu_b, I_{\mathrm{lens}})$ are compared to those observed. Model events are rejected if $(p_{\mathrm{i,\ model}} - p_{\mathrm{i}}) > 2\sigma_{p_{\mathrm{i}}}$ for any i, as they will contribute a negligible likelihood. The level of this cut, at 2σ, is somewhat arbitrary, but there is negligible difference when cutting at $> 2\sigma$.

As the lens may be either star B or C, both cases are considered. Hereafter they shall be referred to as the *bright lens* and *faint lens* case, respectively.

5.4 Results and discussion

Fig. 5.3 shows the likelihood as a function of distance, for both the lens and source, in both the bright and faint lens cases. The preferred lens distance D_{d}, and source distance D_{s}, are $5.25^{+0.12}_{-2.42}$ kpc and $8.95^{+0.70}_{-1.12}$ kpc, respectively, in the bright lens case. For the faint lens case, the values are $6.55^{+0.36}_{-3.18}$ kpc and $8.95^{+0.67}_{-0.95}$ kpc, respectively. (The 1σ uncertainties represent 68.3% of the areas under the curve on either side of the peak). There is a clear preference for the faint lens case, with its total likelihood a factor $\sim$2.2 greater than for the bright lens.

Fig. 5.4 shows the likelihood as a function of lens mass M_{d}. For the faint lens, the likelihood peaks at 0.96 $\mathrm{M}_{\odot}$, with a lower 1σ bound of 0.73 $\mathrm{M}_{\odot}$. For the bright lens, the likelihood continually rises up to 1 $\mathrm{M}_{\odot}$. This implies an MS lens too massive to be consistent with the model. However, we shall soon see that there is no cause for concern. Fig. 5.5 gives contours of likelihood as a function of M_{d} and D_{d}, showing a tight correlation between these two parameters. Note that none of these results (or those later in this chapter) are significantly changed, with respect to the uncertainites, if the kinematic model used here is replaced with the modified version developed in chapter 4.

Given that the primary observable for any microlensing event is the timescale, it is useful to see how much tighter the constraints on the lens distance and mass may become when t_{E} is precisely known. Fig. 5.6 shows contours of expected average t_{E} as a function of D_{d} and M_{d}. The dotted lines show that combining the preferred lens distances with a timescale in the range $40 \lesssim t_{\mathrm{E}} \lesssim 45$ days

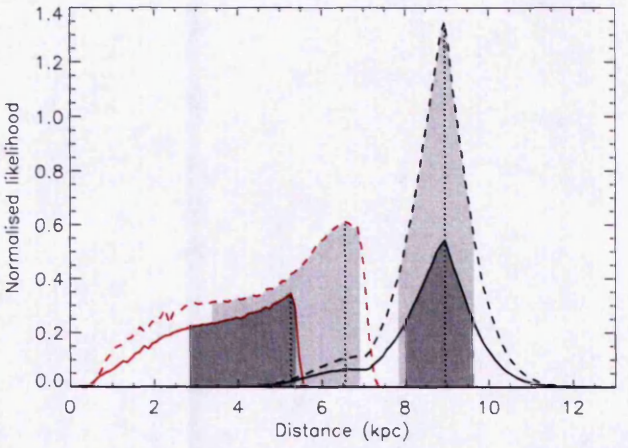

Figure 5.3: Likelihood as a function of distance, for the lenses (red lines) and sources (black lines), in both the bright lens (solid lines) and faint lens (dashed lines) cases. The vertical dotted lines show the preferred values, and the shading indicates the 1σ confidence intervals (see text). The curves are normalised such that the bright lens curve has an area of unity.

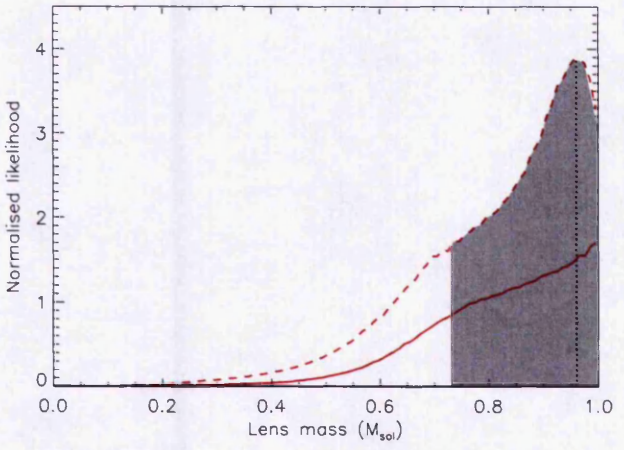

Figure 5.4: Likelihood as a function of lens mass, for the bright (solid line) and faint (dashed line) lens cases. The vertical dotted line shows the preferred $M_{\rm d}$, and the shading indicates the 1σ confidence interval (see text). The curves are normalised such that the bright lens curve has an area of unity.

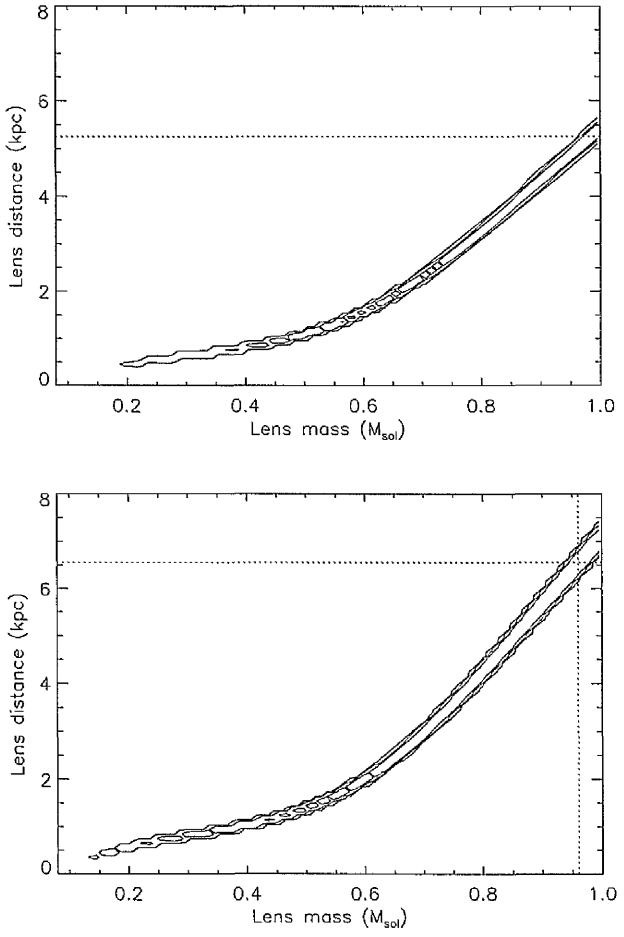

Figure 5.5: Contours of likelihood as a function of lens mass and distance, for the bright (top panel) and faint (bottom panel) lens cases. The dotted lines indicate the preferred $M_{\rm d}$ and $D_{\rm d}$. Contour levels are at (0.1, 1.0, 5.0); the normalisation is to a total area of unity.

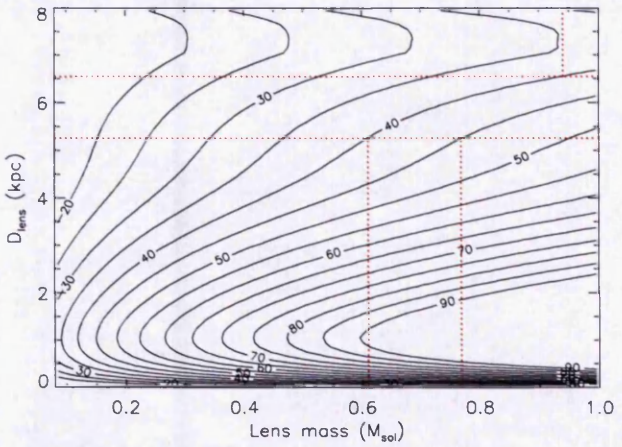

Figure 5.6: Contours of expected average event timescale as a function of lens mass and distance. The dotted lines indicate the preferred $D_{\rm d}$ and the suggested $M_{\rm d}$ for a timescale $40 \lesssim t_{\rm E} \lesssim 45$ days. Contour levels are at 20–90 days, in intervals of 5 days.

suggests a bright lens mass $0.61 \lesssim M_{\rm d} \lesssim 0.77$ M$_\odot$. However, we have seen that Fig. 5.4 shows a bright lens of $M_{\rm d} > 1$ M$_\odot$ is preferred. Fig. 5.6 suggests a faint lens of $M > 0.95$ M$_\odot$, whereas Fig. 5.4 shows a preferred value of 0.96 M$_\odot$ (a formal but unconvincing agreement). Clearly, the parameters used so far in the maximum likelihood calculation, μ_l, μ_b and I_0, are insufficient to achieve even a self-consistent solution of $D_{\rm d}$ and $M_{\rm d}$. This is not surprising. $t_{\rm E}$ must be included in the analysis at some level.

A precise measurement of V is also important: a MS star's colour varies significantly with mass, thus $M_{\rm d}$ could be much better constrained. We shall now see the considerable effect of including even crude estimates of $t_{\rm E}$ and V. The timescale is taken to be $t_{\rm E} = 43 \pm 3$ days. Since the combined flux of B and C is known, and their flux ratio appears to be ~1:1, the magnitude of each star is taken to be $V = 20.4 \pm 0.05$. Figs. 5.7 and 5.8 show the likelihood as functions of distance and $M_{\rm d}$, respectively. As expected, the lens distance and mass are now much more tightly constrained. The faint lens case is ruled out completely, with a total likelihood of zero. For the bright lens, the preferred distance is $D_{\rm d} = 1.90^{+0.14}_{-0.15}$ kpc. Note that the preferred source distance has not changed much: $D_{\rm s} = 8.90^{+0.77}_{-1.52}$ kpc (compared with the initial value of $8.95^{+0.70}_{-1.12}$ kpc). The preferred mass is $M_{\rm d} = 0.65^{+0.02}_{-0.02}$ M$_\odot$, well below the 1 M$_\odot$ limit. It therefore

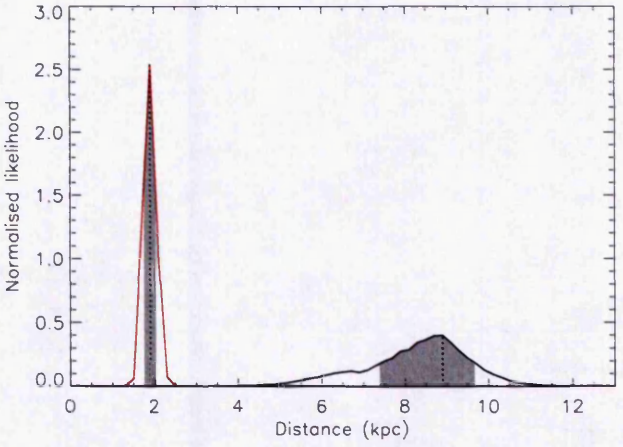

Figure 5.7: Likelihood as a function of distance, using all five observable parameters, for the bright lens (red line) and source (black line). The vertical dotted lines show the preferred values, and the shading indicates the 1σ confidence intervals. The curves are normalised such that the lens curve has an area of unity.

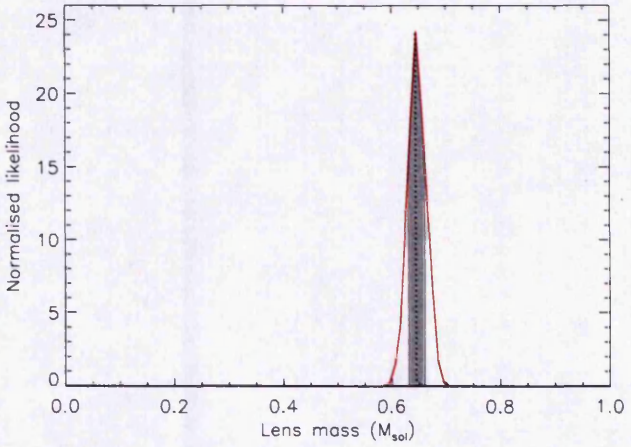

Figure 5.8: Likelihood as a function of lens mass, using all five observable parameters, for the bright lens. The vertical dotted line shows the preferred $M_{\rm d}$, and the shading indicates the 1σ confidence interval. The curve is normalised to an area of unity.

appears certain that the source star is a bulge star, while the lens is a MS star lying in the disc. Note the high precision of the mass estimate, comparable with the measurement of $M = 0.097 \pm 0.016$ M$_\odot$ by Gould, Bennett & Alves (2004). Likelihood contours as functions of D_d and M_d are given in Fig. 5.9.

A separate check on the self-consistency of this new solution is applied as follows. If μ, t_E, D_d and D_s are accurately known, then M_d can be determined directly:

$$M_\mathrm{d} = 1.168 \ \mathrm{M}_\odot \left(\frac{t_\mathrm{E}}{40 \ \mathrm{days}} \frac{\mu}{10 \ \mathrm{mas \ yr}^{-1}} \right)^2 \frac{D_\mathrm{s}}{8 \ \mathrm{kpc}} \frac{D_\mathrm{d}}{D_\mathrm{s} - D_\mathrm{d}}. \qquad (5.2)$$

Taking $t_\mathrm{E} = 43$ days, and the preferred values $D_\mathrm{d} = 1.90$ kpc and $D_\mathrm{s} = 8.90$ kpc, equation (5.2) yields $M_\mathrm{d} = 0.57$ M$_\odot$. This is well below the preferred mass ($M_\mathrm{d} = 0.65^{+0.02}_{-0.02}$ M$_\odot$). Thus it appears the solution is still inconsistent. However, the mass given by equation (5.2) is very sensitive to the lens distance: inputting $D_\mathrm{d} = 2.08$ kpc instead would yield $M_\mathrm{d} = 0.65$ M$_\odot$. This latter distance is less than 1.5σ above the preferred one ($D_\mathrm{d} = 1.90^{+0.14}_{-0.15}$ kpc). It is not surprising that a small discrepancy should occur in the results of the likelihood analysis, given that two of the observable parameters it used are not yet securely determined.

Five observable parameters are measureable: the event timescale, two lens colours and two components of relative proper motion. Inputting only three of these into the likelihood analysis dramatically failed to produce a self-consistent solution of the lens mass and distance, but including all five should do so with tight constraints on D_d and M_d. Already the faint lens case has been ruled out completely. Fig. 5.10 illustrates the relative influence on the analysis of the different observables. The lens likelihood curve in Fig. 5.7 is replotted, alongside the likelihood curves calculated from using each observable alone. It is clear that while no one parameter will allow any meaningful constraint at all on D_d, the lens magnitudes are most important for obtaining a precise estimate.

5.5 Summary and conclusions

This chapter has presented the first direct detection of a microlens towards the Galactic bulge, for which data analysis is ongoing at the time of writing. The latitudinal and longitudinal components of the lens-source relative proper motion are

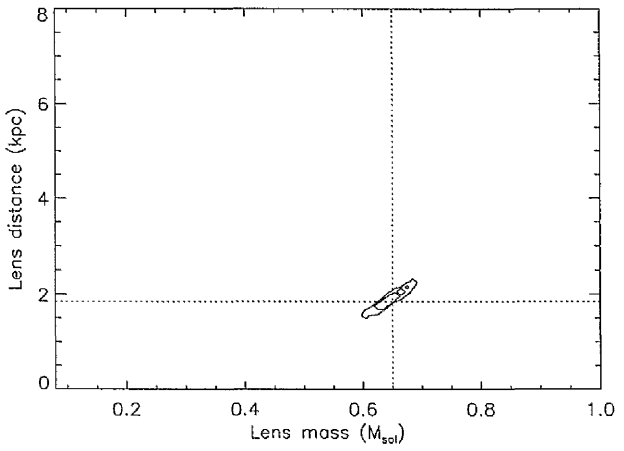

Figure 5.9: Contours of likelihood, using all five observable parameters, as a function of bright lens mass and distance. The dotted lines indicate the preferred $M_{\rm d}$ and $D_{\rm d}$. The tightness of the constraints is shown by the small size of the contour region (c.f. Fig. 5.5). Contour levels are at (0.1, 1.0, 5.0); the normalisation is to a total area of unity.

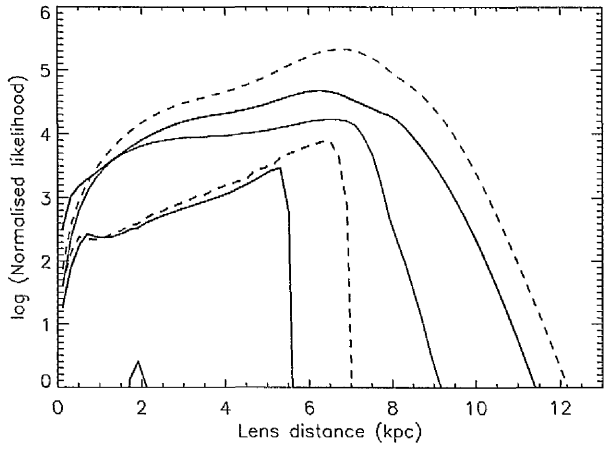

Figure 5.10: Likelihood (on a log scale) as a function of lens distance, using all observables (red line, same as in Fig. 5.7) and using each individual observable alone: $t_{\rm E}$ (black line), μ_l (green solid line), μ_b (green dashed line), I (blue solid line) and V (blue dashed line). The curves are normalised such that the curve using all observables has an area of unity.

precisely known, as is the lens's I-band magnitude. A preliminary maximum likelihood analysis has been performed. It has shown that when the event timescale and the lens's magnitude in V-band are also accurately known, the lens mass and distance will be tightly constrained. Knowledge of the lens's magnitude in both the I- and V-bands is particularly helpful. A full likelihood analysis with all the observed parameters will provide only the second precise mass measurement of an isolated star, other than the Sun, to date.

References

Alcock C. et al., 2001, Nat, 414, 617

Bennett D.P. et al., 2002, ApJ, 579, 639

Bond I.A. et al., 2004, ApJ, 606, L155

Gould A., Bennett D.P., Alves D.R., 2004, ApJ, 614, 404

Jiang G. et al., 2004, ApJ, 617, 1307

Kallivayalil N., Patten B.M., Marengo M., Alcock C., Werner M.W., Fazio G.G., 2006, ApJ Letters, submitted, preprint astro-ph/0609619

Kozłowski S., Woźniak P.R., Mao S., Smith M.C., Sumi T., Vestrand W.T., Wyrzykowski Ł., 2006a, MNRAS, 370, 435

Kozłowski S., Woźniak P.R., Mao S., Wood A., 2006b, ApJ, in prep.

Kroupa P., Tout C.A., 1997, MNRAS, 287, 402

Smith M.C., Belokurov V., Evans N.W., Mao S., An J.H., 2005, MNRAS, 361, 128

Sumi T., 2004, MNRAS, 349, 193

Thomas C.L. et al., 2005, ApJ, 631, 906

Udalski A. et al., 2002, Acta Astron., 52, 217

Chapter 6

Summary, conclusions and prospects

This chapter gives a summary of the results and conclusions presented in this thesis (§6.1 – §6.3), followed by a brief look at future prospects that relate to this work (§6.4).

6.1 Optical depth

As discussed in chapter 1, an accurate determination of the optical depth towards the Galactic bulge is of tremendous value in understanding the shape and structure of the Milky Way. It remains the key goal of observational and theoretical microlensing studies, and measurements are compared with expected values along as many lines of sight as possible. In chapter 2, a map of the optical depth was generated for a new Galactic model, based on the work of Han & Gould (2003), who used an empirical normalisation by *Hubble Space Telescope* (*HST*) star counts. Such maps can be compared with observations along any line of sight (LOS). The map, and optical depth profiles therein, were shown to be significantly different to predictions by Evans & Belokurov (2002) and Bissantz & Gerhard (2002), but in good agreement with the latest observations by OGLE (Sumi et al. 2006), MACHO (Popowski et al. 2005) and EROS (Hamadache et al. 2006).

One key question that has yet to be answered is why measurements of τ based on the lensing of red clump giants (RCGs) are much lower than, and inconsistent with, measurements based on lensing of all stars along the LOS. One possible reason – a dependance of τ on the different flux limits of the two methods – was investigated in chapter 3, and found not to provide an explanation. Expected optical depths were calculated for scenarios corresponding to the observations by OGLE and MACHO, using RCGs, and MOA (Sumi et al. 2003), using all stars. The model was seen to be consistent with the OGLE and MACHO measurements, but not that by MOA. The OGLE and MOA results were obtained using difference image analysis (DIA). DIA 'all-star' τ values are increased by the application of a (controversial) correction accounting for lensing of disc stars. Even allowing for this correction, the MOA optical depth was still significantly underpredicted.

Another intriguing result from chapter 3 was the prediction of τ as a function of source apparent magnitude. This trend was generally flat for magnitudes $I_0 \gtrsim 13$. However, there was a significant oscillation caused by RCG sources, due to their strong correlation between magnitude and distance – this correlation was clearly illustrated. A comparison with the latest observations from EROS was inconclusive. An oscillation was found to be consistent with the data, and provide a better fit than a flat trend, but with low significance, as the data are still insufficient.

The amplitude of this oscillation in the expected τ was shown to vary considerably as a function of $\theta_{\rm bar}$, the inclination angle of the bar to our LOS. Many models – including the one used here – and observations favour $\theta_{\rm bar} \lesssim 20°$. However, recent observations by Benjamin et al. (2005) and Hamadache et al. (2006) support much larger bar angles: $(44 \pm 10)°$ and $(49 \pm 8)°$, respectively. If the oscillation in τ was observed, and its amplitude accurately measured, additional constraints could be placed on the bar angle. The expected τ was also shown to vary significantly with $\theta_{\rm bar}$. The OGLE and MACHO optical depth measurements were combined with the predicted trends to place 1σ upper limits on $\theta_{\rm bar}$, which ruled out the larger bar angles.

6.2 Timescale, event rate distributions and kinematics

Whereas the optical depth depends on the total mass along a LOS, the timescale distribution depends on the composition of that mass (§1.3.1), thus offering a valuable probe of the lens mass function. A map of the expected average timescale was presented in chapter 2. The expected timescale distribution towards the bulge showed the same power-law tails as predicted by Mao & Paczyński (1996). When compared with the distribution seen by OGLE, there was found to be good agreement, but slightly poorer agreement with that seen by EROS. The most important discrepancy in both cases was an excess of long observed events. Following the recent discovery of a binary pulsar with an unexpectedly slow proper motion (Kramer et al. 2006), the potential for a population of such slow-moving massive lenses to produce an excess of long events was examined. However, any effect on the timescale distribution was found to be negligible.

The fractional contributions to the total expected event rate, as a function of timescale, were predicted for different types of lenses: brown dwarfs, main-sequence stars, white dwarfs, neutron stars and black holes. Asymptotic behaviour was clearly seen at both long and short timescales: the fractional contribution from a lens of mass M was found to be weighted by $M^2\, n(M)\, {\rm d}M$ and $M^{-1}\, n(M)\, {\rm d}M$, respectively. This is independent of the density and kinematics of the lens population, and hence provides valuable information concerning the lens mass function. In appendix A, these weightings were derived directly from the event rate equation (2.8). Similar asymptotic behaviour was seen as a function

of Einstein radius, and also explained mathematically.

The distribution of event timescales depends not only on the mass function, but also on the Galactic dynamics. The dynamics of the bulge are still not well understood. Though numerous attempts have been made to develop self-consistent models (e.g., Häfner et al. 2000; Bissantz, Debattista & Gerhard 2004), there has been limited good observational data, and few lines of sight, with which to compare the predictions. Predicting event timescale distributions offers a further test. However, microlensing surveys can help in another, more useful way. They involve prolonged monitoring of dozens of densely-populated stellar fields. Kozłowski et al. (2006a) obtained second-epoch observations of 35 bulge fields, centred on events seen by MACHO, with the *HST* after about 5–10 yrs. Hence they were able to measure high-precision stellar proper motions and dispersions, finding some clear trends with both Galactic latitude and longitude. In chapter 4, the simple kinematic model used elsewhere in this thesis was shown to provide a poor overall match to these trends. The model was gradually developed to become more realistic, and the effect of each modification was analysed. In only a few steps, a significantly better fit to the data was found. This demonstrates what can be achieved with models that are simpler and less computationally expensive than those constructed with other, more sophisticated techniques (e.g. Binney 2005). Reassuringly, none of the predictions made elsewhere in this thesis were significantly changed by using the new kinematic model.

6.3 Lens detection

Direct detections of lenses are rare, but of great importance. If a lens and source are resolved, an accurate measurement of the lens-source relative proper motion may be made. This would in turn enable the lens mass degeneracy to be partially broken, or even completely broken in certain cases (§1.4.3). In chapter 2, the proportion of stellar lenses that might be independently detected, under different selection criteria, was estimated. Currently, such detections are only possible several years after an event, when the lens has moved sufficiently far away (in projection) from the source for both to be resolved. Follow-up observations with the *HST* and *James Webb Space Telescope* were considered, and it was found that they should allow a few per cent of stellar lenses to be detected after 10–20 yrs.

The follow-up observations featured in the proper motion survey of Kozłowski et al. (2006a) have been searched for visible lenses[1] (chapter 5). Out of 34 events, three lenses were seen. This is a similar proportion to the estimate in chapter 2. The most convincing of these cases represents the first direct detection of a microlens towards the bulge, for which data analysis is ongoing. A prelimary maximum likelihood analysis was performed, which showed that when all the available observable parameters are securely determined, precise estimates of the lens mass and distance will be possible. This would be only the second precise mass measurement of an isolated star, other than the Sun, to date.

6.4 Future prospects

The numbers of microlensing events in the recent OGLE, MACHO, MOA and EROS analyses are still small, so the comparisons with the predictions in this thesis are not yet stringent. However, the complete databases of the microlensing collaborations collectively contain well over 2000 events. When these are included in a full analysis, tests of the Galactic models will become much more discriminating.

The future is bright for studies of microlensing. Planned and proposed space missions such as *Gaia* (e.g. Belokurov & Evans 2002), the *Space Interferometry Mission* (e.g. Gould 2003) and the *Microlensing Planet Finder* (e.g. Bennett et al. 2004), as well as the ground-based *Very Large Telescope Interferometer* (e.g. Delplancke, Górski & Richichi 2001), will enable observing programmes much more extensive than those currently underway. The full geometry of microlensing may be seen for hundreds of events, and similar numbers of direct lens mass measurements made, providing the first determination of the bulge mass function.

[1]This work, to appear in Kozłowski et al. (2006b), was conducted by the author's collaborators.

References

Belokurov V.A., Evans N.W., 2002, MNRAS, 331, 649

Benjamin R.A. et al., 2005, ApJ, 630, L149

Bennett D.P. et al., 2004, BAAS, 36, 1356

Binney J., 2005, in Turon C., O'Flaherty K.S., Perryman M.A.C., eds, ESA SP-576, The Three-Dimensional Universe with Gaia, p. 89

Bissantz N., Gerhard O., 2002, MNRAS, 330, 591

Bissantz N., Debattista V.P., Gerhard O., 2004, ApJ, 601, L155

Delplancke F., Górski K.M., Richichi A., 2001, A&A, 375, 701

Evans N.W., Belokurov V., 2002, ApJ, 567, L119

Gould A., 2003, in Ikeuchi S., Hearnshaw J., Hanawa T., eds, ASP Conf. Ser. 289, Proc. IAU 8th Asian-Pacific Regional Meeting, Volume I, p. 453

Hamadache C. et al., 2006, A&A, 454, 185

Häfner R., Evans N.W., Dehnen W., Binney J., 2000, MNRAS, 314, 433

Han C., Gould A., 2003, ApJ, 592, 172

Kozłowski S., Woźniak P.R., Mao S., Smith M.C., Sumi T., Vestrand W.T., Wyrzykowski Ł., 2006a, MNRAS, 370, 435

Kozłowski S., Mao S., Wood A., Woźniak P.R., 2006b, in prep.

Kramer M. et al., 2006, Sci, accepted, preprint astro-ph/0609417

Mao S., Paczyński B., 1996, ApJ, 473, 57

Popowski P. et al., 2005, ApJ, 631, 879

Sumi T. et al., 2003, ApJ, 591, 204

Sumi T. et al., 2006, ApJ, 636, 240

Appendix A

Event rate weightings in timescale tails

As described in §2.4.4, the microlensing event rate shows asymptotic behaviour at both long and short timescales. This appendix presents derivations that show the behaviour is directly related to the lens mass function; specifically, the fractional contributions are weighted by $M^2\, n(M)\, \mathrm{d}M$ and $M^{-1}\, n(M)\, \mathrm{d}M$, at very long and short timescales, respectively.

A.1 Introduction

The event rate is given by equation (2.8). However, as the mass dependence of the asympototic behaviour is the same for sources at different distances, we may ignore the source distance dependencies here. Therefore for a source at distance $D_{\rm s}$ and a population of lenses each with identical velocity v and mass M, the event rate is given by

$$\Gamma = \frac{4G^{1/2}}{c} \int_0^{D_{\rm s}} \rho(D_{\rm d})\, v \left[\frac{D_{\rm d}(D_{\rm s}-D_{\rm d})}{MD_{\rm s}}\right]^{1/2} {\rm d}D_{\rm d}, \qquad \text{(A.1)}$$

where $\rho(D_{\rm d})$ is the lens mass density at $D_{\rm d}$.

In reality, v and M both vary. The velocity probability distribution, $p(v)\,{\rm d}v$, can usually be approximated by a two-dimensional Maxwellian distribution

$$p(v)\,{\rm d}v = \frac{1}{\sigma^2} \exp(-v^2/2\sigma^2)\, v\,{\rm d}v, \qquad \text{(A.2)}$$

where σ is the velocity dispersion. For constant M, the factor $\rho(D_{\rm d})$ in equation (A.1) is simply the total mass density. When M varies, the event rate depends on the lens mass function, i.e. on how the total mass is partitioned into lenses of different masses. This is assumed to be same everywhere. The mass density for lenses in the range $M \rightarrow M + {\rm d}M$ can be written as a product of $f(D_{\rm d})\, Mn(M)\,{\rm d}M$, where $f(D_{\rm d})$ indicates the distance dependence and $n(M){\rm d}M$ is the number density of lenses in the range $M \rightarrow M + {\rm d}M$.

Integrating over the mass and velocity distributions, and using the fact that $\rho(M){\rm d}M = f(D_{\rm d})\, Mn(M)\,{\rm d}M$, gives

$$\Gamma = 2A^{1/2} \int_0^{D_{\rm s}} D_{\rm eff}^{1/2} f(D_{\rm d})\,{\rm d}D_{\rm d} \int n(M) M^{1/2}\,{\rm d}M \int v\, p(v)\,{\rm d}v, \qquad \text{(A.3)}$$

where $A = 4G/c^2$ and $D_{\rm eff} = D_{\rm d}(D_{\rm s} - D_{\rm d})/D_{\rm s}$. We can now rewrite the timescale equation (2.11) as

$$\begin{aligned} t_{\rm E} = \frac{r_{\rm E}}{v} &= \left[\frac{4GM}{c^2}\frac{D_{\rm d}(D_{\rm s}-D_{\rm d})}{D_{\rm s}}\right]^{1/2} v^{-1} \\ &= \frac{A^{1/2} M^{1/2} D_{\rm eff}^{1/2}}{v}. \end{aligned} \qquad \text{(A.4)}$$

The typical transverse velocity is $\sim\sigma$, and this defines a characteristic timescale

as

$$t_\sigma = \frac{A^{1/2} M^{1/2} {D_{\rm eff}}^{1/2}}{\sigma}. \tag{A.5}$$

The short and long tails satisfy $t_{\rm E} \ll t_\sigma$ and $t_{\rm E} \gg t_\sigma$, respectively.

A.2 Behaviour at long timescales

As can be seen from equation (A.4), the long timescale events occur when the lens and source both move approximately parallel to each other and almost parallel to the LOS. In this case, the transverse velocity is close to zero ($v \ll \sigma$) and the timescale becomes long.

For events with timescales longer than $t_{\rm long}$ ($\gg t_\sigma$), the transverse velocity must satisfy

$$v < \frac{A^{1/2} M^{1/2} {D_{\rm eff}}^{1/2}}{t_{\rm long}} \ll \sigma. \tag{A.6}$$

The exponential factor $\exp(-v^2/2\sigma^2)$ approaches unity, and so we have

$$\begin{aligned}
\Gamma(> t_{\rm long}) &= \frac{2A^{1/2}}{\sigma^2} \int_0^{D_{\rm s}} D_{\rm eff}^{1/2} f(D_{\rm d})\, {\rm d}D_{\rm d} \\
&\quad \times \int n(M) M^{1/2}\, {\rm d}M \int_0^{\frac{A^{1/2} M^{1/2} D_{\rm eff}^{1/2}}{t_{\rm long}}} v^2 {\rm d}v \\
&= \frac{2A^{1/2}}{\sigma^2} \int_0^{D_{\rm s}} D_{\rm eff}^{1/2} f(D_{\rm d})\, {\rm d}D_{\rm d} \\
&\quad \times \int n(M) M^{1/2}\, {\rm d}M \times \frac{1}{3} \left(\frac{A^{3/2} M^{3/2} D_{\rm eff}^{3/2}}{t_{\rm long}^3} \right) \\
&= \frac{2A^2}{3\sigma^2 t_{\rm long}^3} \int_0^{D_{\rm s}} D_{\rm eff}^2 f(D_{\rm d})\, {\rm d}D_{\rm d} \int n(M) M^2\, {\rm d}M.
\end{aligned} \tag{A.7}$$

Therefore, for long timescale events, the event rate follows a power-law as a function of the timescale, with a normalisation that depends on the mass function, $\propto M^2\, n(M)\, {\rm d}M$, as also derived by Agol et al. (2002).

A.3 Behaviour at short timescales

Re-expressing equation (A.4) in terms of $x = D_{\rm d}/D_{\rm s}$, we have

$$t_{\rm E} = \left[\frac{4GM}{c^2} x(1-x) D_{\rm s}\right]^{1/2} v^{-1}. \tag{A.8}$$

Very short events occur when the lens is very close to either the source or the observer, i.e. when $x \to 1$ or $x \to 0$. The asymptotic behaviour is the same for $x \ll 1$ and $1 - x \ll 1$, so we concentrate here on the case when $x \ll 1$, $x(1-x) \approx x$. For events shorter than a given timescale $t_{\rm short}$ ($\ll t_\sigma$), we must have

$$x < \frac{v^2 t_{\rm short}^2}{A\, M\, D_{\rm s}}. \tag{A.9}$$

Equation (A.3) can then be re-written in terms of x:

$$\begin{aligned} \Gamma(< t_{\rm short}) &= 2A^{1/2} \int_0^{D_{\rm s}} [x\,(1-x) D_{\rm s}]^{1/2}\, f(D_{\rm d})\, {\rm d}D_{\rm d} \\ &\quad \times \int n(M) M^{1/2}\, {\rm d}M \int v\, p(v)\, {\rm d}v. \end{aligned} \tag{A.10}$$

Changing the integration variable to x, and with $x \ll 1$, $f(xD_{\rm s}) \approx f(0)$, we obtain for the first integral

$$\begin{aligned} \Gamma(< t_{\rm short}) &= 2A^{1/2} \int_0^{\frac{v^2 t_{\rm short}^2}{A\, M\, D_{\rm s}}} x^{1/2}\, f(xD_{\rm s}) D_{\rm s}^{3/2}\, dx \\ &\quad \times \int n(M) M^{1/2}\, {\rm d}M \int v\, p(v)\, {\rm d}v \\ &= \frac{4}{3} \frac{t_{\rm short}^3}{A} f(0) \int n(M) M^{-1}\, {\rm d}M \int v^4\, p(v)\, {\rm d}v. \end{aligned} \tag{A.11}$$

Therefore for short timescale events, the event rate follows a power-law as a function of the timescale, with a normalisation that depends on the mass function, $\propto M^{-1}\, n(M)\, {\rm d}M$.